SIMULTANEOUS SENSING OF PRESSURE AND TEMPERATURE USING A SELF-TEMPERATURE-COMPENSATED FABRY–PÉROT MEMS MECHANISM

by

Sepideh Ghaderian

A thesis
presented to the University of Waterloo
in fulfillment of the
thesis requirement for the degree of
Doctor of Philosophy
in
Mechanical and Mechatronic Engineering

Waterloo, Ontario, Canada, 2022

Examining Committee Membership

The following served on the Examining Committee for this thesis. The decision of the Examining Committee is by majority vote.

External Examiner	Dr. Regina Lee Professor Dept. of Earth and Space Science and Engineering York University
Supervisor	Dr. Patricia Nieva Professor Dept. of Mechanical and Mechatronics Engineering University of Waterloo
Internal Member	Dr. Kevin Musselman Associate Professor Dept. of Mechanical and Mechatronics Engineering University of Waterloo
Internal-External Member	Dr. Eihab Abdel Rahman Professor Dept. of Systems Design Engineering University of Waterloo
Internal-External Member	Dr. Hamed Majedi Professor Dept. of Electrical and Computer Engineering University of Waterloo

Author's Declaration

This thesis consists of material all of which I authored or co-authored: see Statement of Contributions included in the thesis. This is a true copy of the thesis, including any required final revisions, as accepted by my examiners. I understand that my thesis may be made electronically available to the public.

Statement of Contributions

This thesis is based on a combination of papers pending submission. The chapters are adapted from the following list of work, with specific reference to the papers provided within the chapters:

1. S. Ghaderian, A. Ghannoum, P. Nieva, "Reviews on Extrinsic Fabry–Pérot Interferometric Pressure Sensors"
    - S. Ghaderian conducted a literature review and prepared the manuscript. A. Ghannoum and P. Nieva supervised and gave valuable feedback on the development of an in-depth review of pressure sensors.

- Contribution:
    - Presented a review of the various developed fiber-optic Fabry–Pérot Interferometric (FFPI) pressure sensors in two main configurations: diaphragm-based and diaphragm-free sensors.
    - Investigated fabrication techniques and diaphragm material selections in detail. Each fabrication technique was analyzed based on the advantages and disadvantages of the implemented method. Moreover, the pressure sensitivity of each FFPI sensor was summarized in tables in the paper.

2. S. Ghaderian, A. Ghannoum, P. Nieva, "An Extrinsic Fabry–Pérot Interferometric Temperature Sensor based on the Thermo-Optic Effect Using a Cost-Effective Signal Demodulation Method"

- S. Ghaderian designed an extrinsic FFPI temperature sensor, conducted experiments, and numerically modelled the device. A. Ghannoum developed the optical signal analyzer used in the experiments. P. Nieva supervised the whole project.

- Contribution:
  - Developed and evaluated an extrinsic FFPI temperature sensor based on the thermo-optic effect (TOE) of silicon in the temperature range of 0–100°C.
  - Implemented a cost-effective signal modulation method based on a photodiode.
  - Designed and fabricated protective stainless-steel packaging with a threaded locating component to connect an optical fiber through a connector.
  - Investigated the thermo-optic coefficient (TOC) of silicon theoretically and experimentally.
  - Studied the modulation depth of the device by using different couplers with different splitting ratios.

3. S. Ghaderian, A. Ghannoum, P. Nieva, "Packaged Temperature and Pressure-Sensing Extrinsic FPI MEMS device for Harsh Environments with Self-Temperature-Compensation"
   - S. Ghaderian designed an FFPI microelectromechanical system (MEMS) device, conducted experiments to measure temperature and pressure and numerically analyzed and modelled the device. A. Ghannoum helped in the preparation of the experimental setup and developed the optical signal analyzer used in the experiments. P. Nieva supervised the whole project.
   - Contribution:

- Presented a harsh environment dual-sensing device that couples an FFPI with a MEMS to measure temperature and pressure.
- Designed and fabricated a unique stainless-steel packaging approach to prevent pressure from affecting the temperature measurement.
- The overall design shields fragile optical fibers and eliminates the use of electrical components in the sensing region.
- Developed an empirical model to consider the effects of temperature on the membrane deflection of the device.
- Conducted experiments to evaluate the device at 120°C and at over 1,000 psi.
- Developed an empirical model on the effects of temperature with a numerical analysis and the modeling of the device.

4. S. Ghaderian, A. Ghannoum, P. Nieva, "Optical Demodulation of an Intensity-Based Fiber Optic Fabry–Pérot Pressure Sensor"

➢ S. Ghaderian developed the model and tested it by using a MATLAB code. A. Ghannoum and P. Nieva supervised and gave valuable feedback throughout the work.

➢ Contribution:

- Developed a model for the demodulation of intensity-based pressure sensors.
- Investigated a mathematical approach that can model a sinusoidal sensor signal in systems with gradual pressure change, which eliminates the dependency of operating in the linear range of the FFPI sensor.
- Demonstrated a method to determine the initial cavity lengths of developed FFPI pressure sensors.

Abstract

This thesis presents the design and development of a self-temperature-compensated sensor for measuring temperature and pressure in harsh environments using a combination of Fabry–Pérot interferometry and microelectromechanical systems (MEMS). A silicon-on-insulator (SOI) wafer is etched to form a dual mechanism consisting of a membrane and a solid block that is then coupled with two optical fibers contained in a unique and simple protective stainless-steel housing. The solid block uses the thermo-optical properties of silicon for temperature measurements, while the deflection of the membrane is used for pressure sensing. An empirically based model combines solid mechanics and optical theory and is in good agreement with experimental measurements. As part of this work, the thermo-optic coefficient (TOC) of the silicon was also investigated theoretically and experimentally. The results show a good agreement between the TOC extracted from the experimental data and such a coefficient in published literature. Furthermore, a novel optical model for the demodulation of the intensity-based pressure-sensing mechanism was developed. This model relates the whole sensor-response profile to the measured parameters and eliminates linear range limitations. By using this model, one can also obtain the initial cavity lengths of an FFPI sensor, which can be very challenging at the microscale. A series of experiments conducted to test the performance of this multi-functional sensor showed that it can easily withstand pressures up to 1,000 psi and temperatures of up to 120°C, where the range of the temperature measurements are restricted only by the fiber optic materials. The developed self-temperature-compensated multi-functional sensor therefore serves as a promising tool in the precise characterization of pressure and temperature in harsh and/or complex environments.

Acknowledgements

I would like to express my thanks to God for giving me the chance to live and supporting me throughout my life. I would also like to express my sincerest gratitude to my supervisor Prof. Patricia Nieva for her support, guidance, patience, and the opportunity to work in this exciting field of engineering.

I would like to thank the University of Waterloo for giving me the opportunity to pursue my passions and continue my education in a warm and healthy environment. I would like to deeply thank my committee members Dr. Hamed Majedi, Dr. Kevin Musselman and Dr. Eihab Abdel Rahman and my PhD external examiner Dr. Regina Lee. This experience would not have been the same without the support of the SIMS Lab team members. I would also like to thank Dr. Abdul Rahman Ghannoum, who spent many hours with me in the lab and for fruitful conversations, and Mr. Omar Awad, for his constant encouragement.

Lastly, my deepest thanks to my beloved parents and my family. I am forever grateful for their unwavering support and love, which have been sources of strength in all my endeavors.

Table of Contents

List of Figures

List of Tables

List of Abbreviations

EFPI	Extrinsic Fabry–Pérot interferometer
EM	Electromagnetic
EMI	Electromagnetic interference
FEM	Finite element model
FBG	Fiber Bragg grating
FIB	Focused ion beam
FFT	Fast Fourier transform
FP	Fabry–Pérot
FPI	Fabry–Pérot interferometer
FS	Femtosecond laser
HCF	Hollow-core fiber
HC-PBF	Hollow-core photonic band gap fiber
HF	Hydrofluoric acid
IFPI	Intrinsic Fabry–Pérot interferometer
LED	Light-emitting diode
LD	Laser diode
MEMS	Microelectromechanical system
MMF	Multi-mode fiber
OPL	Optical path length

OSA	Optical spectrum analyzer
OSI	Optical signal interrogator
PCF	Solid photonic band gap fiber
RFI	Radio frequency interference
RI	Refractive index
SiC	Silicon carbide
SOI	Silicon-on-insulator
SOIMUMP	Silicon-on-insulator multi-user MEMS processes
SM	Single mode
SMF	Single-mode fiber
TOE	Thermo-optic effect
TOC	Thermo-optic coefficient
SD	Standard deviation
MSE	Mean squared error
DRIE	Deep Reactive Ion Etching

List of Symbols

σ	Conductivity
E_x	Time-varying electric fields
B_y	Time-varying magnetic fields
k	Propagation constant
$\emptyset$	Phase
λ	Wavelength
ω	Angular frequency
E_0	Amplitude of the wave
$\emptyset_0$	Phase constant
$\emptyset$	Phase
L	Cavity length
θ	Angle at which refracted rays are propagating with respect to the norm
n	Refractive index
R_{FP}	Fabry–Pérot reflectance
T_{FP}	Fabry–Pérot transmittance
P_i	Optical power
P_r	Reflected optical power
P_t	Transmitted optical power
R	Reflectance

$R_{\parallel}$	Parallel reflectance
$R_{\perp}$	Perpendicular reflectance
r	Reflection
$r_{\parallel}$	Parallel reflection
$r_{\perp}$	Perpendicular reflection
I_R	Reflected intensity
I_o	Initial intensity
I	Fraction of intensity
n_i	Index of the refraction of an incident medium
n_t	Index of the refraction of a transmitted medium
M	Modulation depth
I_{max}	Maximum intensity
I_{min}	Minimum intensity
ν	Poisson's ratio
P	Distributed load given in a force/area
b	Membrane length
E	Elastic modulus
t	Thickness of a membrane
δ	Deflection
x	Number of data points
Y_i	Observed values

$\widehat{Y}_i$	Predicted values
$\bar{Y}$	The mean value of the data set

1 Introduction

Today, sensors are used daily in industry, fabrication, medicine and other fields; they are fundamental to measuring various parameters and detecting when things are about to go wrong [1]. The demand for rapid, affordable, low-cost and reliable devices for making parameter measurements, especially in harsh environments, is on a constant rise [2].

Sensors are usually designed to minimally affect what is measured, which is one of the intrinsic advantages of microscale-sized sensors. Furthermore, in most cases, a microsensor can reach a higher sensitivity and significantly faster measuring time compared with macroscopic approaches [3]. MEMS technology allows sensors to be fabricated on a microscale. MEMS sensors are gaining increasing interest for use in hostile environments in different industries (Fig. 1).

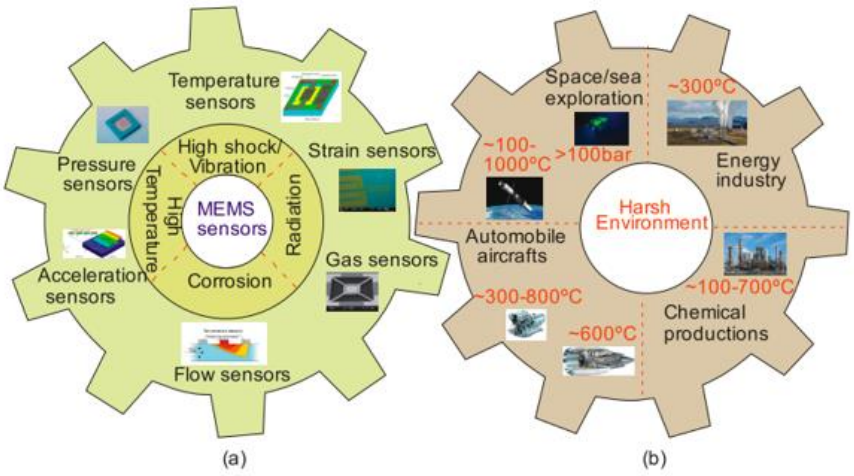

Fig. 1. (a) Different MEMS sensors and their harsh environments and (b) applications of MEMS sensors and their corresponding conditions (extracted from [4], an open access article distributed under the terms and conditions of the Creative Commons Attribution (CC BY) license).

However, hostile environments are not limited to only elevated temperatures and high pressures. Other harsh environments include ionizing radiation, radio frequency interference (RFI) and electromagnetic interference (EMI), which hinder the operation of sensors [5].

Fiber optic sensors are an attractive means for measurements under harsh environments [6]. The intrinsic advantages of fiber optic sensors include electromagnetic (EM) field immunity and resistance to radio frequencies as well as a small size and weight, high accuracy, high resolution, remote controllability, and distributed sensing capabilities. A combination of MEMS and fiber optics will thus pave the way for novel sensing concepts and applications. In this case, optical fibers are used as signal carriers, while MEMS chips work as sensitive elements to receive responses from environments [7].

One of the most effective methods used to combine versatile optical fibers with MEMS is the use of Fabry–Pérot interferometers (FPIs) [8]. FPIs consist of two reflective mirrors divided by a cavity that is a certain length; one of the reflective mirrors can be a MEMS device. FPIs are easily affected by perturbations that impact the two mirrors' optical path length (OPL). When perturbing factors, such as pressure, temperature and strain, are applied to a device, the OPL of the device changes and a measurand can be obtained through signal processing [9].

Among the different parameters of interest that are often measured, pressure and temperature are of significant importance. Measuring pressure is key in a wide variety of technologies and application areas, ranging from medicine (for blood measurements) [10] to space-shuttle operations [11]. Temperature detection also plays a major role in energy-saving practices and in monitoring production processes during which temperature may be influential [12].

FPI sensors have many intrinsic advantages, including a small size and an immunity to EM fields, that drive a need for FPI temperature sensors instead of conventional sensors, such as

thermistors and thermocouples. Thermometers often need to function in the presence of intense EM fields or to be employed at long distances. In such environments, sensors with metal leads are prone to eddy currents. This can cause noise and the possible heating of a sensor, which may lead to an inaccurate temperature measurement. Fiber optic temperature sensors do not use metal transducers to perform their conversions [13]. This allows for a minimal thermal dissipation through conduction and provides a quick response and extreme accuracy [14]. Considering the importance of temperature and pressure measurements, a reliable and long-term temperature- and pressure-monitoring device can bring substantial value to various industries, which justifies a great investment in this state-of-the-art measurement system [15]. This study thus incorporated fiber optic technologies to perform temperature and pressure measurements.

1.1 Thesis Objective and Approach

An FPI MEMS pressure sensor was designed in the Sensors and Integrated Microsystems Laboratory (SIMS Lab) of the University of Waterloo [16]. Experimental results proved the sensor's accuracy. However, the effects of temperature could not be clearly discerned, and thus, the experimental data that was collected needed further investigation. Therefore, the objective of this thesis was to analyze all the parameters that affect the FPI sensor's performance to ultimately create a novel and reliable FFPI self-temperature-compensated sensor capable of measuring both pressure and temperature.

The optomechanical design of FFPI self-temperature-compensated sensors is a highly integrated process involving many technical disciplines, including structural mechanics, thermomechanics, MEMS fabrication and signal processing. To achieve the final goal of developing a dual-mechanism sensing device, the process was divided into steps. First, by using a

MEMS chip, a temperature sensor was developed. Then, an integrated sensor was developed by using the same chip [13][15].

To achieve the goal of creating such a sensor, the following objectives were considered:

- Optimize the current SIMS Lab pressure sensor
    - Optimize the sensor and develop a second-generation prototype
    - Fabricate, test and validate numerical models
- Develop an FPI MEMS temperature-sensing mechanism
    - Design a housing to properly align an optical fiber with a MEMS device
    - Conduct experiments and tests and validate the results
- Develop an FPI MEMS mechanism for multi-sensing
    - Examine the impacts of all factors on the performance of the sensor
    - Design and fabricate packaging
    - Develop an FEM model and optimize the sensor
    - Fabricate a prototype and validate the experimental results
    - Develop an analytical model for a self-temperature-compensated FPI MEMS sensor
    - Model and demodulate to improve the signal processing

Fig. 2 summarizes the overall approach.

1.2 Thesis Outline

Chapter 1 summarizes the overall objectives and tasks. Chapter 2 covers background information and the FPI theory related to this study, centering on fiber optic FPI pressure and temperature sensing, followed by fiber optic configurations for parameter sensing and recent

developments in pressure and temperature measurement. The review focuses on pressure sensitivity and the creation techniques that have been reported. A few specific examples of technologies for FPI sensors that have been published are shared in detail to present their significant practical potential. Chapter 3 introduces the developed FPI temperature module based on the thermo-optic properties of silicon with a focus on three aspects: i) fabricate an epoxy-free housing, ii) align an optical fiber with an SOI chip and iii) investigate the TOEs of silicon. Chapter 4 focuses on the integrated FPI MEMS temperature and pressure sensing module. It discusses the numerical analysis of the sensor and compares the analysis with experimental results. All effective parameters, including the effects of temperature on the sensor's performance, were studied.

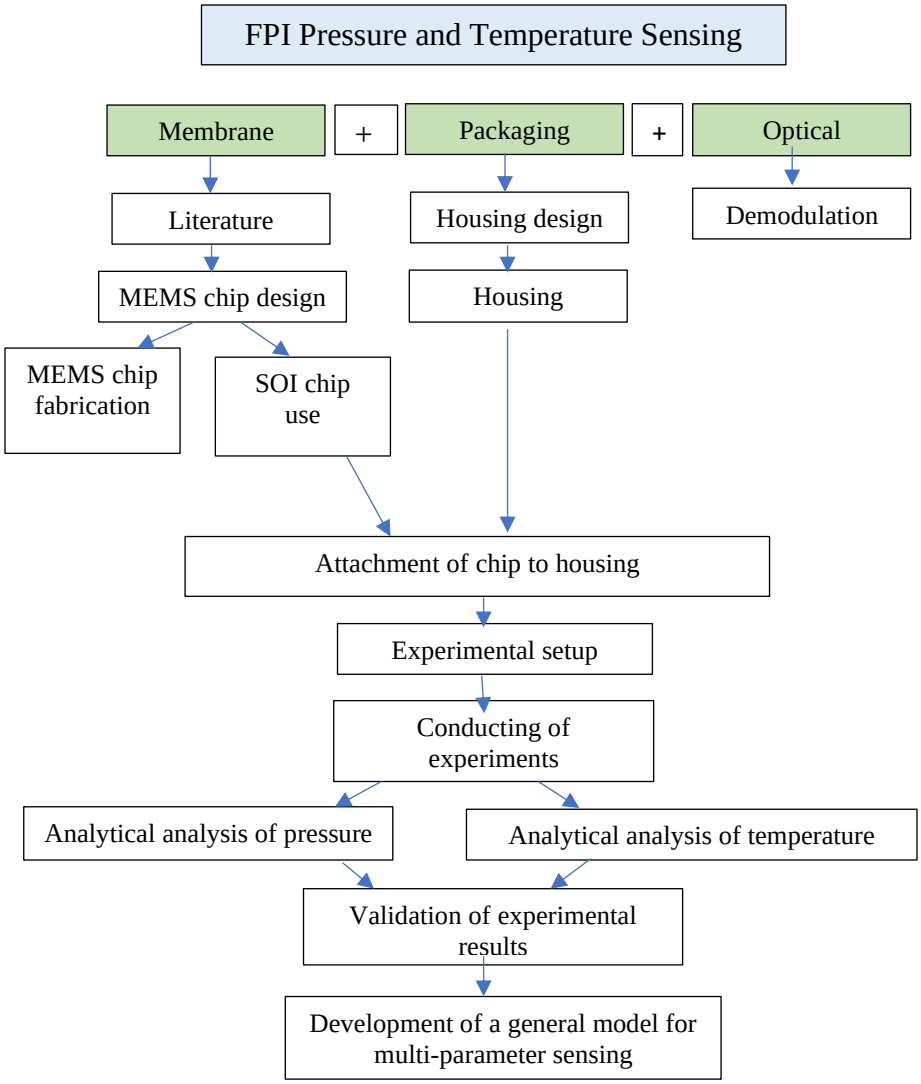

Fig. 2. A summary of the overall approach.

Chapter 4 also presents a theoretical analysis of the fiber optic sensor's output signal, for which finite-element modeling was required, and presents a coupling with a MATLAB model for the sensor. Predictions of the model are considered in comparison with the results of experiments. Chapter 5 discusses the impacts of applied pressure and temperature on the sensing device. The thesis ends with Chapter 6, which summarizes and concludes the thesis and makes suggestions for future research for the promotion of the FFPI MEMS pressure and temperature sensing system.

2 Background

The fundamental principle of fiber optic sensors is the measurement of external physical parameters. This is done by stimulating changes to one or more of the optical properties, e.g., the phase, intensity, wavelength and polarization, of a light beam traveling along an optical fiber [17]. A brief review the nature of light follows, after which an explanation of optical fibers is presented.

2.1 Wave Nature of Light

Light can be treated like a wave that is EM and has magnetic and electric fields that are time varying: B_y and E_x, respectively (Fig. 3). However, when a light wave interacts with matter that is non-conducting ($\sigma = 0$; conductivity), it is generally described with respect to E_x—the component relating to an electric field—instead of B_y. The reason for this is that the electric field displaces ions in the crystal or the electrons in molecules, causing the polarization of matter [18].

A sinusoidal wave that is the simplest traveling wave with respect to a propagation in the direction of *z* has the following general mathematical expression [19]:

$$E_x = E_0 \cos(\omega t - kz + \emptyset_0), \quad (1)$$

where E_x denotes the electric field that is at point *z* during time *t*, E_0 denotes the wave amplitude, *w* denotes the angular frequency, *k* denotes the constant of propagation determined using the

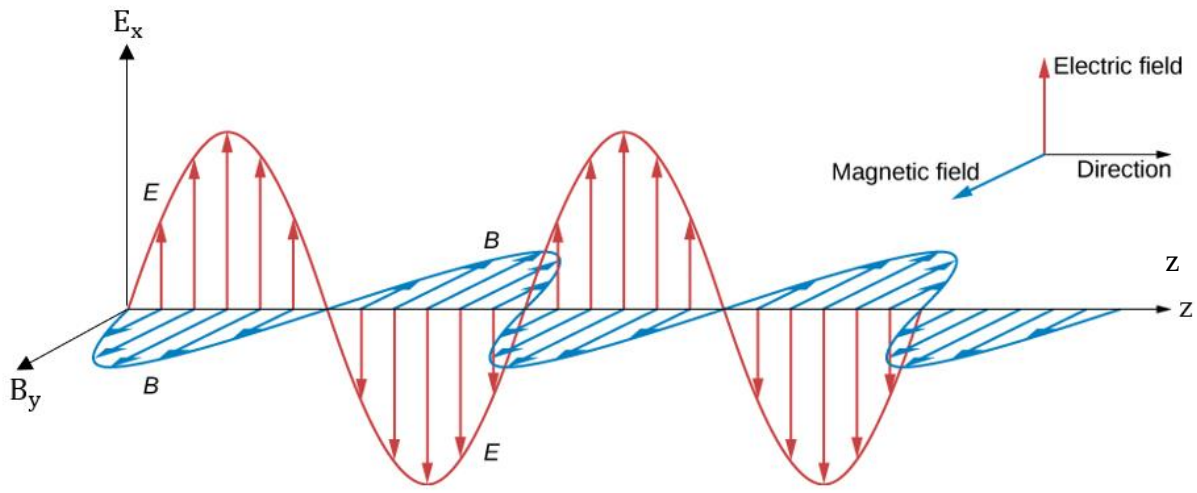

Fig. 3. A certain time of a specific sinusoidal EM or harmonic wave (redrawn from [20], page 24). E represents the electric field, B represents the magnetic field and z represents the direction of propagation.

expression $\frac{2\pi}{\lambda}$, λ denotes the wavelength and $\emptyset_0$ denotes a constant of the phase. The argument $(\omega t - kz + \emptyset_0)$ denotes the wave phase; it is represented by $\emptyset$ and describes the relationship between time and space [20]. Consider the following:

$$\emptyset = \omega t - kz + \emptyset_0 = \text{constant} \quad (2)$$

If a wave is following the direction of z with vector k as shown in (1), the difference of phase $\Delta\phi$ between two points divided using Δz is $k\Delta z$ because for each point, ωt is the same [21].

We now move on to review the equation that describes how an electric field is created. Field E obeys Maxwell's EM wave equation, and when a beam divergence is small, a Gaussian beam is the solution to Maxwell's equation [22]. Several different beams of light, e.g., a laser's output, can be described with the assumption that they are Gaussian. The diameter of a Gaussian beam $(2w)$

on any position of z is defined so the cross-section (πw^2) at the position comprises 86% of the power of the beam [23].

Gaussian beams are reviewed here because the intensity of light (that is, the radiation energy flow for each unit area and for each unit of time) distribution across the cross-section of the beam at any position along z is Gaussian [24]. During a propagation within a homogenous medium, a Gaussian beam remains Gaussian; only its parameters, e.g., its beam radius and wavefront curvature radius, change. The same is true for propagation through thin lenses or for reflections in weak mirrors. These properties give Gaussian beams a key role in optics [25]. The following part of this chapter describes the optic theories related to this thesis in greater detail.

2.2 Fiber Optic Sensing Fundamentals

In general, a fiber optic sensor comprises a source of light, optical fiber, sensitive element and detector (see Fig. 4) [17].

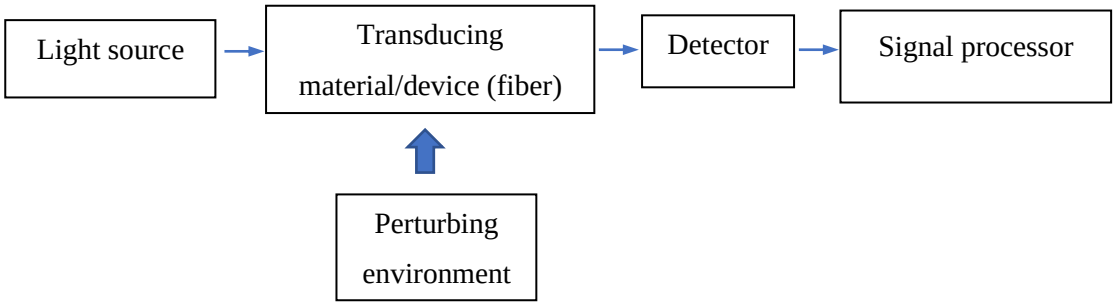

Fig. 4. The basic elements of a fiber optic sensor.

Fiber optic sensors can be categorized into four main groups: wavelength-modulated, polarization-based, intensity-modulated and phase-modulated sensors [26]. Due to a considerable sensitivity, fiber optic sensors that are phase-modulated are the best known and may be utilized in

a dynamic range that is significantly larger than that of other such sensors. Phase-modulated fiber optic sensors typically involve the use of optical interferometers to measure a change in the phase of a single light signal or, more often, a relative phase change between two light waves [27].

2.3 Interferometers

Interferometers generally use a broad, coherent monochromatic light source and two separate optical paths or arms. When a light wave is illuminated from a light source, the wave of light is separated into two coherent waves that are moving in two paths that are different. Then, the different waves are joined to interfere on a detector array (or a screen); the end result is called an interference fringe [28].

Four basic configurations that are interferometric exist: the Michelson, Mach–Zehnder, Fabry–Pérot and Sagnac configurations [29]. Among these, FPI has a greater sensitivity and does not have any fiber couplers, which may cause a sensor's deployment and data interpretations to be complicated [26]. This configuration is the one that was chosen for this work and is discussed in detail in the following section.

2.4 FPIs

FPIs are cavity-based interferometers that use the concept of phase modulation. The etalon (FP cavity) consists of two plates that partially transmit and reflect; they face each other and are divided by a spacer that is adjustable [30]. An optical etalon does not have to have two mirrors and free space between them. It can be a solid medium, the ends of which are used to reflect light [31].

For example, think of a beam of light that is an incident ray on an FP cavity that has a length of (L), as shown in Fig. 5. θ denotes the angle at which refracted rays within the cavity propagate in

relation to the norm. Moreover, k = $2\pi n/\lambda$ represents the constant of propagation within the cavity (λ is the wavelength of free space). The variable n is the refractive index for the medium within the cavity. A portion of the incident beam goes into the cavity. The light that goes into the cavity will undergo multiple reflections within the cavity in the case that the incident beam's wavelength relates to one of the cavity modes, which leads to a transmitted beam. The waves that are transmitted, e.g., A, B and C, become focused on point P on a screen through a lens [27]. This mechanism is illustrated in Fig. 5.

All points like this that have the same θ are positioned on a circle near the etalon axis. The interference pattern consists of dark and bright rings, and bright rings are for constructive interference while dark rings are for destructive interference [32]. This FPI ring is illustrated in Fig. 6. The difference between the phases A and B is 2kLcos θ; it is 2mπ, in which m denotes an integer for the purpose of constructive interference. Thus, P is bright (A, B, C, etc. are in a phase) if

$$2\text{kLcos}\,\theta = 2m\pi;\ m = 0, \pm 1, \ldots \tag{3}$$

For a normal incidence, these waves that are transmitted may interfere only constructively when $kL = m\pi$ [33].

The diameter of the interference ring is dependent upon the wavelength (λ) as well as on nL, the optical separation (refractive index × distance) for the etalon's plates. With just a tiny alteration of the optical path, nL (distance × refractive index) can result in a shift in the pattern of diffraction or displacement of the fringes that is measurable and may be utilized to infer on nL [34][35].

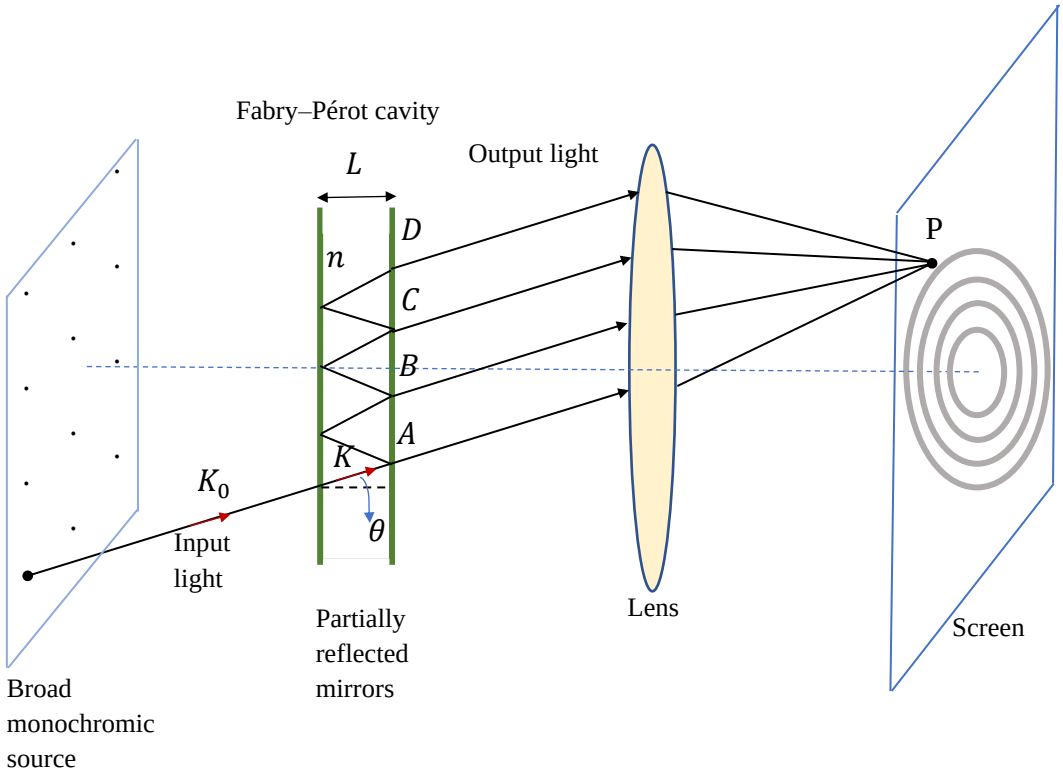

Fig. 5. A Fabry–Pérot interferometer (the figure was modified and redrawn from [20], page 89). A, B and C are transmitted waves. L is the FP cavity length, θ is the angle of propagation, k is the constant of propagation within the cavity and n is the refractive index of the medium.

Fig. 6. An FPI interference pattern. The dark rings are for destructive interference and the light ones are for constructive interference.

In an FPI, interference's intensity is determined and monitored as a result of alterations in an effective parameter (λ, n or L) [17].

Returning to the reflectance and transmission of the light beams of an FP cavity, consider R_1 and R_2, two mirrors' (M_1 and M_2) reflectances (Fig. 7).

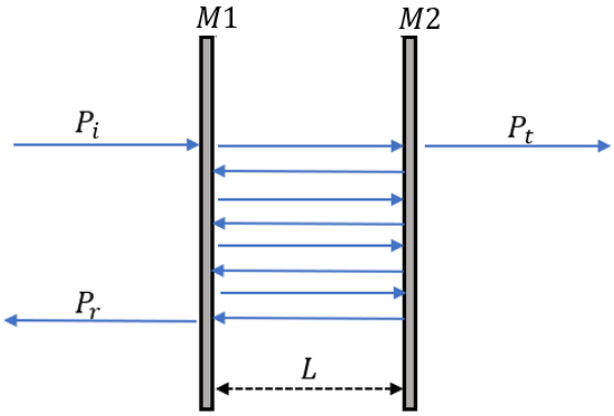

Fig. 7. A schematic of an ideal FP cavity that comprises two semi-transparent mirrors (M_1 and M_2) that are parallel and have equal reflectivities ($R's$). The figure is redrawn from [29]. L is the FP cavity, P_i is the incident, P_r is the reflected light and P_t is the transmitted optical power.

The Fabry–Pérot reflectance R_{FP} and the transmittance T_{FP} are presented in (4) and (5), respectively, for mirrors with different reflectances. It is assumed that the incident light is a monochromatic light with the wavelength λ and optical power P_i. In addition, P_r and P_t represent the reflected and transmitted optical power [9].

$$R_{FP} = \frac{P_r}{P_i} = \frac{R_1 + R_2 + 2\sqrt{R_1 R_2}\cos\emptyset}{1 + R_1 R_2 + 2\sqrt{R_1 R_2}\cos\emptyset} \tag{4}$$

$$T_{FP} = \frac{P_t}{P_i} = \frac{T_1 T_2}{1 + R_1 R_2 + 2\sqrt{R_1 R_2}\cos\emptyset} \tag{5}$$

A change in cavity length will cause a shift in the phase, and ultimately, the transmission will be varied [20]. (4) is a common equation in optical sensors that indicates the response of a Fabry-Pérot sensor is a periodic function of the device's FP cavity length [36].

Consider (4) and (5). R (reflectance) is used to determine the reflected light's intensity in relation to the incident light's intensity and is defined on its own for the components of an electric field that are perpendicular and parallel to an incidence plane [37] . It must be noted that in this thesis, only equations for normal incidence were considered because light that is emitted from numerous sources, e.g., light-emitting diodes (LEDs), is unpolarized. Consequently, it can be considered a collection or stream of EM waves, the fields of which are oriented randomly perpendicular to the light-propagation direction [29]. In a normal incidence, the reflectance for the components of an electric field that are perpendicular ($R_{\perp}$) and parallel ($R_{\parallel}$) to the incidence plane is equal [17].

Therefore, with a normal incidence, $R_{\perp}$ and $R_{\parallel}$ are determined using the following expression:

$$R = R_{\perp} = R_{\parallel} = (r)^2, \tag{6}$$

where the variable *r* is the term for reflection, which is greatly simplified for a normal incidence, as shown in (7) [21]:

$$r = r_{\parallel} = r_{\perp} = \frac{n_1 - n_2}{n_1 + n_2}, \tag{7}$$

where *n* represents the refractive index of the medium.

2.5 Single Fiber Optic FPI Interrogation

The interrogation of an FPI involves obtaining a readout signal based on a measurand [33] as in FPIs, a measurand causes a change in an optical phase. Thus, measuring optical phase variations is a crucial issue in FPI interrogations. A phase variation can be obtained from either the intensity

or the wavelength shift of an interferometric fringe [38]. Therefore, the interrogating techniques are categorized into intensity interrogating and spectral interrogating, respectively [27].

2.5.1 Intensity Interrogating Method

A schematic diagram of the intensity interrogating method for monitoring the OPL variations of an FP sensor can be seen in Fig. 8 [27]. Light that is generated from a laser diode (LD) or LED passes through a circulator (or a fiber coupler) and then propagates to the FP cavity. Next, beams experience numerous internal reflections within the FP cavity. The fiber recollects a resulting signal, where a phase difference occurs in the light that is reflected from the fiber, which is interfering with the light that was recollected from the FP cavity. After passing through the circulator again, the signal is redirected to a detector, which results in an intensity loss. Through a photodetector, the reflected light's intensity is converted; this is done by using a photodiode, and the light is converted into an electrical signal that is electronically processed. Finally, the electrical signal is transmitted for processing; light information is demodulated and utilized for a calculation of the measurand [39].

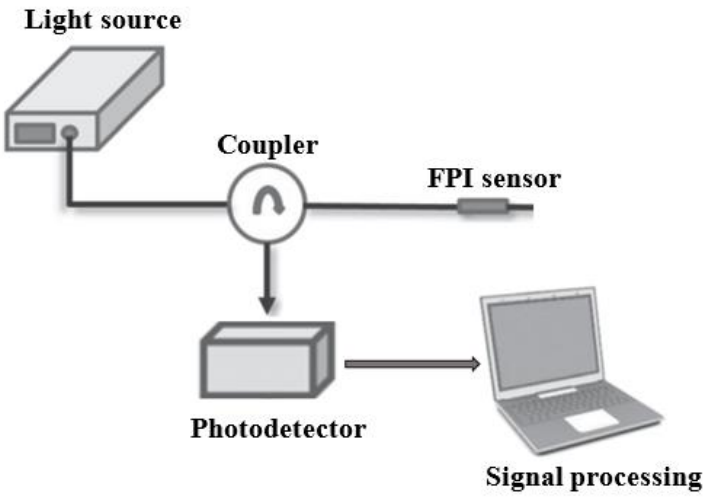

Fig. 8. A schematic diagram of the intensity interrogation method for monitoring the OPL variations of an FPI sensor.

2.5.2 Spectral Interrogating Method

The spectral interrogating scheme comprises a source of light, a coupler, and an optical fiber similar to the intensity interrogation method. The difference lies in the type of the detector. In spectral interrogation methods, a spectrometer is used instead of a photodetector [40]. When a measurand causes a change in the OPL, there is a shift in the light wavelength. By measuring the light spectra, the shift in wavelength can be obtained. Therefore, obtaining the spectrum of a signal light is critical. In order to get the full spectra of FFPI sensors, various methods, such as a broadband light source combined with a spectrometer [41]; a broadband light source combined with a tunable filter [42] and a swept or tunable laser combined with a photodetector [43], have been introduced. The spectra interrogation scheme results in a higher measurement accuracy. However, spectrometer-based technology is extremely expensive and is often used for special environment sensing with high-performance requirements [27].

2.6 Summary

This chapter summarized the most fundamental concepts in photonics, which are the nature of optical fields, including the wave nature of light, and Gaussian beam propagation. This chapter also reviewed basic principles in photonics related to fiber optics, including optical intensity, optical power, the interference of two nearly monochromatic waves, Fabry–Pérot optical cavities and interferometers. This provided a thorough understanding of the fundamental concepts related

to the continuation of this research work. These concepts are used when designing reliable harsh-environment Fabry–Pérot pressure and temperature sensors, the design of which was the goal of this thesis.

3 Literature Review

This chapter's basis is a paper by the author titled "Review on Fabry–Pérot Interferometric Extrinsic Pressure Sensors." It is an unpublished manuscript and is pending for submission in a journal.

3.1 Single Fiber Optic FPI Configurations

Fiber optic FPI sensors are typically categorized as intrinsic (IFPIs) or extrinsic (EFPIs) [37]. In both configurations, light is conveyed by a fiber through a two-stage process. The initial stage conveys it from an emitter to an interferometer, and the second stage conveys it from an interferometer to a detector. The difference lies in where the FP cavity is formed.

3.1.1 IFPI Configurations

In IFPIs, modulation takes place directly in an optical fiber where an FP cavity is formed. This FP cavity can be established between an internal mirror (a surface that is reflective) and either the fiber's polished surface or cleaved end surface (Fig. 9 (a)). Another way is to establish an FP cavity between two internal mirrors. Internal mirrors in IFPI configurations can be created through splicing together fibers that have end surfaces that are coated or through reflective splices of different kinds of optical fibers. Using these ways, the ends of an optical fiber should be non-reflecting, i.e., one should use an angled cut or broken fiber (Fig. 9 (b)).

The final way to form an FP cavity is to employ fiber Bragg grating (FBG; Fig. 9 (c)) [44]. Three mentioned configurations for IFPI sensors are shown in Fig. 9 , followed by brief discussions on the advantages and disadvantages of each.

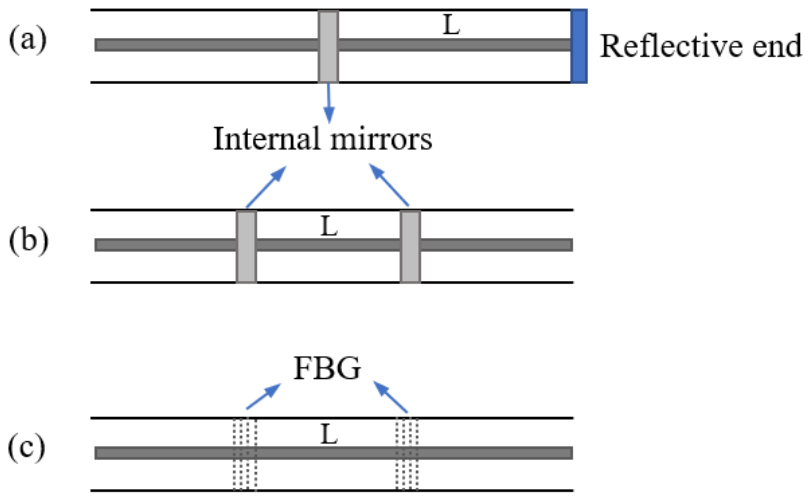

Fig. 9. The intrinsic FPI configurations. L represents the FP cavity length; The figure was redrawn from [9] for convenience: (a) an FP cavity established between an internal mirror and a reflective end surface, (b) an FP cavity created between two internal mirrors and (c) an FBG employed to create an FP cavity.

After discussing different configurations, we will now move on to discuss the advantages and disadvantages of each configuration. A thin film coating [45] has the advantages of mass production as optical fibers allow for a coating without any loss of spectral performance. However, a multi-layer coating with a small microscale thickness on the small cleaved surface of an optical fiber is not as stable as that of a substrate surface. Fusion splicing, which is a widely used method in FPI sensor fabrication, can be utilized to splice two coated fibers together [46][47]. Internal mirrors can be developed by fusion splicing two different fibers [48]. The most prominent advantage of fusion splicing is its low-cost fabrication [49]. However, such fibers spliced using the method lack repeatability, and the performance derived from final sensing strongly depends on the process of fusion splicing as the electric charge intensity and period need to be optimized

through a program in order to melt the surfaces of fibers for two-beam interference. Furthermore, the reflectance of mirrors distorts and significantly decreases as a result of fusion splicing [47].

The FBG IFPI sensor-fabrication process requires neither cleaving nor splicing over the sensor region [44]. The benefits of FBG IFPI sensors are a high mechanical strength, multiplexing and absolute measurements [50]. However, when using an optical spectrum analyzer, a shift in wavelength should be measured, which makes this technology complex and relatively expensive [51].

Finally, a cross-sensitivity to temperature is the main drawback of IFPIs that limits their application when temperature is an issue [27]. IFPIs are used mostly where multi-fiber sensors are needed that are arranged in a line. Mostly, a single-point sensor is enough for many uses. EFPI sensors, discussed in the next section, are more practical for single-point measurements [9].

3.1.2 EFPI Configurations

A sensing process is EFPI if an FP cavity is formed in any medium except an optical fiber, such as solid materials or an air gap. However, due to optical loss, the optical cavity is limited to a few hundred microns in EFPI configurations [22][23]. The typical structures of EPPI pressure sensors are categorized into two main configurations: diaphragm-based and diaphragm-free [54]. In the following sections, the typical structures of EFPI configurations are briefly explained.

3.1.2.1 Diaphragm-Free EFPI Pressure-Sensor Configurations and Recent Developments

In diaphragm-free EFPI pressure sensors, both a change in the FP cavity length and a variation in the refractive index (RI) of the cavity will lead to pressure sensing [55][56].

In EFPIs, diaphragm-free pressure sensors work according to FP cavity-length variations; when the pressure is acting radially on the structure, an internal fiber is driven to result in an alteration in the FP cavity length. Moreover, an optical-frequency-domain reflectometer is used to demodulate the pressure. Numerous developed EFPI pressure sensors make use of an air gap as the FP cavity. An air gap can be created through different methods, such as laser micromachining [57][58], etching with chemicals [59][60] and focused ion beam milling [61]. After an air gap is created, two fibers are spliced together (Fig. 10) through fusion splicing [47].

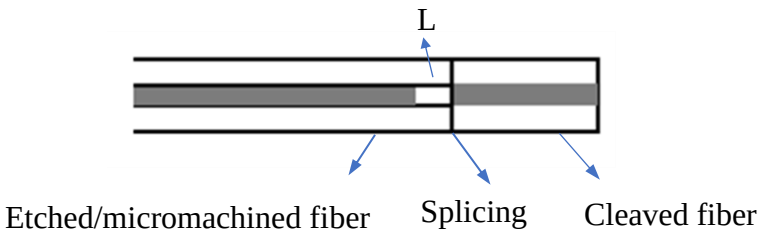

Fig. 10. The fabrication of a diaphragm-free EFPI pressure sensor by making use of fusion splicing. L denotes the FP cavity length.

Pevec et al. [62] used a micromachining process, including selective chemical etching, and a series of splicing and cleaving steps to fabricate a pressure sensor within the range of 0.003 psi. The developed pressure sensor was calibrated during the fabrication process by using controlled etching. The authors changed the pressure while the sensor was exposed to hydrofluoric acid (HF), and the sensor was connected to an optical signal interrogator. Reflected spectra were constantly monitored to read the cavity length to obtain the sensor's pressure sensitivity. Then, the sensor was disconnected from the HF, which was neutralized as the pressure sensitivity reached 27.57 nm/psi (the target pressure sensitivity).

Zhang et al. [63] used the chemical-etching and fusion-splicing method to fabricate a ball EFPI sensor capable of measuring pressure between 0 and 2 MPa. The end face of a standard single mode fiber (SMF) was etched for 15 min in a solution of 40% HF and then spliced to another cleaved fiber. Similarly, by using an MMF fiber that had been etched and filled with a UV adhesive, Chen et al. [64] proposed and fabricated an EFPI pressure device. The sensor has a pressure sensitivity of −0.28 nm/psi within the range of 0 to 145 psi.

The chemical-etching method has a low cost, and the process of creating cavities in a fiber tip is simple. The developed sensors have not only small measurement ranges normally in the kPa scale but also relatively poor mechanical strengths.

Another method used to form an air gap is to align two polished and cleaved ends of fibers in a hollow capillary or tube (Fig. 11 (left)) [65][66]. An air-gap cavity can also be formed in part of a hollow-core fiber (HCF) that has been spliced between two SMFs [67] (Fig. 11 (right)). The air-gap length (the FP cavity length) will lower in size as the hollow fiber's length decreases due to the pressure that is applied.

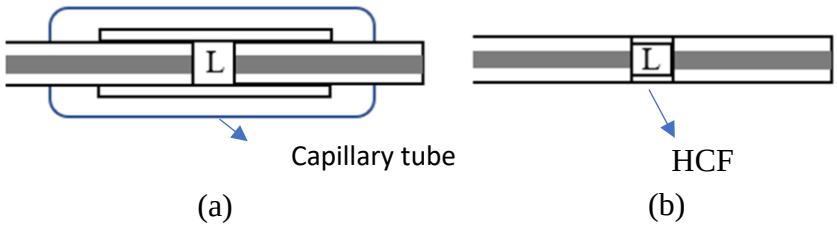

Fig. 11. Extrinsic FPI configurations with an air gap (L represents the FP cavity) [7][27]. The air gap is created (a) by aligning two polished and cleaved ends of fibers in a hollow capillary or tube and (b) by splicing an HCF between two SMFs.

As an example, Xu et al. used part of a silica rod (a hollow fiber) and spliced it between two SMFs to fabricate an EFPI pressure sensor [68]. A lead-in cleaved fiber was inserted into a hollow fiber, while another optical fiber that was cleaved was added from the hollow fiber's other side to create an FP cavity between the two ends of cleaved fibers. The authors calibrated the developed sensor with the help of electric arcs. While the fiber was joined to a white-light interferometer system, the gap of air was altered ahead of time; this was done by having a splicer stage grasp the fiber tail that was reflecting and by reviewing the tail online through the use of the white-light system. Once the gap of air was altered to achieve a value close to the aim, the electric arc was used to join the hollow fiber end and the reflection fiber. This was one of the first instances of an optical fiber's FP cavity length being controlled precisely by using electric arcs. This method is useful for the fabrication of sensors and for examining FP interferometers. However, it has two drawbacks: the system is costly and complicated.

Liang et al. [69] investigated an EFPI gas-pressure sensor that was diaphragm-free as the FP cavity was created through inserting an FBG that was well-cut and a silica tube that was hollow on both sides into a casing of silica. The length of the FP cavity between the SMF's ends and the hollow silica tube changed as the density of gas changed. Considering the principle that the density of gas changes based on changes in pressure, a measurement of pressure can be done in the range of room temperature to 800°C. The FPI gas-pressure sensitivity of the sensor is 0.029 nm/psi, and it has a high response to linear pressure of 14.5–101.5 psi. A method for temperature decoupling was used to enhance the sensor's accuracy in applications that involve high temperatures. The sensor does not experience a plastic deformation issue that ensures a way of measuring pressure at a high temperature. However, for sensing pressure, the temperature should be raised.

Fusion splicing and micromachining techniques can be utilized to develop hybrid EFPI pressure sensors by splicing different fibers together [21], such as all-solid photonic crystal fibers (PCFs) [70] and other kinds of microstructure fibers. PCFs can be fusion spliced between two SMFs and form an EFPI [71]. Ding et al. [72] fabricated an all-solid distributed pressure sensor; this was done by splicing an SMF and PCF. The PCF's free-end face had a film and a 99% reflectivity. Then, a digital resample was performed to obtain the PCF sensor head's optical spectrum with a 1 pm resolution. The sensor can experience the challenge of cross-sensitivity with two points of pressure, which is a limitation with respect to its practicability as a sensor of distributed pressure.

Yang et al. [56] fabricated a similar sensor; the authors spliced part of a silica capillary with a hollow core between a hollow-core PCF and an SMF. A configuration for an FP cavity was created as a result, with the sensing cavity working as a capillary tube and the PCF working as a passage of gas to an exterior environment. They then compared four different gas-pressure sensors based on fibers with configurations for FP cavities that used various kinds of PCFs with hollow cores. They found that exterior pressure changes can result in changes to the sensing-cavity air's refractive index. Consequently, a wavelength change occurs in interference dips. The authors measured the pressure sensitivity as about 0.027 nm/psi; the linearity was measured to be high at 99.7% or above, no matter the kind of PCF that was utilized as an inlet of gas.

Wu et al. [42] constructed a similar sensor within a range of 0–5,800 psi. The researchers performed this by splicing a standard SMF to a PCF of a short length. The PCF worked as an FP cavity and was a probe for direct sensing that did not require any more components. The FPI's spectrum of reflection was examined through using an optical spectrum analyzer.

By considering the dependence that applied pressure has on gas's refractive index, an EFPI with no diaphragm can also be utilized in hybrid sensors for the detection of gas pressure. Zhang

et al. [74][75] used three types of optical fibers, including SMF, HCF and coreless fiber (CF), to fabricate an EFPI pressure sensor. First, the SMF was spliced to the HCF, the latter of which was cleaved a length from the point of splicing. Then, the CF was spliced to the HCF and sequentially cleaved. A structure resembling a sandwich was used for the SMF-HCF-CF and formed the EFPI. Next, a microchannel was drilled into the side wall of the HCF with a femtosecond (fs) laser so gas could enter/exit the HCF. This created a pressure sensor without a diaphragm that had a 0–1,450 psi pressure range. However, using a high-quality fs laser requires one to establish high-resolution monitoring; this means that the device is very costly. Moreover, it is fragile as a result of partially removing some fiber material.

Xu et al. [45] published a paper on an EFPI gas-pressure sensor. The sensor was created through the fusion splicing of a small piece of a main capillary. The authors placed a feeding capillary at one endpoint and an SMF on the remaining endpoint. This was done so gas could enter the feeding capillary and from there enter the main capillary. The interferometer device's spectrum of reflection changed as the gas pressure changed; this was a result of the refractive index of the gas depending upon on the pressure that was used. The sensor has a pressure sensitivity of 0.028 nm/psi with a 0 to 220 psi range of pressure.

A similar EFPI gas-pressure sensor in the range of 174 psi was fabricated in 2017 [77]. An air cavity inside was created through fusion splicing together an SMF section to another SMF part that had an end-face microhole. Next, the authors crafted a microchannel; this was done to allow gas to flow in and vertically up the air cavity. Indeed, when a cavity of air cascades in a small length of SMF, an interference pattern involving three beams results. This varies along with the gas pressure within the inside cavity of air as a result of a refractive-index change in the gas. The

output fringe spectrum of the sensor is a three-beam interference pattern. The demodulation of a signal for a method like this is quite complex.

Ran et al. [78] created a probe for gas-pressure sensors that does not have a diaphragm and that has a 1,160 psi range. They performed this by using a quartz capillary and a hollow-core PCF. The quartz capillary works like a channel for a gas inlet that is microfluidic, while the HC PBF part works like an FP cavity. The sensor has a fast response, which is beneficial with respect to pressure measurements that are dynamic; however, further research and characterizations of the sensor are needed. Similarly, Tang et al. [79] demonstrated an EFPI device based on HC PBF that utilizes a channel that opens at the side and has a pressure sensitivity of 0.029 nm/psi. The authors developed an FPI by splicing together a thin HC PBF part between two standard SMFs. Next, they drilled a channel that opens at the side through the HC PBF's hollow core; this was done using an fs laser. They then examined cavity length's impact on its performance with respect to sensing gas pressure. They found that shorter cavities result in larger ranges of measurement and provide larger limits of detection (and vice versa).

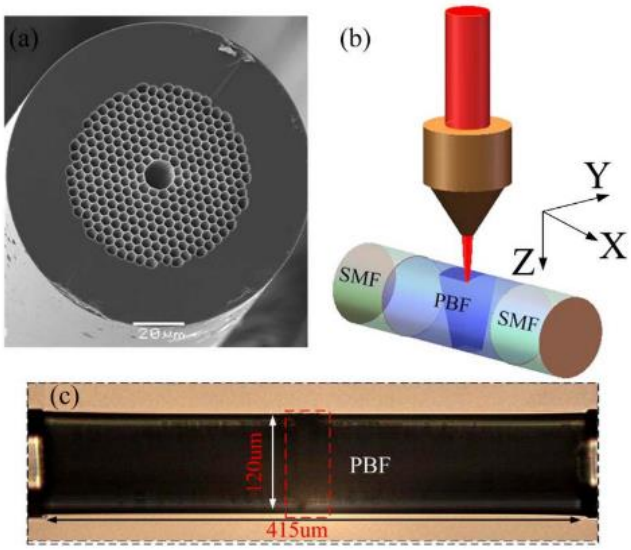

Fig. 12. The fabrication process of the diaphragm-free pressure sensor developed by [79]: (a) the HC PBF cross-section, (b) a schematic showing the creation with the fs laser and (c) an image of the side-opening FP cavity that the researcher drilled, presented from the side.

Although the FPI sensors used for measuring changes in cavity RIs each typically have a significant range of measurement and a good robustness, they often have a low pressure sensitivity. Moreover, a sensor head that is carefully designed can increase a system's complexity and manufacturing difficulty [33].

Table 1. A summary of diaphragm-free EFPI pressure sensors.

Authors	Year	Range (psi)	Sensitivity (nm/psi)	Fabrication Method	Demodulation Method
Yang et al. [56]	2021	3.23–20.6	0.02–0.03	Splicing a piece of a hollow-core silica capillary between a hollow core and an SMF	Wavelength shift in the interference
Pevec et al. [62]	2014	0–0.003	27.58	Micromachining	Spectral interrogation wavelength
Zhang et al. [63]	2019	0–290	−0.00026	Using the arc discharge-enlargement method and chemical etching	Shifts monitored by using an optical spectrum analyzer (OSA)
Chen et al. [64]	2017	2.9–133	−0.28	Etching MMF filled with a UV adhesive	FPI reflection spectrum noted upon using an OSA
Xu et al. [68]	2006	0–200	0.316–1.5	Fusion splicing	Spectrum fringe shifts
Zhang et al. [74][75]	2019	0–1,450	12.41	Fusion splicing	Wavelength shifts monitored by using an OSA
Liang et al. [69]	2018	14–101	0.029	Silica casing	Interference spectrum
Ding et al. [72]	2012	0–1,500	Not reported	Splicing a PCF fiber segment and an SMF	Optical spectrum
Wu et al. [42]	2011	0–5,800	3.8E-05	Splicing a PCF fiber segment and an SMF	Optical spectrum shifts
Xu et al [45]	2015	0–220	0.028	Fusion splicing	Reflection spectra
Xu et al. [77]	2017	0–174	0.027	Fusion splicing	OSA
Ran et al. [78]	2018	0–1160	2.87E-5	Using a quartz capillary and a PCF with a hollow core	Wavelength demodulation

Table 1 summarizes the above-discussed EFPI pressure sensors. These sensors had the common fused-splicing technique in their fabrication processes. A prominent advantage of fusion splicing is its low-cost fabrication. However, as aforementioned, fusion-spliced fibers (cleaved or coated) lack repeatability, and their sensing performance in the end depends significantly on the process of fusion splicing; the electric charge intensity and period need to be optimized through a program in order to melt the surface for two-beam interference. Furthermore, the reflectance of mirrors distorts and significantly decreases as a result of fusion splicing [60]. These kinds of EFPI structures suffer from a lack of mechanical strength and are applicable to only pressure measurements in kPa scale ranges [80][75].

3.1.2.2 Diaphragm-Based EFPI Pressure-Sensor Configurations and Recent Developments

In a diaphragm-based EFPI, for both a fiber-tip structure (Fig. 13 (left)) and a fiber-end structure (Fig. 13 (right)), a sensitive diaphragm is positioned close to the polished or cleaved end of an optical fiber. An FP cavity is created between the fiber's end and the diaphragm's reflecting surface [81][82]. The diaphragm has pressure placed on it, and a deformation occurs that corresponds to an alteration in the length of the FP cavity [83].

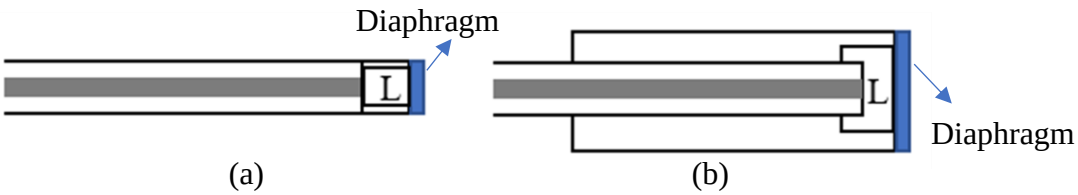

Fig. 13. An extrinsic diaphragm-based FPI configuration [7]: (a) a fiber-tip structure and (b) a fiber-end structure.

Wang et al. [84] established the design framework for pressor sensors with microdiaphragms by clarifying and defining the connections between sensitivity, side length, diaphragm thickness and resonant frequency. An investigation showed that a diaphragm that has a high resonant frequency and is sensitive has to be thin, and a small length of the side needs to be ensured. Rao et al. [27] recommended using a thick diaphragm for sensing high pressure and a thin diaphragm for sensing low pressure.

Many fiber-tip diaphragm-based EFPI pressure sensors are produced using fusion splicing [47] and chemical etching [85]. Chemical etching is based on the different etching rates of fiber cores and cladding due to their different material compositions [26]. Ge et al. [85] developed an EFPI fiber-tip pressure sensor for the range of 0–14.5 psi using the fusion splicing of an etched fiber with another cleaved fiber. A multi-mode fiber (MMF) was etched by using HF and spliced together with an SMF in order to create an FP cavity. Following this, the MMF was lapped to decrease its thickness and to allow it to work as a diaphragm. Wavelength demodulation was used to determine the length of the cavity, and this was performed to determine the loaded pressure. Another diaphragm-based hybrid sensor had a thin diaphragm made of silica that allowed the researcher to obtain the response of the sensor's pressure. It was fabricated using etching and polishing technology and can detect a pressure of 20.3 psi [86]. The resonator was formed by using an air cavity that was short and located at the fiber's tip. Similarly, Cibula [87] formed a pressure-sensitive diaphragm with a sensor sensitivity of about 0.068 nm/psi over a pressure range of 1,450 psi by etching one end of an optical fiber and further splicing a fiber that had been etched into a fiber that was cleaved.

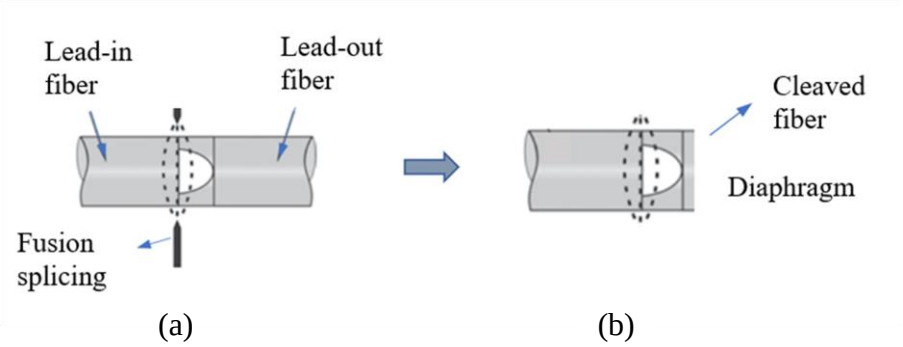

Fig. 14. A schematic of a diaphragm-based FPI formed by using fusion: (a) first, an etched fiber (lead-in fiber) is spliced with another fiber; (b) second, the end of fiber is cleaved. The figure was modified and redrawn from [87].

Zhu et al. [88] fabricated an all-fused EFPI pressure sensor that is made of silica; this was done directly on the tip of an optical fiber. The sensor includes three commercial silica fiber types, and the fibers were spliced together as follows. First, the researcher spliced an SMF with a 105 μm fiber and made a cleave beside it so there would be a thin 105 μm layer of fiber atop the SMF. Second, a fiber of 62.5 μm was spliced to that portion, and they cleaved it to a specific length to create an FP cavity. Third, the tip was placed in 50% HF; this was done in order to remove the 62.5 μm fiber's core. That fiber's cladding was undoped fused silica and remained almost intact.

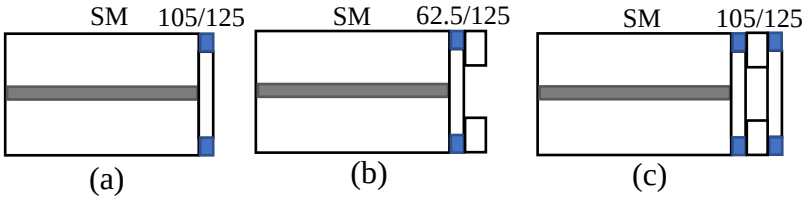

Fig. 15. A schematic of the fabrication steps for Zhu et al.'s diaphragm-based EFPI pressure sensor (the figure was modified and redrawn from [88]): (a) the etch barrier; (b) the splicing, cleaving and etching of the cavity and (c) the splicing, cleaving and etching of the diaphragm.

The cladding was left as the pit's wall. Fourth, the pit was spliced with a fiber of 105 μm to create an FP cavity. Finally, the 105 μm fiber was cleaved to serve as a diaphragm, which the researcher etched to reduce its thickness and allow it to work.

Chemical etching has the advantages of a low cost and suitability for mass production, but the rough inner surface of a cavity resulting from chemical etching considerably decreases the cavity surface's reflectivity. The roughness of the etched bottom of an air cavity usually renders it unstable for high-performance fiber optic EFPIs, and thus, it must be improved by optimizing the charge intensity and duration during the splicing process [85] [89].

The mechanical strength of two chemically etched fibers spliced together is better than that of an etched fiber spliced with a cleaved fiber because the diameters of the two etched fibers are equal [89]. However, a residual etching solution still affects the etched fiber [27]. Moreover, chemical etching decreases the fiber's melting point. Another drawback is that chemically etched fibers are cones, which is not ideal for EFPIs that are high quality [59].

Another type of EFPI pressure sensor that is of all-fused silica can be created directly atop the tip of a fiber. It uses a simple fabrication that requires only cleaving and fusion splicing. Wang [90] developed a pressure-sensitive diaphragm using an arc fusion splicer that was electric in order to align a hollow fiber between two cleaved standard fibers. The creation was safe, easy and cost effective because it involved no chemical processes. However, conducting fusion splicing on a sensor that has a significant air cavity requires appropriate splicing recipes to be created to ensure a fusion of two fibers that is good and to ensure the enclosed air cavity's mechanical and structural integrity are maintained. Furthermore, expansion and deformation can occur during the splicing [47].

A pressure sensor based on a diaphragm created using an fs laser can detect a pressure of 0.7 MPa [74]. An EFPI pressure sensor based on a microdiaphragm comprises an SMF optical fiber of silica glass, a glass diaphragm, and a glass capillary. The components are fused by utilizing a fusion splicer developed to measure pressure within the range of 14.5 psi [91].

Similar to chemical etching and splicing, laser micromachining also reduces the mechanical strengths of fibers. A strong thermal effect of laser pulses is the main limitation in fabricating EFPI sensors with precise air gaps [40]. Such sensors typically have the usual drawbacks of a high cost and complex manufacturing. However, all the mentioned drawbacks led researchers to fabricate fiber-end diaphragm-based EFPI pressure sensors [9].

The benefits of fiber-end FPI optic sensors include a high sensitivity, small size and capability of remote sensing; they are desirable in numerous applications of sensing. One can easily extend these benefits to other uses and functions of pressure sensors that are interferometric and fiber optic [54]. Different methods have been investigated to fabricate fiber-end structures.

By aligning an optical fiber with a diaphragm attached to the end of a ferrule, then using a ferrule of fused silica and the technology of CO2 laser-heating bonding, researchers created an EFPI [81]. In this case, there was no strain on the EFPI sensor, and deformation of the diaphragm directly corresponded to the phase changes of the EFPI. Similar to other EFPIs, it has the advantage of a cross-sensitivity to low temperatures of 0.013 nm/°C and a 36.54 nm/psi pressure sensitivity [92]. However, fusion splicing is the main drawback [47].

Another configuration of a fiber-end diaphragm-based EFPI pressure sensor was fabricated with the help of MEMS techniques [62], such as the standard lithography process [94] and the bulk micromachining technique [64]. In this configuration, there was a hole in one wafer or substrate that formed an FPI cavity when the wafer was bonded to another substrate. Several kinds of EFPI

pressure sensors that use optical fibers and are based on MEMS have been discussed in extant literature, such as sensors made using silicon [96][97][98][99][100][101][102][103][104], SU-8 biocompatible polymers [105][106][107][108], sapphire [102][109][110][111] and ceramic materials [18]. These discussions have concerned their uses and mechanical properties.

MEMS technology has many benefits because it has a significant economical manufacturing potential [112]. Ma et al. [67] developed an EFPI pressure sensor based on a diaphragm using a MEMS technique. A silicon diaphragm was fabricated from a micromachined silicon wafer and was coated with a highly reflective thin film mounted on a Pyrex-glass substrate. An optical fiber was then fixed on another such substrate, and both were anodically bonded together. Finally, a homemade demodulator was used to measure pressure up to 145 psi. The authors reported a higher 0.002% resolution with respect to pressure sensing compared with a similar structure for a sensor that had been reported. In a similar study, Yin et al. [113] used a silicon diaphragm to propose an EFPI pressure sensor with the help of a MEMS fabrication technique to measure pressure of 1.45–36.25 psi.

Ge et al. [104] created an EFPI pressure sensor that has a 0–14.5 psi range and a 0.5 nm/psi sensitivity based on a MEMS technique. A thin silicon diaphragm was etched with the help of a lithography technique and was then anodically bonded to a glass tube. The finite-element method (FEM) was utilized for a comparison of analytical and experimental analyses. The researchers' results showed that the theoretical deflection agreed with experimental data. Thus, they concluded that using the FEM by considering a real structure is necessary. Brace et al. [103] studied the effects of support material on a MEMS pressure sensor by developing an EFPI pressure sensor that is packaged with an industrial stainless-steel housing. A comparison showed that an analytical model did not correctly reveal the support's impact. An empirical model with a non-linear term

was proposed to address the deflection properly. The sensor can stand pressure up to 1,000 psi, although the stainless-steel housing needs modifications to support the fiber better.

It is evident from the above discussion that silicon has been used frequently for diaphragm fabrications because of its unique mechanical properties [114]. However, in hostile environments, when a pressure sensor is exposed to corrosion, a silicon diaphragm has limited applications due to a poor corrosion resistance [115][116]. Hence, different materials that are silicon compatible, including silicon-on-insulator (SOI) and silicon carbide (SiC) diaphragms, have been studied for uses in difficult environments using micromachining technology [117][118][119].

Table 2. A summary of diaphragm-based EFPI pressure sensors.

Author(s)	Year	Material	Range (psi)	Sensitivity (nm/psi)	Fabrication method
Cibula et al. [54]	2009	Silica	0–1,015	68.94	Chemical etching
Ma [98]	2020	Silicon	0–145	11.017	MEMS technique
Li [99]	2006	Silicon	29–145	0.0068	Bulk and surface MEMS techniques
Ge et al. [100]	2008	Silicon	0–435	Not reported	MEMS technique
Jia et al. [101]	2018	Silicon	0–72.5	56.14–58.6	Anodically bonding a local wafer that was made of silicon and was gold-plated to a micromachined wafer of Pyrex glass
Ge et al. [104]	2018	Silicon	0–14.5	0.51	MEMS technique

3.2 Summary

This section reviewed numerous EFPI pressure sensors in relation to their creation, configurations and techniques for sensing. This discussion had two sections, which were diaphragm-based structures and diaphragm-free structures. The former work was based on both

FP cavity-length variations and RI variations of gas. Many EFPI diaphragm-free sensor studies investigated variations in cavity length, and the sensors have pressure sensitivities that are quite low in comparison to sensors that use thin diaphragms. EFPI configurations for sensors based on diaphragms demonstrate a better performance for pressure sensing.

The literature review on fiber optic sensing mainly focused on pressure measurements, but the objective of this thesis was to measure not only pressure but also temperature. Speaking technically, while there is no interference between temperature and other parameters, such as strain, all the FPI configurations discussed in this chapter can be used for temperature sensing.

Great contributions have been made to design and fabricate a reliable and practical FPI sensor. However, as discussed above, the current developed sensors suffer from low mechanical strengths, a lack of repeatability and a lack of stability. Most of the reported FPI sensors are based on wavelength detection, which needs a spectrometer and is extremely expensive. To design an FPI sensor, it is also necessary to consider the value and cost of a system for end customers. The object of this thesis was to design and fabricate a reliable and stable self-temperature-compensated FPI sensor for simultaneous temperature and pressure measurements. Material selection, structure, sensor housing, cost and fabrication were considered in the design of the sensor.

The main focuses of this thesis were as follows.

1. The development of intensity-based interrogation methods that have the potential to be used to manufacture FPI sensors cheaply in massive quantities while offering superior performance characteristics.
2. The development of a temperature-sensing EFPI device.

3. The development of self-temperature-compensated sensors for detecting pressure. Because temperature has a significant effect on FPI pressure-sensor readout signals, four main strategies were used to develop these sensors:
    i. The use of a diaphragm-based configuration using an SOI wafer for the membrane.
    ii. The use of extrinsic FPI sensors, which have low temperature sensitivities.
    iii. The design of a uniquely packaged FPI structure so that the temperature effect can be compensated for.
    iv. The use of an intensity-based interrogation method to arrive at a cost effective FPI sensor.

A more detailed literature review of EFPI temperature sensing mechanism is given in the following chapter.

4 An Extrinsic FPI Temperature Sensor based on the Thermo-Optic Effect Using a Cost-Effective Signal-Demodulation Method

The basis of this chapter is an unpublished manuscript by the author that is pending submission in a journal; its title is "An Extrinsic Fabry–Pérot Interferometric Temperature Sensor based on the Thermo-Optic Effect Using a Cost-Effective Signal-Demodulation Method."

4.1 Introduction

As aforementioned, the intrinsic advantages of FFPI sensors include an immunity to EM fields, remote sensing ability and small size and weight; these benefits have caused an increased interest in using FPI temperature sensors [6][120]. Fiber optic temperature sensors do not use metal transducers to perform their conversions [121]. This allows for a minimal thermal dissipation through conduction and provides a quick response and extreme accuracy [11] that drives a need for the use of FPI temperature sensors instead of conventional ones, such as thermistors and thermocouples [122]. FPI temperature-sensing devices are categorized into two main types based on their working principles.

The first type is based on FP cavity-length variations due to thermal expansion [123]. The second type relies on the TOE, whereby a temperature change, ΔT, induces variations in either the refractive index of a material (n) or causes a wavelength shift ($\Delta\lambda/\Delta T$) in a spectral response due to changes in the phase of reflected light [124]. In both configurations, light is conveyed by a fiber from an emitter to an interferometer; it is also conveyed from an interferometer to a detector [13].

In the first type of FFPI temperature sensor, the FP cavity can be developed either inside an optical fiber, where modulation takes place directly in the fiber, or in any medium, such as a solid material or an air gap. Fusion splicing, which is a widely used method in FPI sensor fabrication, can also be utilized to form an FP cavity inside optical fibers by fusion splicing two coated fibers [47], two chemically etched fibers [125][126] or two different types of fibers together [127][128][129][130][131][132][133].

Zhu et al. [127] fusion spliced a section of solid PBF to an SMF and were able to fabricate an FPI temperature sensor that could measure a temperature range of −20°C to 1,200°C. Yang et al. [134] developed an extrinsic FPI temperature-sensing device formed in a mercury-filled silica tube. The mercury-filled tube was fusion spliced with an SMF. The mercury surface and the end face of the SMF formed an FPI. When a temperature increased, the volume of the mercury expanded, and therefore, the FP cavity length decreased.

As pointed out before, the most prominent advantage of fusion splicing is its low-cost fabrication. However, fusion-spliced fibers lack repeatability, and the final performance of an FPI sensor depends significantly upon the splicing process. Other methods to create an FP cavity include focused ion-beam (FIB) micromachining [100], FIB milling technology [101], microfabrication [137] and fiber Bragg grating FPI [44] sensor fabrication. These processes require neither cleaving nor splicing over the sensor region; however, the fabrication steps are complicated. In addition, signal demodulation is a significant disadvantage of these kinds of developed sensors.

In the second type of FPI temperature-sensing devices, the thermo-optic characteristics of materials can be used to fabricate optical temperature sensors [138]. Silicon is a desirable sensor material that shows not only a notable TOC ($\frac{\partial n_{si}}{\partial T} = 1.86 \times 10^{-4}\ K^{-1}$ at a 1.55 μm wavelength)

[139] but also has unique properties, i.e., a large thermal diffusivity, low thermal-expansion coefficients and a high thermal stability [140]. There is a wide body of literature that has discussed the use of the TOE of silicon for sensing devices [10][141][142][143][144]. Wolthuis et al. [10] developed an FPI temperature sensor that consists of a silicon wafer sandwiched between two glass substrates. With an increase in temperature, the silicon's refractive index (n_{si}), and consequently, the phase shift of the reflected beam from the FPI, vary with temperature changes. Ge et al. [141] anodically bonded a silicon wafer on a glass fiber to develop a similar structure; the silicon's thermo-optic characteristics changed, and this in turn led to a shift in the reflected spectra for measuring temperatures in the range of 20–48°C. In other similar work based on the silicon TOE, a small silicon cylinder mounted on the end face of an SMF served as an FPI that sends back an interferometric spectrum that is sensitive to the silicon's temperature [142].

In all the literature reviewed above, the TOE has been seen mainly as a wavelength change ($\Delta\lambda/\Delta T$) in a spectral response that is induced by temperature. A constant value is usually considered for the value of n_{si} for a wavelength range of interest [139][140][141][142][144][145]. To measure a wavelength shift, a spectrometer is typically used; interference spectra are analyzed by utilizing the fast Fourier transform (FFT), which makes this technology complex and expensive. Though it has been recognized that n_{si} changes with both wavelength and temperature, refractive-index changes with temperature are rarely considered when developing temperature-sensing devices [146].

In this chapter, an extrinsic FPI temperature sensor is presented that is based on the thermo-optic properties of silicon by using an SOI wafer. A cost-effective signal demodulation method was used to investigate the refractive-index variation of silicon as it was heated from an ambient temperature to 100°C. An analytical model was used to simulate the experimental results. A TOC

extracted from experimental data was compared with the published literature to validate the accuracy of the proposed device. The temperature device features a protective stainless-steel housing that protects the optical fiber and SOI wafer. Results show that the sensor described in this chapter is a precise, durable device at an affordable cost.

4.2 Theory

The principal operation of FPI sensors is multiple reflections that happen between two mirrors in an FP cavity. Interactions between the transmitting and reflecting waves cause either constructive or destructive interference, which causes the reflected light's intensity to vary. The Airy formula is used to expresses the fraction of reflected light, as shown in (8) [103][27]:

$$\frac{I_R}{I_o} = \frac{R_1 + R_2 + 2 \cdot \sqrt{R_1 R_2} cos\phi}{1 + R_2 R_1 + 2 \cdot \sqrt{R_1 R_2}\, cos\, \phi}, \tag{8}$$

where I_R and I_o represent the reflected and initial intensities, respectively. R_1 and R_2 are the normal reflectivities of the etalon surfaces, and ϕ gives the round-trip phase shift of the fundamental mode.

$\phi's$ and R's values are simply given by using (9) and (10):

$$\phi = \frac{2\pi nL}{\lambda} \tag{9}$$

and

$$R = \left(\frac{n_i - n_t}{n_i + n_t}\right)^2, \tag{10}$$

where n is the FP-cavity material's refractive index, L represents the length between the mirrors, λ provides the light's wavelength and n_t and n_i are the incident medium's refraction index and the transmitted medium's refraction index, respectively.

Consider I as the fraction of reflected light ($I = \frac{I_R}{I_o}$) in (8). Because the TOE determines a phase change, according to (9), I will undergo a modulation showing a periodic pattern that has I_{max} (maximum) and I_{min} (minimum) amounts correspondingly at the two-phase conditions $\emptyset = m\pi$ and $\emptyset = (m + 1/2)\pi$, with m being an integer. Thus, the modulation depth (a significant parameter that characterizes the FP cavity) is:

$$M = \frac{I_{max} - I_{min}}{I_{max}} \tag{11}$$

A higher modulation depth can be noted in a good-quality cavity composed of smooth and parallel surfaces, which have low losses.

Moreover, in (9), ϕ has a double temperature dependence on both the refractive index variation and the thermal expansion. Therefore, differentiating (9)with respect to T gives [122]:

$$\frac{\partial \emptyset}{\partial T} = \frac{2\pi L}{\lambda}\frac{\partial n}{\partial T} + \frac{2\pi n}{\lambda}\frac{\partial L}{\partial T} = \frac{2\pi L}{\lambda}\left(\frac{\partial n}{\partial T} + \alpha n\right), \tag{12}$$

where the term $\alpha = \partial L / L\partial T$ is the thermal expansion coefficient. In equation (2), ϕ has a double temperature dependence on both refractive index variations and thermal expansion, however; the thermal expansion coefficient of silicon (an average value of $2.5 \times 10^{-6} K^{-1}$) is two magnitude orders tinier in comparison with the TOC (an average value of $1.86 \times 10^{-4}\ K^{-1}$). Furthermore, the silicon's refractive index varies significantly with temperature when the wavelength of the considered light is near the silicon band gap [10].

4.3 Device Structure and System Configuration

The device structure includes a sensitive part, an optical fiber as a signal carrier and packaging that aligns the optical fiber with the silicon (the sensitive part). These parts are explained in the next two subsections.

4.3.1 Sensing Mechanism

Due to the unique properties of an SOI platform, including the capability of mass production at an affordable cost [1][147][148], and the possibility of later integration with a membrane for added pressure sensing capabilities, an SOI wafer was selected for the sensing mechanism of the extrinsic FPI temperature sensor, as schematically displayed in Fig. 16 (a). The SOI wafer (5.5 mm × 5.5 mm square) is comprised of three individual layers: a single-crystal silicon layer (400 μm thick), an insulating layer of silicon oxide (2 μm) and another single-crystal silicon layer (25 μm thick). All the SOI chips used in testing and preparing the presented temperature-sensing device were fabricated using the silicon-on-insulator multi-user MEMS process (SOIMUMP) approach offered by MEMSCAP. The full fabrication details can be found in Revision 8 of the *SOIMUMP Design Handbook* [116][16].

4.3.2 Packaging

A stainless-steel packaging was fabricated for the temperature-sensing device. A square pocket with a width of 5.5 mm was drilled on top of the housing (Fig. 16. (b)), and an SOI chip was placed inside. The other side of the packaging features a slot to which an FIS SMA905 stainless-steel connector (127 μm; Fiber Instrument Sales Inc., USA) [114][115] was attached; an optical fiber was then inserted inside the connector, as displayed in Fig. 16. (c). To position the optical fiber's tip, a threaded locating component was used, removing any additional space between the fiber and

SOI wafer. The packaging is schematically shown in Fig. 16 (In appendix, Fig. 43 presents drawing of the device with the dimensions in detail). The real device's structural parts and the device's assembly are shown in Fig. 17.

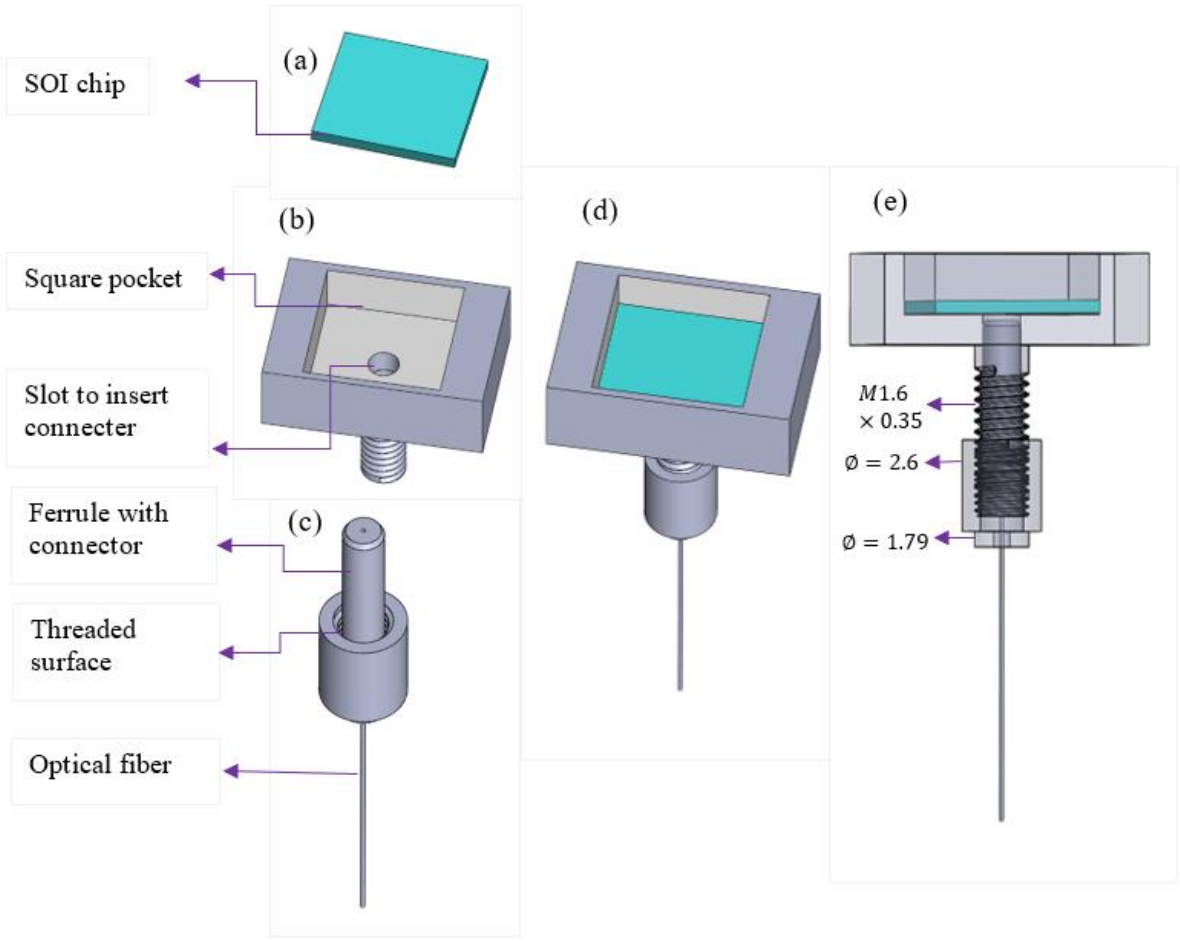

Fig. 16. The packaging assembly: (a) the SOI chip, (b) the housing, (c) the connector with the optical fiber inserted in the ferrule, (d) a full isometric view of the packaging and (d) a transparent view of the assembly with dimensions in mm.

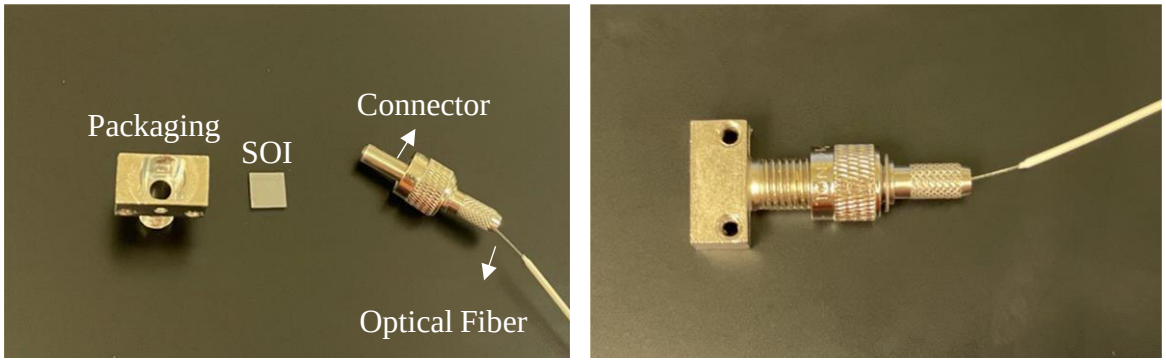

Fig. 17. (Left) The device's structural parts and (right) the full sensor-packaging assembly.

4.4 Experimental Setup

The experimental setup is schematically presented in Fig. 18. The sensing system was configured based on the intensity-interrogation method [151]. A DC power supply source (E3631A, Agilent) was used to provide power for an 850 nm laser light-emitting diode (LED) (OPV314AT, TT Electronics [152]) via a breadboard. Light generated from the LED source was passed through a 2:1 Y-coupler. The 2:1 Y-coupler, which is a passive device that splits and combines an optical signal, was used in the experiment to transmit and receive light from the FP cavity. The other split ends of the Y-coupler were connected to an in-house optical sensor interrogator (OSI) [153] with a built-in photodiode for measuring the intensity of the reflected light coming from the Y-coupler's single end. The single end was directed to the FP cavity in the sensing device. In the FP cavity, light beams undergo internal reflection. Then, the reflected light from the surface of the SOI wafer is recollected with the optical fiber. After passing through the coupler again, the signal is redirected to the OSI.

The gain and sampling rates of the photodiodes in the OSIs were optimized to achieve an optical signal with a high resolution and avoid the saturation of the signal. MATLAB (v. R2021b) was

configured to retrieve the signals from the OSI, provide a live plot of the measurements and store the data for further analyses. The temperature-sensing device was placed in a furnace box (Thermo Scientific Lindberg/Blue M Moldatherm Box Furnaces) [154] on top of a thermal brick. At the same time, a USB-TC01 temperature-input device (thermocouple) [155] was connected to the surface of the SOI wafer to record the temperature as a reference.

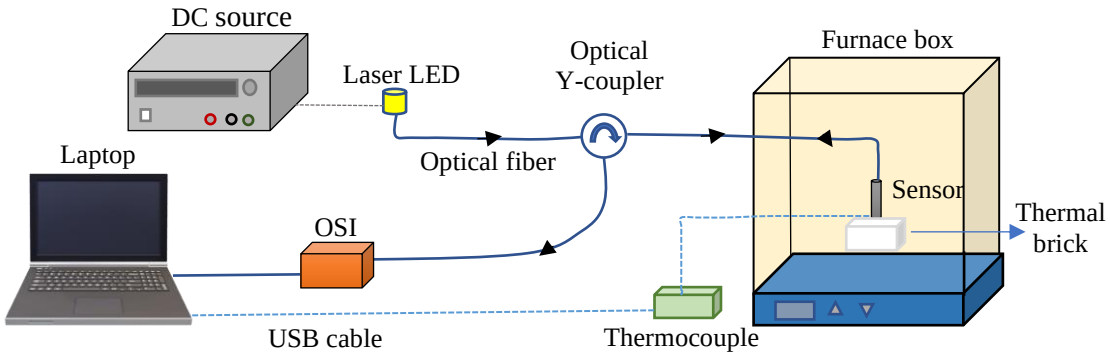

Fig. 18. A schematic diagram of the experimental setup for temperature sensing.

For experiments, three 2:1 SM Y-couplers and one 2:1 multi-mode Y-coupler were used [118]. The following table summarizes the couplers' features.

Table 3. A summary of the couplers used in the experiments.

Fiber Type	Name (in this Chapter)	Splitting Ratio	Ratio Connected to the Receiver (OSI)	Ratio Connected to the Source (LED)
SM	SM 50/50	50/50	50	50
SM	SM 80/20	80/20	20	80
SM	SM 90/10	90/10	90	10
Multi-mode	MM 50/50	50/50	50	50

4.5 Experimental Results

First, the experimental results were collected from an ambient temperature to 100°C in steps of 1°C using the 2:1 SM Y-coupler with a splitting ratio of 50/50 (SM 50/50). The voltage,

determined by using the OSI, was recorded and plotted versus the temperature recorded through the thermocouple (Fig. 19).

Then, the remaining two 2:1 SM Y-couplers and the 2:1 MM Y-coupler were used in the experiments [118]. The experiments were conducted from room temperature to 100°C. Fig. 20 displays the intensity variation with respect to temperature from 50°C to 60°C. A temperature of 10°C in the middle testing range was selected to produce clear plots. The experimental results, which are shown with solid dots, are connected through a solid line.

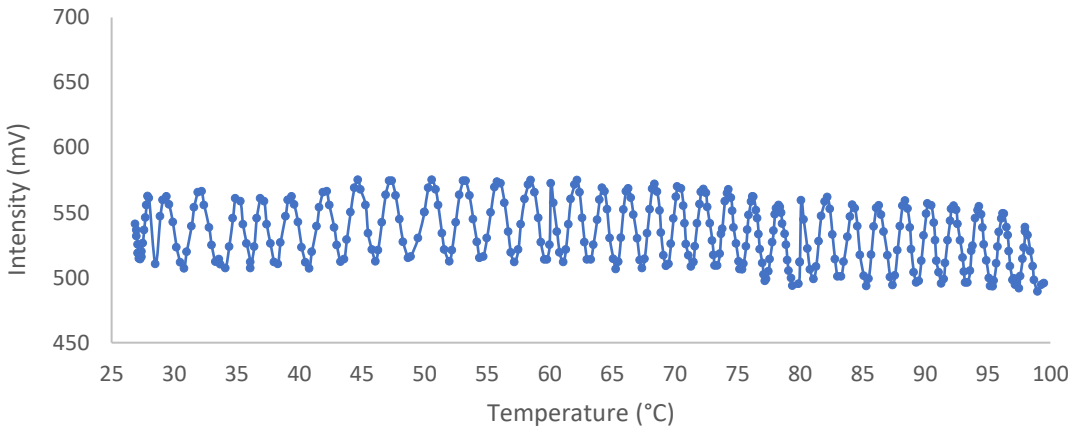

Fig. 19. The SOI voltage responses when evaluated at a range of 0–100°C within the furnace box. The solid dots present experimental results. The solid blue line is the connection line.

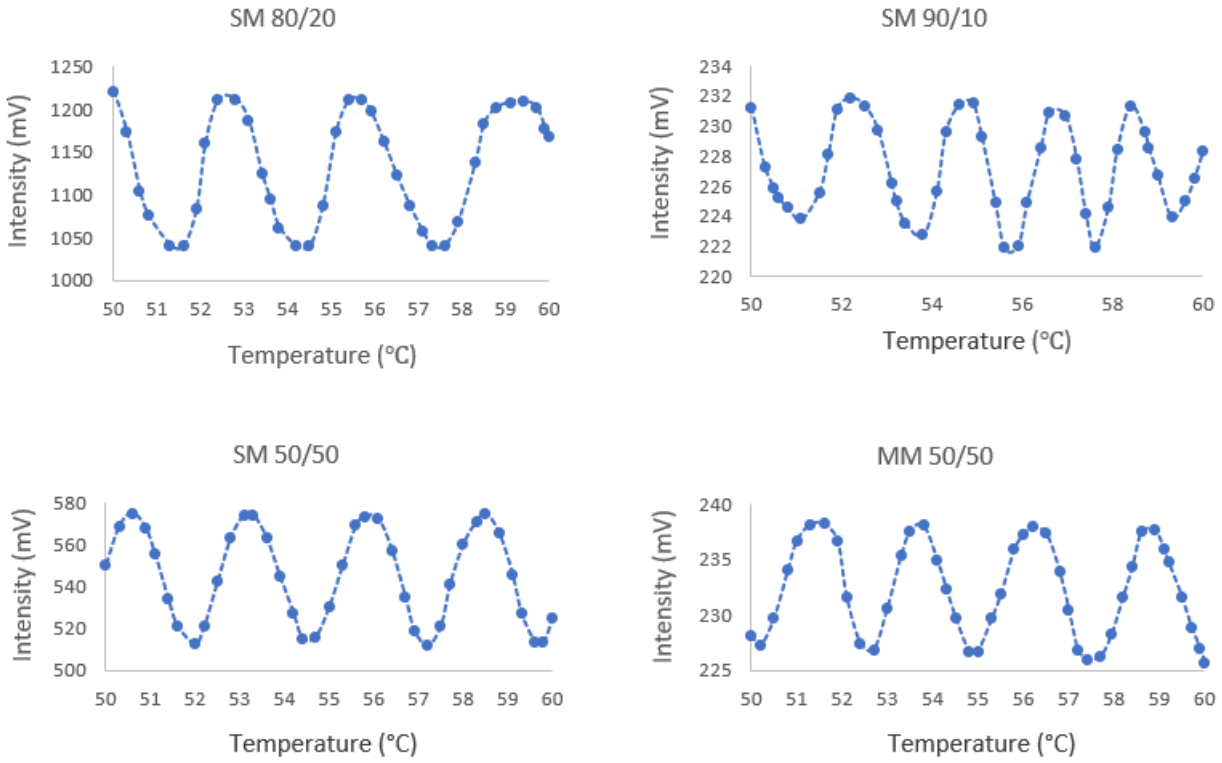

Fig. 20. A comparison of the voltage responses of the FPI temperature device from 50°C to 60°C in the furnace box with the four Y-couplers.

4.6 Discussion of Results

Following the testing results, this section provides an analysis and discussion of the sensitivity, resolution, modulation depth and thermo-optic coefficient. Since sensors cannot reproduce an ideal transfer function, a sensitivity analysis is helpful to study sensors' accuracy. Moreover, as pointed out in section 4.2, modulation depth is a significant parameter that characterizes FP cavities, and the thermo-optic coefficient is extracted to emphasize the accuracy of a sensor.

4.6.1 Sensitivity Analysis

A sensor's sensitivity is the output signal to measured property ratio [157]. Sensitivity denotes how a system can detect a signal at a particular level. The larger a value of sensitivity is, the more favorable the system's performance is [158]. For a temperature sensor based on an FPI, one can estimate the sensitivity by fitting the slope of the experimental data [128]. The linear range and its linear fitting is plotted in Fig. 21.

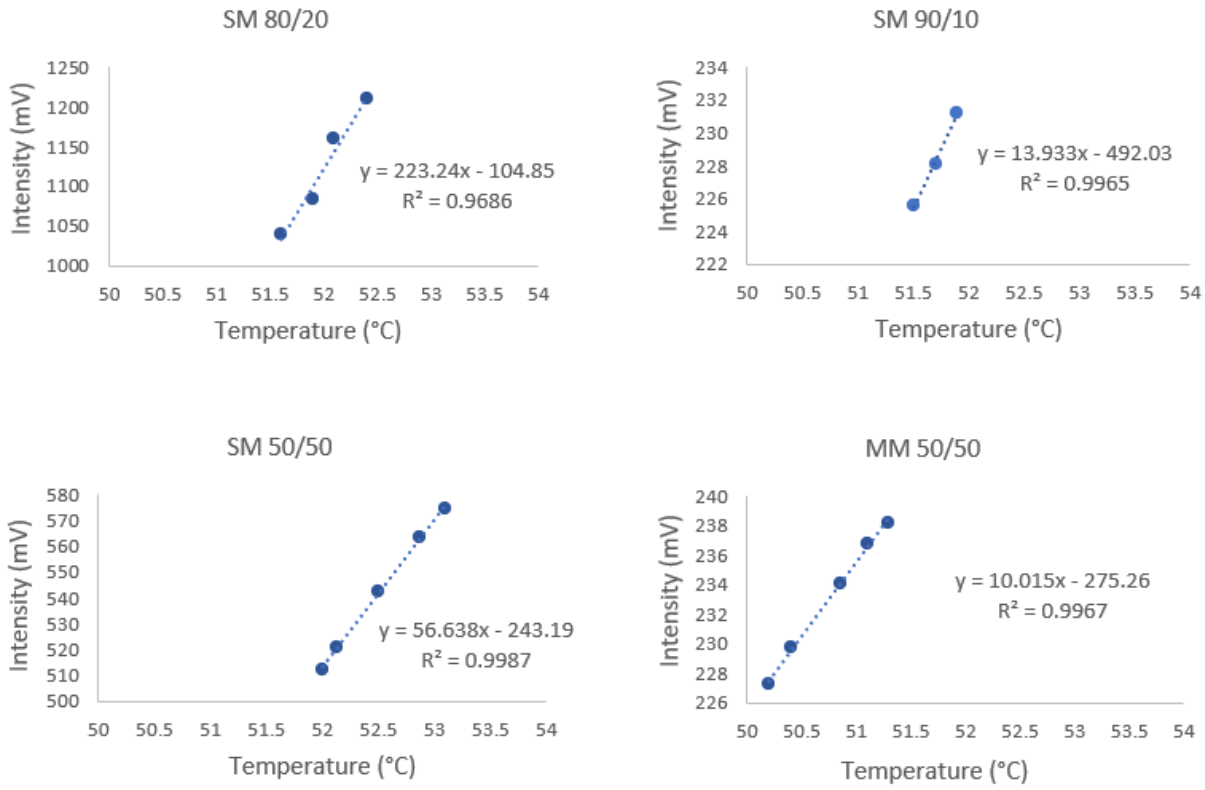

Fig. 21. A comparison of sensitivities of the four Y-couplers.

Using a linear regression model, the values of R square (R^2), or goodness-of-fit measure, were found to be 0.996, 0.968, 0.998 and 0.996 and the sensitivities for each of the four Y-couplers were approximately 10.015 mV/°C, 223.24 mV/°C, 56.63 mV/°C and 13.93 mV/°C, respectively.

To obtain a better judgement about the performance of the developed sensor, the sensitivity was also compared with available commercial temperature sensors. Four different kinds of temperature sensors are the most popular for today's electronics: resistance temperature detectors, thermocouples, semi-conductor-based integrated circuits and thermistors[160][161][162]. The most popular of these are thermocouples, which are created by connecting two different metal wires that are dissimilar. The result is a phenomenon called the Seebeck effect, wherein the difference in temperature between the two wires, i.e., conductors, that are dissimilar results in a difference in voltage betwixt the two different substances. One can measure the latter and utilize it in order to determine the temperature [162]. A plethora of thermocouples exist, all made from diverse materials, and as a result, various sensitivities and ranges of temperature can be measured. These thermocouples are distinguished from each other by using certain letters. The most popular kind of thermocouple is the K kind, which has a 0.041 mV/°C sensitivity.

The following Table 4 [163] shows a comparison of some of the most popular thermocouples sensitivities with respect to the developed sensors. It can be easily seen that the sensitivity of the developed sensor is higher than the sensitivities of all the different thermocouples listed and that are available commercially.

Table 4. A comparison of the sensitivity of different thermocouple types extracted from [163] and the developed temperature sensors.

Sensor	Type	Conduction Alley (+/−)/Splitting Ratio	Sensitivity (mV/°C)
Thermocouple	E	Nickel chromium/constantan	0.068
	J	Iron/constantan	0.055
	K	Nickel chromium/nickel aluminum	0.041
	N	Nikrosil/nisil	0.039
	T	Copper/constantan	0.043
	R/S	Copper/copper nickel compensating	0.010
	B	Platinum rhodium	0.010
This Work	SM	80/20	223.24
	SM	90/10	13.93
	SM	50/50	56.63
	MM	50/50	10.013

4.6.2 Resolution Analysis

The tiniest differentiable alteration that the sensor can determine, and show is called resolution. Larger resolutions (thereby, tinier observable and showable alterations) result in more values that are specific. The standard deviation (SD) of a signal, shown using a unit of measurement, divided by the sensitivity of the sensor typically equals its resolution. Therefore, one can determine the latter using the following equation [164][165]:

$$\text{Resolution} = \text{SD} / \text{Sensitivity} \tag{13}$$

The SD can be determined by using the square root of a value that can be found through a comparison of points of data and a population's overall mean as follows [166]:

$$\text{SD} = \sqrt{\frac{\sum_{i=1}^{x}(Y_i - \bar{Y})^2}{x-1}}, \tag{14}$$

where x denotes the data set's number of data points, $\bar{Y}$ denotes the mean data set value and Y_i denotes the value of the data set's i-th point.

The SD for the four Y-couplers, as listed in Table 5, can be determined from the measured voltage at a particular temperature for the range plotted in Fig. 21 using equation (14). Using equation (13), the resolution for a specific temperature of 51°C, for example, are calculated as 0.003 °C, 0.05 °C, 0.01°C and 0.07 °C, respectively. Table 5 shows a comparison of the resolution for the different Y-couplers investigated at a temperature of 51°C. SM 80/20 shows the highest sensitivity and the smallest resolution. However, SM 50/50 was found to have a more stable signal.

Table 5. A comparison of the resolution for the different Y-couplers investigated at a temperature of 51°C

Coupler Type	SD (mV)	Resolution (°C)
SM 80/20	0.75	0.003
SM 90/10	0.71	0.05
SM 50/50	0.68	0.01
MM 50/50	0.79	0.07

4.6.3 Modulation Depth

Based on equation (11) in Section 4.2, the modulation depth was calculated for all couplers and tabulated in Table 6. From this table, it can be observed that the SM 80/20 Y-coupler has the highest modulation depth, while the SM 90/10 Y-coupler has the lowest modulation depth. Although SM 50/50 displayed a lower modulation depth than SM 80/20, the results for this coupler showed a more normal distribution. Therefore, SM 50/50 was selected for the optical coupler.

Table 6. A comparison of the modulation depths extracted from the experimental data.

Coupler Type	I_{max}	I_{min}	M(Modulation depth)
SM 80/20	1220.789	1040.052	0.148049
SM 90/10	232.1719	221.8866	0.0443
SM 50/50	575.1292	511.7942	0.110123
MM 50/50	238.2543	224.8092	0.056432

4.6.4 Thermo-Optic Coefficient

Silicon's TOC, published by Cocorullo et al. in 1999 [145] and shown below as a second-order polynomial in (15), was considered as a reference for this work.

$$\frac{\partial n}{\partial T} = 9.48 \times 10^{-5} + 3.47 \times 10^{-7} \times T - 1.49 \times 10^{-10} \times T^2 \, (K^{-1}), \tag{15}$$

where n is the refractive index and T is the temperature. To extract TOCs from the experimental data, ΔT_π needed to be obtained. Once ΔT_π, which induces $\Delta\emptyset = \pi$, i.e., once the distance between two transmission maximums, was obtained, one could invert (12) in order to determine the material's thermo-optic coefficient [167] as shown in (16):

$$\frac{\partial n}{\partial T} = \frac{\lambda}{2L\Delta T_\pi} - n\left(\frac{1}{L}\frac{\partial L}{\partial T}\right). \tag{16}$$

Considering Fig. 19, $\Delta T_\pi = 2.3K$, and for $\lambda = 850$ nm, $l = 1$ mm, $n = 3.6$ and $\alpha = 2.5 \times 10^{-6}K^{-1}$, so $\partial n/\partial T = 1.8514 \times 10^{-4}K^{-1}$. This is equal to the silicon's thermo-optic coefficient value at a 300–304 K (~27–31°C) temperature range.

Similarly, the silicon's thermo-optic coefficient, in all ranges of temperature, was obtained by measuring the transition from a maximum of transmission to a minimum and inserting the value for the silicon's refractive index at corresponding temperatures. In this thesis, the silicon's

refractive-index temperature dependence was obtained using the values published by Hi in 1980 [120] and the empirical model developed by Xu et al. in 2019 [146]. The results of extracting the TOC from the experimental data are displayed in Fig. 22 with orange dots.

To verify the accuracy of the obtained TOCs, the results were compared with the values published by Cocorullo et al. in 1999 [145]; these values were plotted by using (15) and are shown with a solid blue line in Fig. 22.

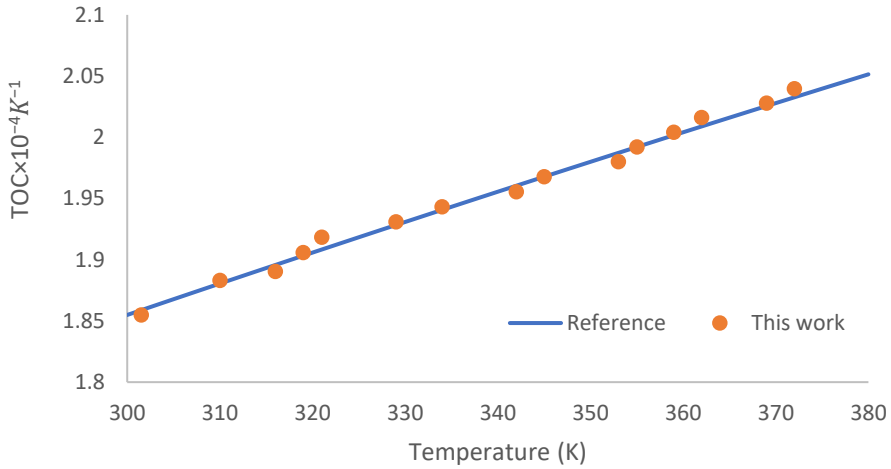

Fig. 22. A comparison of the TOCs extracted from the experimental data and data available in the reference literature [110].

The results extracted from the experimental data were in good agreement with the data that is published. For data comparison, the mean squared error (MSE) [169][170], was determined as,

$$MSE = \frac{1}{x}\sum_{i=1}^{x}(Y_i - \widehat{Y}_i)^2 \,, \tag{17}$$

where $\widehat{Y}_i$ denotes the values that were predicted (determined using the experimental data), x denotes the number of data points and Y_i denotes the values that were observed (determined using the reference). The determined MSE for the data shown in Fig. 22 is 2.15E-05, which is close to

zero and proves that the experimental data is in good agreement with the literature, thus verifying the developed FPI temperature-sensing device's accuracy.

4.7 Summary

An extrinsic FFPI temperature sensor was developed and evaluated. This sensor was based on the TOE in the temperature range of 0–100°C. The limited temperature range was because of the optical fiber (for high temperatures, a specific optical fiber must be used). An SOI wafer, which is a batch-producible platform, was used for the development of the device. For recording variations in the refractive index of the silicon in response to an increasing temperature, a cost-effective signal modulation method based on a photodiode was used. By forgoing the need for packaging optical devices, the developed temperature sensor features a protective stainless-steel packaging with a threaded locating component to connect an optical fiber through a connector. The TOC of the silicon was theoretically and experimentally investigated. A comparison demonstrated an agreement between the TOC extracted from the experimental data and such a coefficient in the published literature. The modulation depth of the device was then studied by using different couplers with different splitting ratios. While an SM coupler with a split ratio of 80/20 shows the highest modulation depth, a 50/50 SM coupler results in a more uniform and normal intensity distribution. The sensitivities and resolutions for different couplers were investigated. For the SM 50/50 coupler, the values were 56.63 mV/°C and 0.01°C, respectively. The developed device is a promising platform for the mass-scale production of a silicon FPI temperature apparatus, which has a cost-effective optical-signal demodulation method. The integration of pressure measurements and temperature sensing is investigated in the next chapter.

5 A Packaged Temperature and Pressure-Sensing Extrinsic Fabry–Pérot Interferometer MEMS Device for Harsh Environments with Self-Temperature-Compensation

The basis of this chapter is a manuscript by the author that is pending for submission in a journal; it is titled “Packaged Temperature and Pressure-Sensing Extrinsic FPI MEMS Device for Harsh Environments with Self-Temperature-Compensation.”

5.1 Introduction

As aforementioned, sensors are used regularly in various sectors, including industry, energy and health care. They are crucial for measuring different parameters and understanding when something might go wrong [1]. Two of the most commonly measured parameters are pressure and temperature. Measuring pressure is key in a wide variety of technologies and application areas ranging from health care for detecting hypertension [10] to fuel tank pressure monitoring in space shuttles [171]. Temperature detection also plays a significant role in energy-saving systems and in the monitoring of production processes during which temperature is influential [10]. As aforementioned, the literature offers numerous examples of sensors capable of measuring either temperature [125][172][173] or pressure [37][27]; however, few sensors have been created for use in both high-pressure and elevated-temperature environments. The demand for such a device for parameter measurements, especially in harsh environments, is on a constant rise. The development of a reliable long-term temperature- and pressure-monitoring device would bring substantial value to various industries, thereby supporting investment in such a measurement system.

MEMS technology is gaining interest for use in hostile environments in different industries due to the unique properties of MEMS devices, which, as aforementioned, include a small size, light weight, high accuracy and high resolution [4]. However, the commonly used technologies have a number of reported challenges. The performance of the current industrial piezoresistive [123][175] and capacitive [176][177] MEMS pressure-sensing systems is impacted by temperature, which can disrupt the performance and accuracy of such a device and destabilize sensing elements. Moreover, conventional temperature-sensing devices, such as thermistors and thermocouples, must often operate in or near intense EM fields or at long distances. In such environments, sensors with metal leads are prone to experience eddy currents [178][179][180]. This may cause noise and the heating of such a sensor, which can lead to inaccurate temperature measurements.

These shortcomings are driving a need for the use of optical sensing devices instead of conventional ones. As previously noted, the intrinsic advantages of fiber optic sensors make them attractive for measurements even in harsh environments [130][182]. A combination of MEMS and fiber optics may therefore pave the way for novel sensing concepts and applications.

One of the most effective methods of combining a versatile optical fiber with MEMS is using FPIs [8]. Several researchers have employed extrinsic FPI schemes to investigate multi-parameter temperature and pressure sensors. Jinde et al. [113] were able to develop an FPI configuration for simultaneous temperature and pressure sensing by bonding a silicon wafer, a glass substrate and a silicon membrane together. The silicon wafer formed a temperature-sensing cavity and made use of the thermo-optic properties of silicon for temperature measurements. A second cavity was formed between the silicon membrane and glass substrate to sense pressure. By using signal processing and demodulating, the reflectance spectra were analyzed to separate measurand

frequencies. Complex and expensive signal processing and a low sensing range are the drawbacks of this configuration.

Cheng et al. [183] employed the thermo-optic properties of silicon to fabricate a multi-parameter MEMS temperature and pressure sensor. An air cavity between a fiber's top surface and a membrane's bottom surface was considered one FP cavity, and silicon on the top side of the device was considered another FP cavity. Since silicon has a larger refractive index than air, the researchers noted that an optical-path difference in the output spectrum is distinguishable when an FFT is performed. The sensing range, however, was not reported. This sensor suffers from a complex and expensive structure and the signal-demodulation method to obtain a measurand. Similarly, Bing et al. [184] formed an EFPI sensor by using a polymer cap that bonded to an SMF's end. The interference fringe's wavelength shift was measured with a spectrometer.

These developed multi-parameter temperature and pressure sensors make use of the total reflection spectrum's wavelength shift, which is inherently expensive and complex, even when it is used to measure one parameter, such as pressure. It can be more complex when it is used for multi-parameter sensing. The shape and wavelength shift of the total reflection spectrum can be affected by any variation in an FP cavity. Cross-sensitivity will seriously influence the accuracies and the linearities of measurands. Thus, although the investigated sensors are capable of double-parameter sensing, the factors of complex fabrication schemes, a lack of stability, low sensing ranges and complex and expensive signal demodulation are drawbacks of the in-line cavity method.

The implementation, therefore, of a successful double-measurement device necessitates a system that can adjust to deviations in temperature and resist harsh environmental conditions while maintaining a high sensitivity to pressure. In this chapter, a stainless-steel housing is fitted with

two fiber optic FPI sensors and a silicon-on-insulator (SOI) chip to simultaneously measure temperature and pressure. The pressure-sensing FPI portion is sensitive to the deflection of the SOI chip's membrane, while the temperature-sensing FPI is sensitive to the thermo-optic properties of silicon. The device response to temperature dependence is investigated and an empirical model is developed in this work.

5.2 Theory and Working Principle

As explained in previous chapters, the principal operation of FPI sensors is multiple reflections that happen between two mirrors in an FP cavity. Interactions between the transmitting and reflecting waves cause either constructive or destructive interference, which causes the reflected light's intensity to vary. The formula for the light intensity shown in (8), and the values for ϕ and *R* are simply given in (9) and (10).

Based on (9), any change in *L*, *n* or λ will result in a phase shift, causing changes to the intensity of the reflected light. In membrane-based FPI pressure sensors, pressure causes a deflection in the membrane that changes the length of the FP cavity. For temperature sensing, as investigated in the previous chapter, ϕ in (9) has a double temperature dependence on both the refractive index variation and the thermal expansion. Therefore, differentiating (9) with respect to *T* gives [122]:

$$\frac{\partial \emptyset}{\partial T} = \frac{2\pi L}{\lambda}\frac{\partial n}{\partial T} + \frac{2\pi n}{\lambda}\frac{\partial L}{\partial T} = \frac{2\pi L}{\lambda}\left(\frac{\partial n}{\partial T} + \alpha n\right).$$

As mentioned, the term $\alpha = \partial L/L\partial T$ is the thermal-expansion coefficient, which for silicon is two orders of magnitude smaller than the TOC.

5.3 Device Structure and System Configuration

The device structure includes a SOI chip, two signal-carrying optical fibers and a unique packaging that aligns the optical fibers with the SOI chip. These parts are explained in the next two subsections.

5.3.1 SOI Chip

An SOI chip was selected due to its small form factor, ability to withstand high pressures and ability to be produced in large batches [1]. As mentioned before, SOIMUMP is a commercial fabrication process offered by MEMSCAP. All the SOI chips used in testing and preparing the presented sensor were fabricated using the SOIMUMP approach from MEMSCAP. The full fabrication details are described in Revision 8 of the *SOIMUMP Design Handbook* [116][16]. The SOI chip is produced by dicing 5.5 mm × 5.5 mm squares from a wafer consisting of three individual layers. The bottom substrate layer is a single-crystal layer of silicon (400 μm thick), followed by an insulating layer of silicon oxide (2 μm) and second single-crystal silicon layer (25 μm thick). Near the center of the SOI chip, a square space with depth of 402μm (400 μm × 400 μm × 402 μm) is etched to create a 25 μm thick silicon membrane that deflects when exposed to pressure. The unetched region of the silicon substrate is utilized for temperature sensing as its refractive index changes due to the TOE.

5.3.2 Packaging

The sensing system requires a unique packaging process to operate in harsh environments. The packaging process is designed to not only hold an SOI chip and two optical fibers but also provide support and shielding. Stainless steel was selected as the material of choice for fabricating the housing due to its strength and machinability [185][186]. The packaging consists of a core piece,

named the fiber locator, and a threaded shelter as the housing. A square pocket with a length of 5.5 mm was machined on the top section of the housing that tightly fits the SOI chip. An epoxy (EPO-TEK 353ND) with a 350°C maximum operating temperature [187] was used to hold the SOI chip inside the pocket and create a hermetic seal (shown in Fig. 23). Two holes were drilled through the housing within the formed pocket aligning the reflective SOI membrane with one of the optical fibers near the center, and the second hole exposes the second fiber to the SOI chip's substrate. The external section of the housing is threaded and consists of a 45° chamfer seal that closely resembles an earlier design by Eric et al. to meet industrial standards [103]. The housing was drilled from the bottom end to allow the insertion of the fiber locator. The locater has two stainless-steel ferrules (SFLC127; 6.4 mm long; Ø1.25 mm and Ø127-µm bore size) [135] that hold the optical fibers. Two single-mode (SM) 2:1 Y-couplers with a 50/50 split ratio and a 65 µm silica core, compatible with wavelengths of 800–900 nm, were inserted into the fiber locator [118]. A set screw was used to fix the fiber locator after adjusting the distance between the optical fibers and the SOI chip, ensuring no drifts in the fiber locator's position. (In Fig. 23, the threads are not shown in the full length of the schematic view of the packaging in order to show the set screw clearly.)

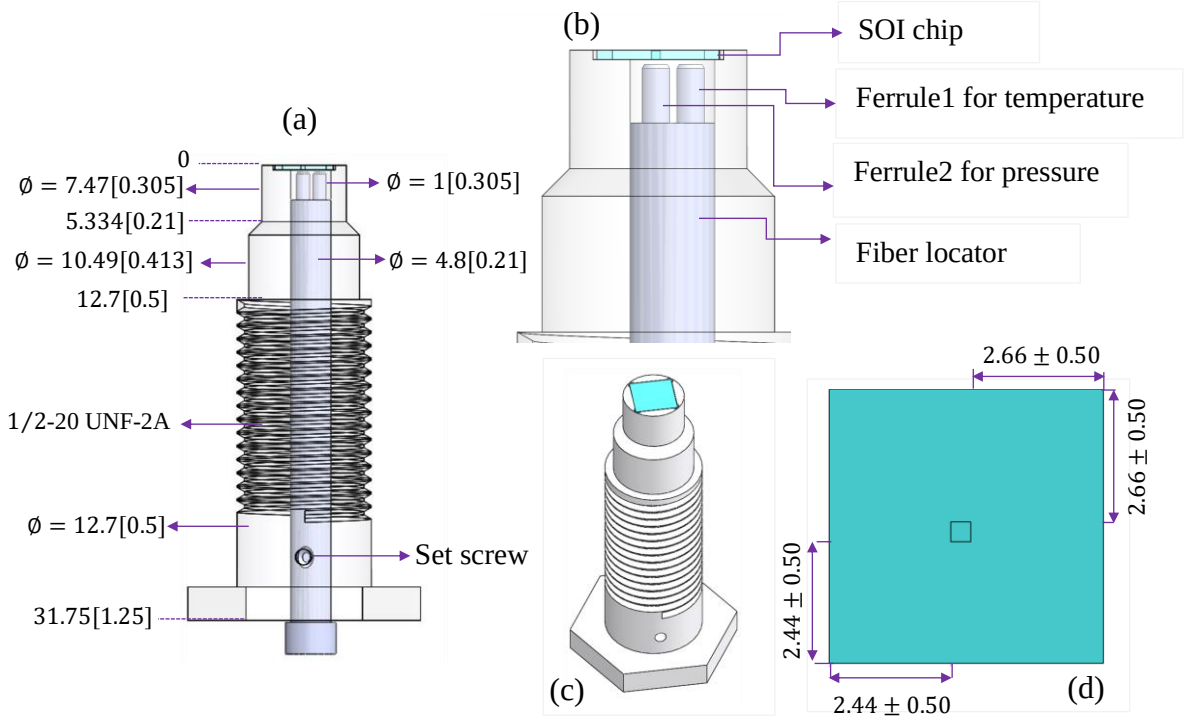

Fig. 23. The packaging assembly: (a) a transparent view with dimensions in mm [inches], (b) a detailed view of the parts, (c) a full isometric view of the packaging and (d) a detailed two-dimensional plot of the model geometry of the SOI chip.

Upon the assembly of the device (see Fig. 24), an FP cavity for sensing pressure was present between the optical fiber surface and the membrane. A second FP cavity for temperature measurements was present between the second fiber and the SOI chip's substrate.

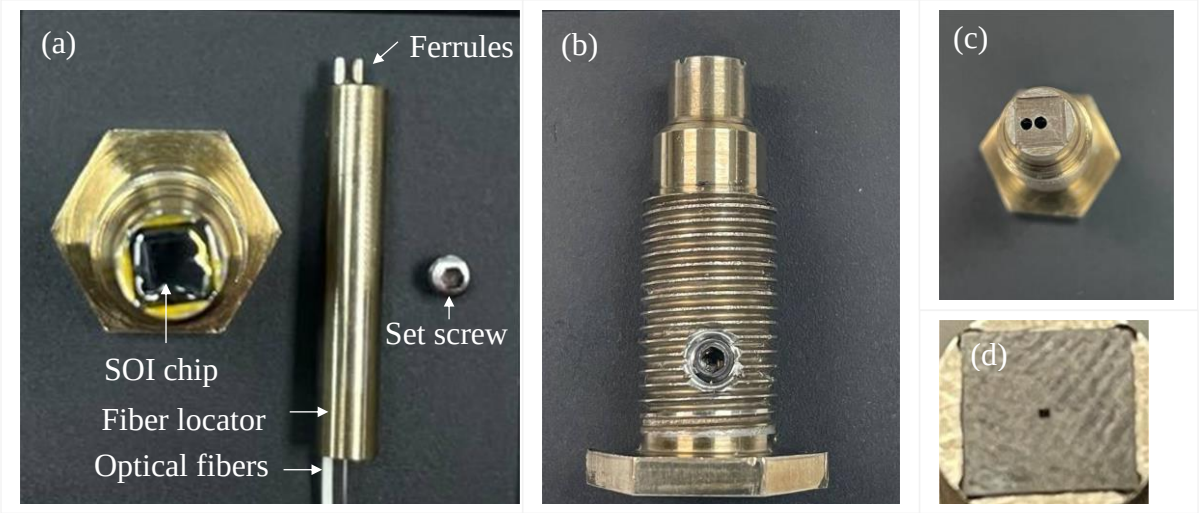

Fig. 24. The full assembly of the device: (a) side view of the fiber locator with the ferrules and optical fibers, (b) the packaged sensor, (c) a top view of the housing before placing the SOI chip and (d) the SOI chip with the 400 μm silicon membrane visible near the center.

5.4 Experimental Setup

The entire experimental setup is schematically presented within Fig. 25. The sensing system was configured based on the intensity-interrogation method [151]. Two SM Y-couplers with a 50/50 splitting ratio (Fiber Instrument Sales Inc.) were used as the main avenue for light to transmit and receive from each of the FP cavities. The Y-couplers were each connected to a voltage-controlled 850 nm laser LED (OPV314AT, TT Electronics [152]) at one of the split ends of the Y-couplers. The two LEDs were connected in parallel to a DC power supply (E3631A, Agilent) via a breadboard. The DC power supply was configured to allow a maximum supply of 1.994 V and 0.01 amps. The other split ends of the two Y-couplers were each connected to an in-house optical sensor interrogator (OSI) [153] (as explained in Chapter 4, the OSI has a built-in photodiode for measuring the intensity of the reflected light coming from the Y-couplers' single end). The single

ends were adhered to the ferrules found within the fiber locator seen in Fig. 24 (a) using epoxy (EPO-TEK 353ND) and directed to the two FP cavities, i.e., one for the pressure sensing and the other for temperature sensing). The gain and sampling rates of the photodiodes in the OSIs were optimized to achieve an optical signal with a high resolution and avoid the saturation of the signal. MATLAB (v. R2021b) was configured to retrieve the signals from the OSI, provide a live plot of the measurements and store the data for a further analysis. A manual pressure calibration apparatus with an automatic temperature control supplied by MPI MorHEAT [189] was used to manipulate the pressure applied on the developed sensing system. The designed housing was threaded to fit into the calibration machine and form a strong seal to prevent any fluid leakage. A digital pressure gauge was used on the calibration machine to display a true supplied pressure that was taken as the reference value.

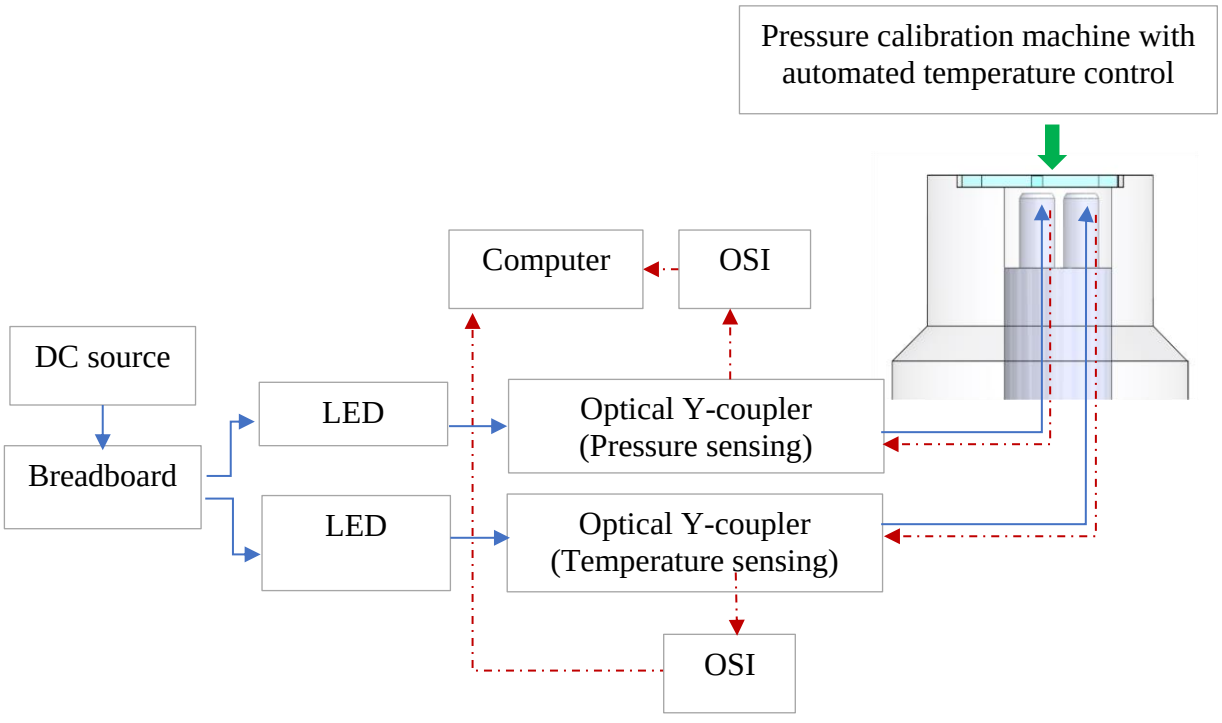

Fig. 25. A schematic of the testing setup.

5.5 Experimental Results

The developed FPI sensor underwent two experimental phases: an investigation of the temperature response and an investigation of the pressure response. For the former, the experiments were done twice. During the first test, the applied pressure was increased from atmospheric pressure to 1,000 psi in steps of 25 psi while the temperature of the heater increased in intervals of 5°C up to 120°C simultaneously. For the second test, the temperature was increased only while the gauge pressure was held at an atmospheric pressure.

Fig. 26 shows the intensity response of Optical Fiber 1, i.e., the fiber facing the SOI substrate used for temperature sensing, in the temperature range of 45–75°C (the small range was selected to produce clear plots to compare the results; the data for 25–120°C is plotted in the appendix Fig. 44). The results clearly demonstrate that pressure has no effect on the temperature-sensing mechanism in the developed FPI sensor. In other words, no cross-sensitivity was observed for the temperature sensor.

To investigate the pressure response, the pressure was increased from atmospheric pressure to 1,000 psi while the temperature was held constant at 60°C; this was repeated with 80°C, 100°C and 120°C. At each constant temperature condition, at least five trials were performed to ensure repeatability.

Fig. 27 shows the results plotted for five trials when the temperature was held at 100°C, captured from the intensity responses of Optical Fiber 2 (the pressure-sensing fiber facing the membrane). The experimental intensities of the device in response to the pressures at different constant temperatures are shown in Fig. 28. The results demonstrate that temperature has a significant effect on the pressure sensor's signal, where a clear shift in the signal occurs as temperature increases.

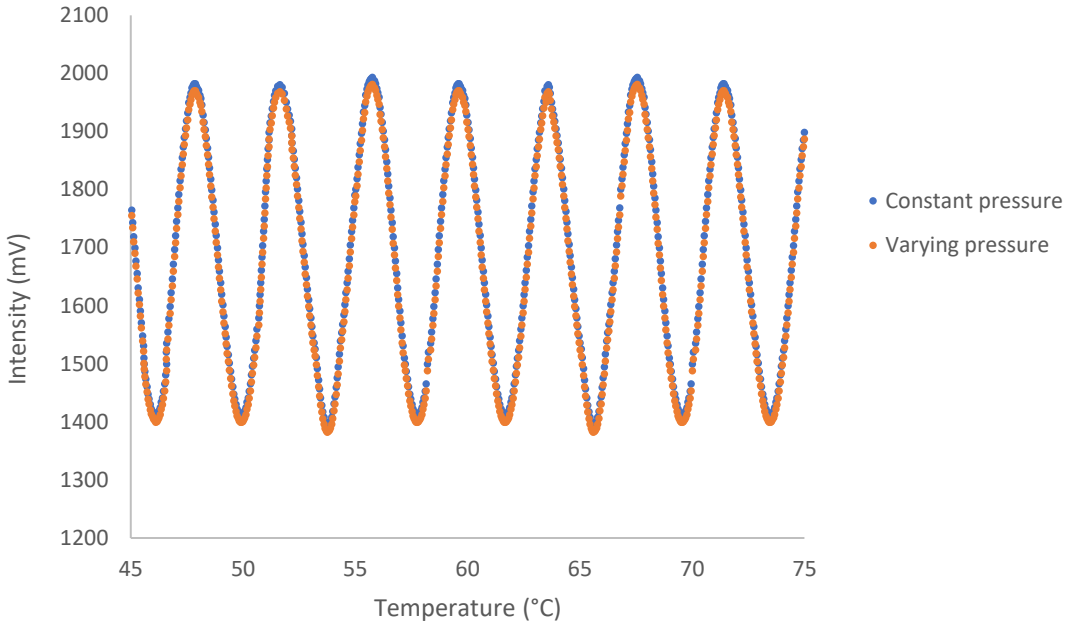

Fig. 26. The experimental intensity responses to temperature variations for Optical Fiber 1 (the fiber at the corner).

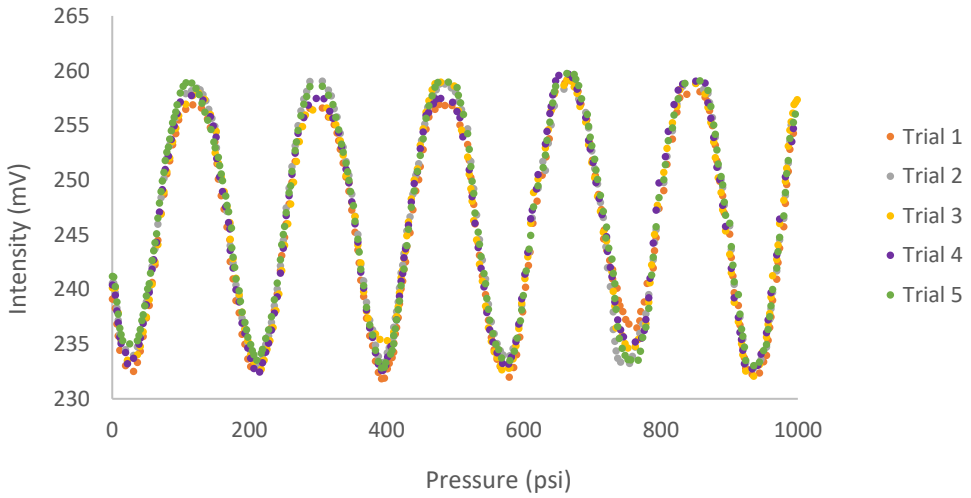

Fig. 27. The experimental intensity responses for Optical Fiber 2 (the fiber in the middle) when the pressure changed from atmospheric pressure to 1,000 psi while the temperature of the heater was stable at 100°C.

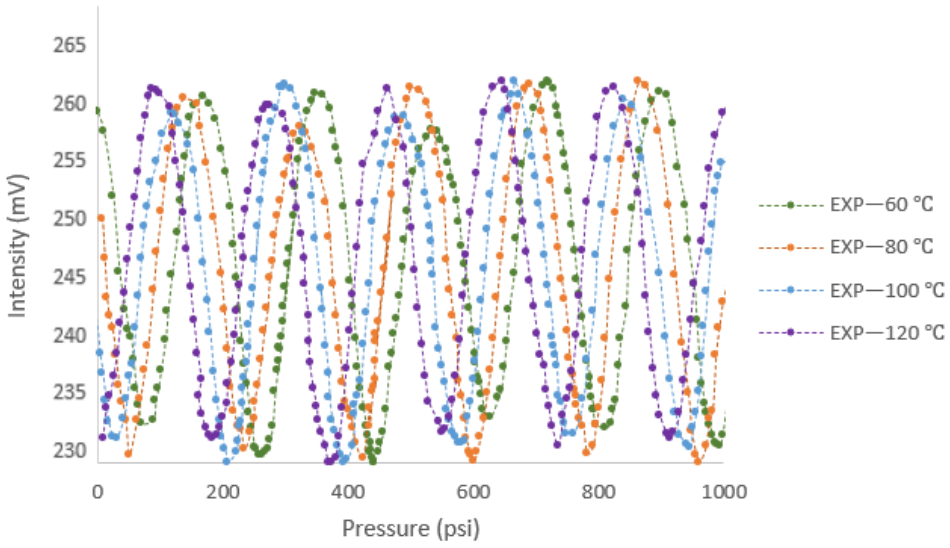

Fig. 28. The experimental intensity responses for Optical Fiber 2 (the fiber in the middle) when the pressure changed from atmospheric pressure to 1,000 psi while the temperature of the heater was stable at 60°C, 80°C, 100°C and 120°C.

To understand and compensate for the temperature effect on the pressure response, the sensing system was modeled.

5.6 Modeling

A numerical model can be an asset in studying a device's performance under different conditions and parameters [190]. The approach used in this work was a combination of analytical and numerical methods as the designed device is a multi-physics sensor combining mechanical modeling with optical theory. The mechanical component of the sensor was numerically modeled (through finite element analysis (FEA) with COMSOL), and the optical section was modeled analytically. Combining numerical and analytical models, an analytical model was developed for the designed sensor.

5.6.1 FEM

The finite element method (FEM) and COMSOL (v. 5.3a) were used to model the response of the SOI chip to pressure and temperature. The model simulated thermal expansion and membrane deflection utilizing analyses of static structural mechanics. A solid mechanics interface was utilized for the numerical simulation, and for the silicon membrane, a membrane interface was utilized. The equations for the two interfaces are discussed in the *Structural Mechanics Module User's Guide* by COMSOL Inc. [191]. The stresses were set to zero at 293 K. The solid-mechanics interface boundary conditions were determined by setting the SOI chip boundaries in regards to the x, y and z rotations and displacements. For the mesh structure, a mix of elements that were free tetrahedral and free triangular was used. Overall, 21,406 such mesh elements were used for the model; a mesh study was conducted ensuring the results were independent of the mesh size (the results for a numerical simulation with a smaller mesh with 27,526 elements were the same, which proves the simulation is mesh independent). To simulate applied pressure, a boundary load on the top boundary of the SOI chip was applied. The simulated applied pressure ranged from atmospheric pressure to 1,000 psi, while the environmental temperature was held constant at the ambient temperature (22°C); this was repeated for 60°C, 80°C, 100°C and 120°C. The simulated membrane's maximum deflection with an applied pressure of 1,000 psi is shown in Fig. 29.

Fig. 30 shows the membrane's maximum deflection in a plot as a function of the pressure for each of the simulated constant temperature conditions. It is clear that as a temperature is increased, the deflections increase. The silicon membrane at the ambient temperature was simulated to deflect 2.33 μm at 1,000 psi, and when the environmental temperature was increased to 120°C, the deflection increased to 2.71 μm.

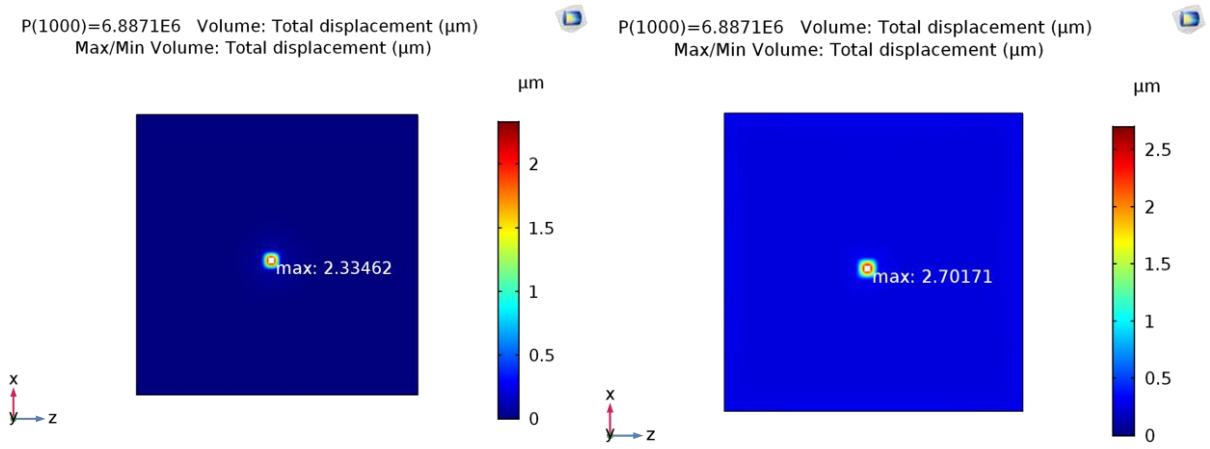

Fig. 29. The displacement of the SOI chip at a pressure equal to 1,000 psi (a) at the ambient temperature (T = 22°C) and (b) at T = 100°C (393.15 K). The maximum of displacement occurred in the center of the membrane.

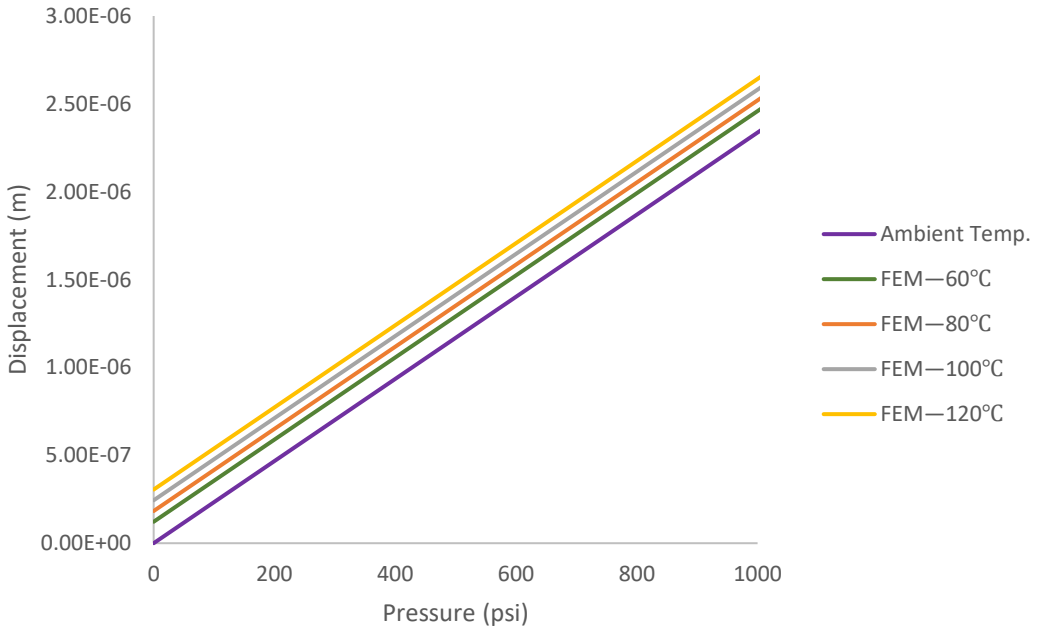

Fig. 30. A plot showing the membrane's displacement at the center point when a pressure of 0–1,000 psi was applied to the membrane at the ambient temperature.

As pointed out, to model the developed FPI pressure sensor, a combination of optics and mechanics was needed. A thin silicon membrane acts as a sensitive element, and an optical fiber acts as a signal carrier. The FEM was used to study the mechanical aspects of the sensor and the housing. To numerically analyze the optical part of the device, the membrane's deflection from the FEM simulation was used as an input and used in equations (8)–(10) to solve for the fraction of reflected light.

5.7 Modeling Results and Discussion

Fig. 31 compares the normalized experimental results for when the pressure was varied from atmospheric pressure to 1,000 psi (Fig. 27) with the normalized simulated model results. Comparing the experimental and analytical results, the sinusoidal trend was closely followed by the model, indicating a good fit. The MSE is 0.008 which is close to zero and proves the data are in good agreement. Overall, the results demonstrate the reliability of the pressure sensor at the ambient temperature and a high pressure, i.e., up to 1,000 psi.

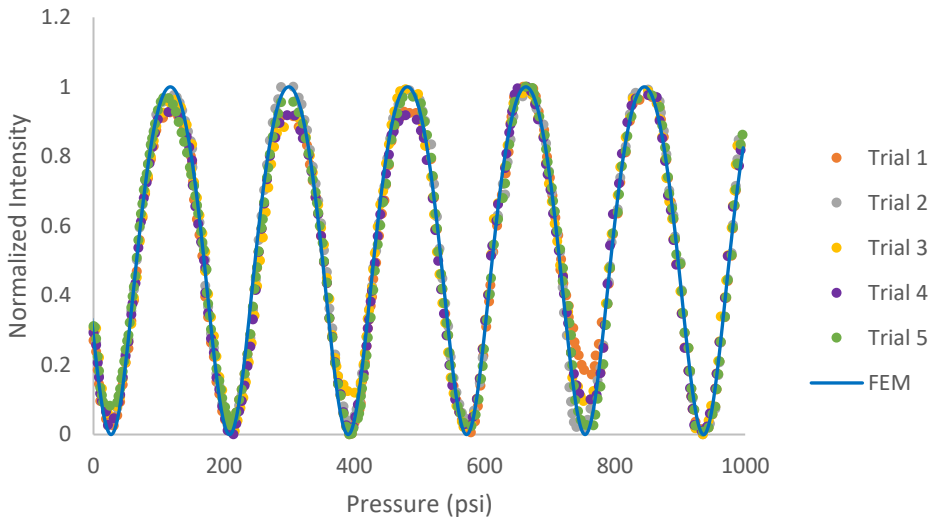

Fig. 31. The normalized membrane intensity as a pressure function while the temperature of the heater was stable at 100°C.

Fig. 32 shows the sensor's simulated response and normalized experimental response at various environmental temperatures. The results indicate a shift in the phase of the sinusoidal trend while the frequency of change with pressure remains constant. Temperature affects the material properties of the SOI chip, increasing the deflection as it increases.

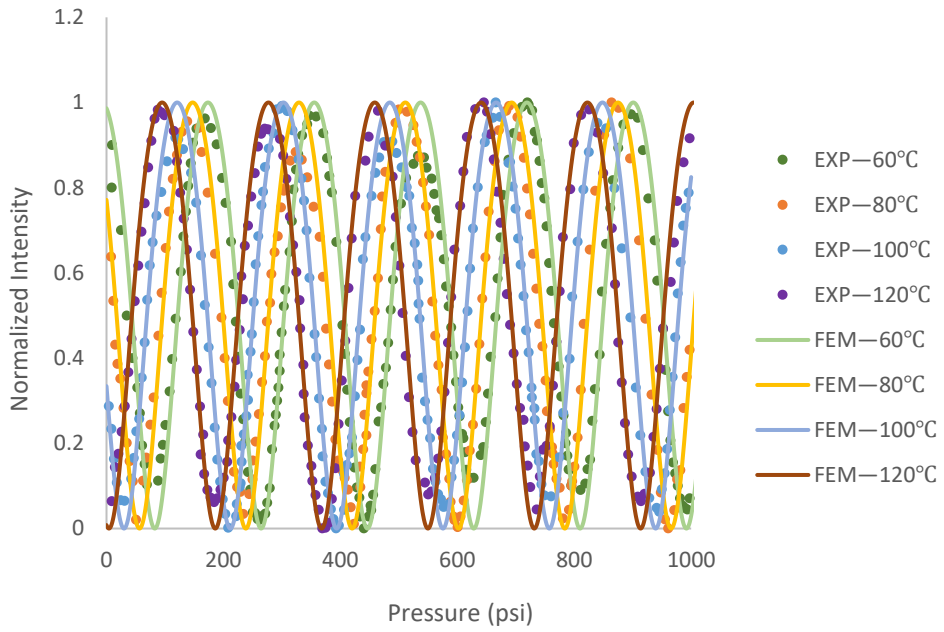

Fig. 32. The analytical analysis results for the intensity response at the die's function of pressure for the ambient–120°C temperature range.

5.8 Empirical Model for Self-Compensated Temperature Effect

To investigate the temperature effect on the sensor's performance, an empirical model needed to be developed to relate the deflection to the pressure and temperature together. There is no general expression for a deflection within a plate; the solutions for straight boundary plates are typically numerically determined for certain plate dimension ratios, load locations and boundary conditions [192]. For rectangular plates that are uniformly loaded, Roark et al. provided analytical solutions [193]. The primary equation for deflection (δ) is:

$$\delta = \frac{Pb^4}{Et^3}, \tag{18}$$

where P denotes the force's/area's distributed load, b denotes the side length of the membrane, E denotes the elastic modulus and t denotes the membrane's thickness.

For some special ratios of plate dimensions and boundary conditions for Poisson's ratio ν = 0.316, specific values for these terms were extracted from the literature and tabulated in Roark's formulas for stress and strain [193].

Using the results of the numerical simulations, the extracted coefficient for the membrane is 0.034. Therefore, the deflection of membrane is:

$$\delta = -\frac{0.0345Pb^4}{Et^3}. \tag{19}$$

The temperature rise introduced thermal stress to the structure due to a mismatch of the thermal expansion coefficient in the device's parts. Such stress altered the membrane deformation as a response to the pressures that were placed and changed the sensor's response. Furthermore, deformation arose within the device due to thermal expansion. To study the effects of temperature, a numerical simulation was done at the temperature range of the ambient temperature to 120°C.

Using the numerical method's results, the developed analytical model for the deflection of the membrane at higher temperatures was as follows:

$$\delta = -\frac{0.0345Pb^4}{Et^3} + \left(\frac{T - T_0}{T_0} * C1\right), \tag{20}$$

where T is the testing temperature, T_0 is the ambient temperature (20°C) and $C1$ is a constant equal to $C1$: 6.1×10^{-8}.

(8)–(10) and (20) were used to visualize temperature's effects on the pressure response in Fig. 33. This combination of equations allowed for a much quicker estimation of the sensor's response versus FEM simulations, and with further work, it allows for an advanced signal analysis of the developed sensing system.

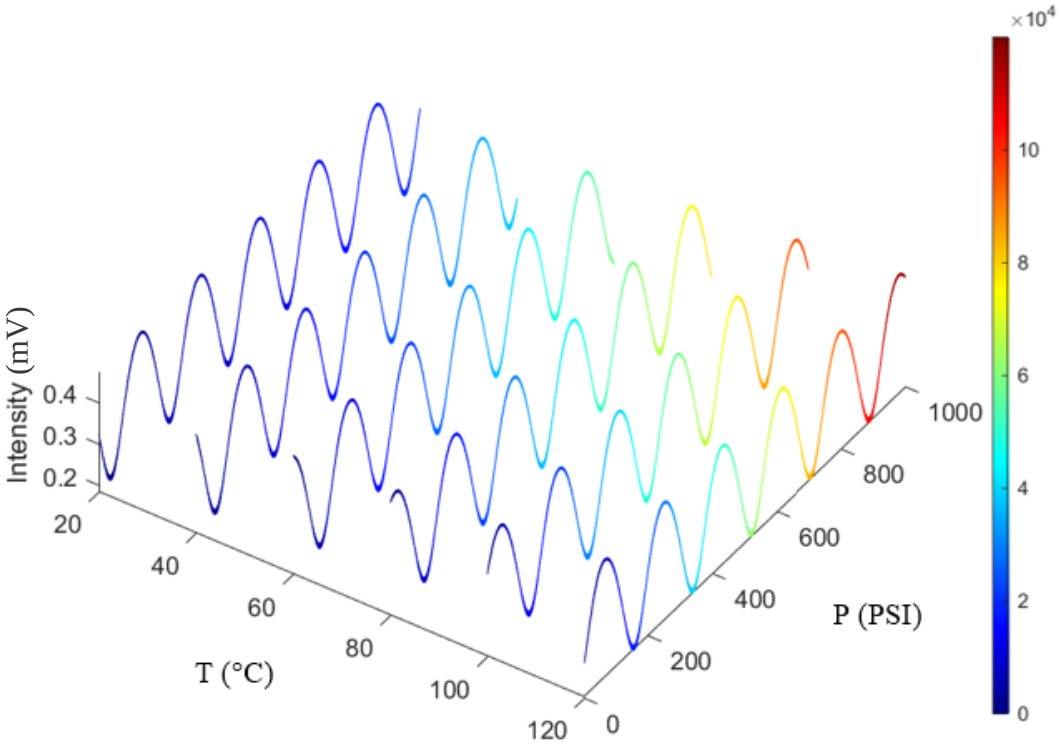

Fig. 33. The self-temperature-compensation effect on the pressure response of the sensor.

The ambiguity that exists in the intensity results limits the usage of the sensor to a linear range. The next chapter is dedicated to the demodulation of the signal.

5.9 Sensitivity and Resolution Analysis

Sensitivity is defined based on the fitting of the slope of a linear curve [128]. To investigate the sensitivity for temperature, the linear range of the experimental data plotted in Fig. 26 was extracted. The linear fitting curve is plotted in Fig. 34 showing a sensitivity of 380.31 mV/°C with a 0.99 R^2 value.

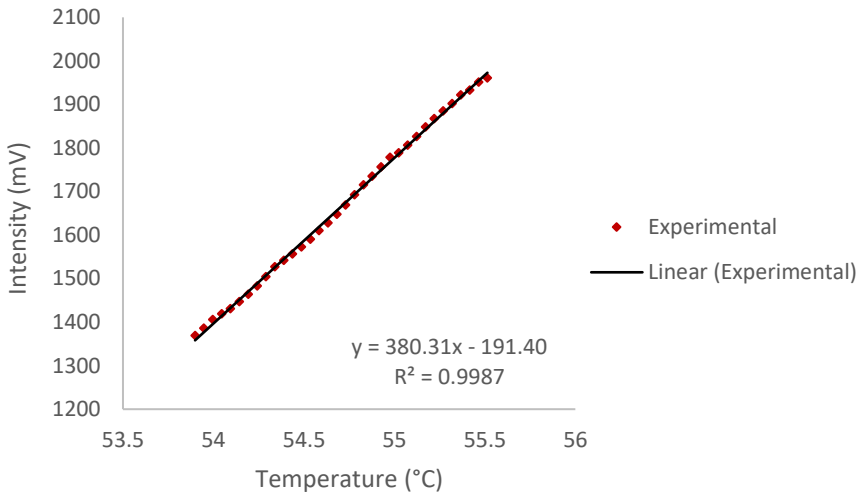

Fig. 34. Linear fitting curve of the experimental intensity response with respect to temperature variations for Optical Fiber 1.

The sensitivity of the sensor to pressure was obtained by fitting a linear curve through the average of the five trials shown in Fig. 27, plotted in Fig. 35:

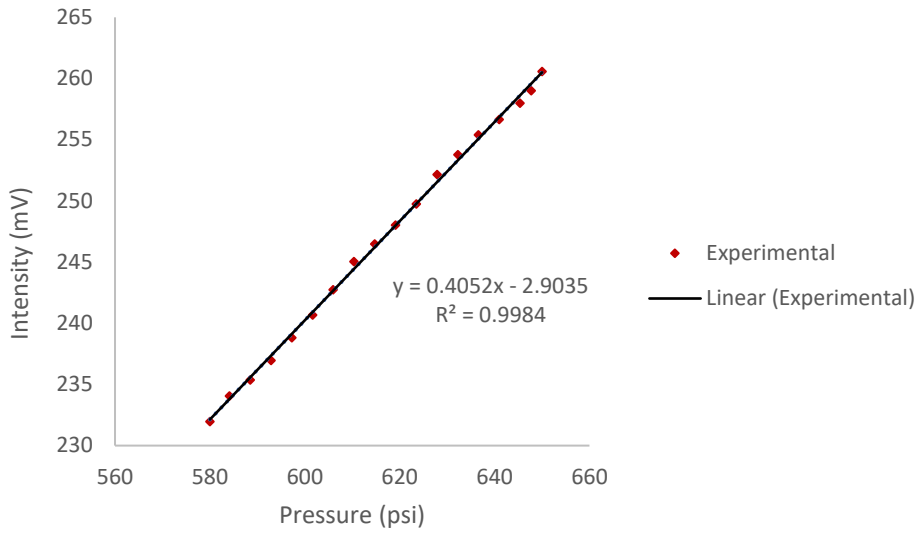

Fig. 35. Linear fitting curve of the experimental intensity response to pressure variations for Optical Fiber 2. From the slope of this curve, the sensor's sensitivity is 0.4 mV/psi, which is consistent across all ranges of temperature (refer to Fig. 28).

As discussed in the previous chapter the sensor's resolution can be determined by using the SD equation (13). Equation (14) is used to determine the experimental data's SD at a particular temperature. For example, SD is equal to 0.84 for 55°C, and 0.78 for temperature 75°C. Thus, using equation (13), resolutions for specific temperature of 55°C, and 75°C are calculated as 0.0022°C and 0.0021°C, respectively. Using the same method, SD is equal to 0.66 for a pressure of 200 psi, and 0.68 for a pressure of 500 psi. Therefore, calculated resolutions are 1.63 psi and 1.67 psi, respectively. The results are summarized in the following table.

Table 7.Sensitivity and resolution extracted from the experimental data.

Parameter	SD (mV)	Sensitivity	Resolution
Temperature 55°C	0.84	380.31 (mV/°C)	0.002 (°C)
Temperature 75°C	0.78	380.31(mV/°C)	0.002 (°C)
Pressure 200 psi	0.66	0.405 (mV/psi)	1.63 (psi)
Pressure 500 psi	0.68	0.405 (mV/psi)	1.67 (psi)

Results show that the developed sensor has high sensitivity to temperature and pressure. Since the intensity interrogation method is different with the common method used in the literature (spectral interrogating) a direct comparison of sensitivity values cannot be made.

5.10 Summary

An extrinsic FPI MEMS pressure- and temperature-sensing device was designed and fabricated. The sensing mechanism has a stainless-steel housing created so the optical fiber can be easily aligned with the membrane. The results showed that the device can sense pressure up to 1,000 psi and temperature up to 120°C. Due to the unique features of the housing, the temperature response is insensitive to pressure. To compensate for temperature's effect on the pressure response, by combining material-science and solid-mechanics principles, a predictive model for the behavior of the increased-temperature membrane was developed. By combining finite-element analysis and equations of membrane deflection with the temperature deviations and thermal expansion of material properties, an approach that is multi-variable was utilized to consider temperature's

effects on the pressure sensor. Thus, an FPI pressure sensor that can work at 120°C and at over 1,000 psi was planned and created. The sensor has 380.31 (mV/°C) temperature sensitivity and 0.405 (mV/psi) pressure sensitivity. Due to clearing components that are electronic from the sensing area, operating temperature limits occurred due to only the materials' mechanical limitations.

6 Modeling and Optical Demodulation of an Intensity-Based Fiber Optic Fabry–Pérot Interferometer Pressure Sensor

The basis of this chapter is the following paper, which is a pending submission by S. Ghaderian, A. Ghannoum and P. Nieva: "Optical Demodulation of an Intensity-Based Fiber Optic Fabry–Pérot Pressure Sensor"

6.1 Introduction

Interferometers each use a coherent light source and two separate optical paths or arms. Light is divided and inserted into each arm. A phase shift appears when an environmental factor disturbs one arm relative to the other one. At the end of one arm, FPIs consist of two reflective mirrors divided by a cavity that has a certain length [15]. As previously noted, FPIs have high perturbation sensitivities with respect to impacts on the two mirrors' OPL. When a perturbing parameter, such as pressure, is applied to such a device, the OPL changes, consequently causing a change in the optical phase of the reflected light [9]. The interrogation of an FPI implies to obtain a readout signal based on the measurand, and the measurand can be obtained by using signal processing. A phase variation can be obtained from either the intensity or the wavelength shift of the interferometric fringe [17]. Therefore, the interrogating techniques are categorized into intensity interrogation and spectral interrogation, respectively [27].

In spectral interrogation methods, a spectrometer is used to measure light spectra. When a measurand causes a change in the OPL, there is a shift in the light wavelength. By measuring the

light spectra, the shift in wavelength can be obtained. That shift is plotted versus pressure to measure the latter. This method can be used for only a limited range of pressure: 0–290 psi [110][194][195][196]. Moreover, spectrometer-based technology is extremely expensive and is often used for special-environment sensing with high-performance requirements.

In the intensity-interrogation method, through a photodetector, a photodiode turns the intensity of light that is reflected into a signal that is electrical and is electronically processed. The electrical signal is transmitted for processing, whereby demodulating information on the light is obtained to obtain the measurand. This intensity-interrogation method is simple and cost-effective compared to spectral interrogation. Yet, since light interference is periodic, ambiguity exists in measuring the parameters [39][197]. Therefore, in this method, the linear range in the signal is used to relate pressure to intensity. Consequently, using this method, a limited range of pressure is measurable [112].

For this chapter, a demodulation method was developed to remove the sensor linear range limitations of intensity-based interrogation methods. This demodulation model improves signal processing by converting all measured intensities to all values of pressure ranges. Thus, pressure measurements up to even 1,000 psi are possible. This chapter is a follow up to the research presented in Chapter 5.

6.2 Theory and Working Principle

As mentioned in previous chapters, interferometers each use a coherent light source and two separate optical paths or arms. The light is divided and inserted into each arm. A phase shift appears when an environment disturbs one arm relative to another one. $\emptyset$, the round-trip propagation phase shift for an FPI, is presented in (9) below.

$$\Delta\emptyset = \frac{2\pi nL}{\lambda},$$

where for the medium in which the cavity is located, n denotes the refractive index, L denotes the FP cavity length and λ denotes the incident light's wavelength.

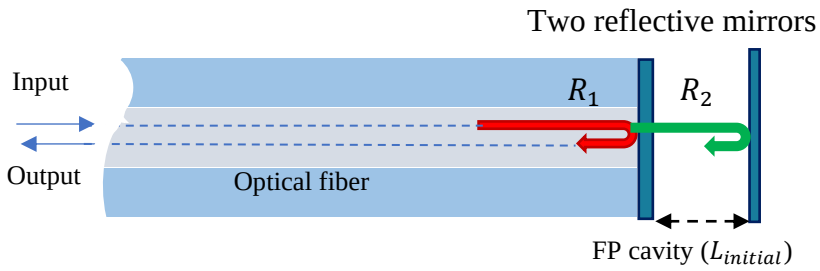

Fig. 36. A schematic of the fiber optic FPI.

Where a sensing fiber's light and a reference fiber's light are in phase once recombining occurs, the lights interfere constructively with an increase in light-intensity. In cases where the lights are out of phase, destructive interference happens, and there is a decrease in the light intensity. Recall from Chapter 4 that (8) gives the intensity change of the light:

$$\mathrm{I} = \frac{R_1 + R_2 + \sqrt{R_1 R_2}\, cos\emptyset}{1 + R_1 R_2 + 2\sqrt{R_1 R_2} cos\emptyset},$$

in which R_1 and R_2 give the reflectance from the reflecting mirrors (displayed in Fig. 36) through (10):

$$R = (\frac{n_i - n_t}{n_i + n_t})^2.$$

When the perturbance parameter is pressure, the calculated displacement ($\delta = \Delta L(\boldsymbol{P})$) obtains the cavity distance through subtracting from the initial cavity distance at an applied pressure of

zero, as (21) shows. The first cavity distance, determined using $L_{initial}$, is the length between the optical fiber's end surface and the membrane's surface.

$$L_{cavity} = L_{initial} - \delta \tag{21}$$

(8) shows that I reaches a maximum for $\cos \phi = -1$ equal to $\phi = (2m + 1)\pi$, in which the variable m is integral. Thus, the optical-spectrum intensity changes periodically along with the perturbation parameter for a certain cavity. Therefore, there is ambiguity with respect to the signal as a result of the signal being periodic, as was shown in the data on the responses.

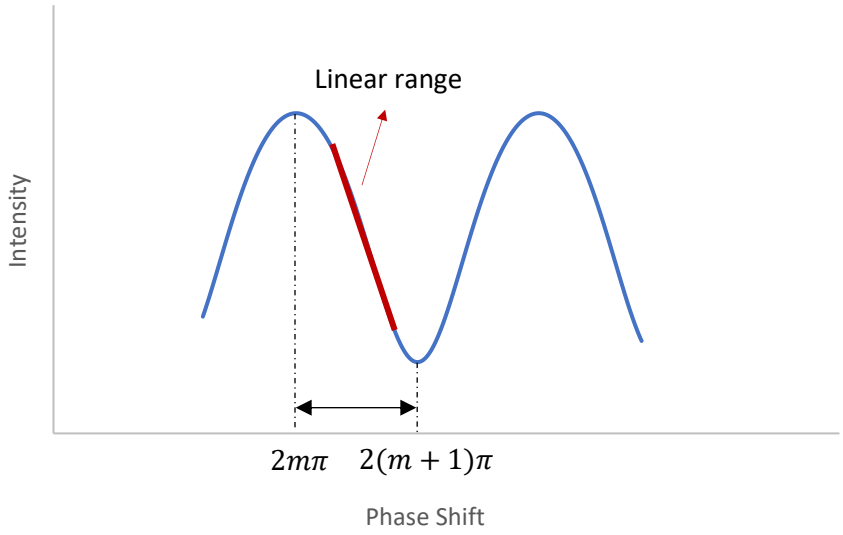

Fig. 37. A schematic diagram of the linear range.

In the linear range, the relationship between the OPL variation and the light intensity that is reflected is almost linear, as shown in Fig. 37. The intensity interrogation is quite simple, but up until now, it has been limited to this linear range.

6.3 Optical Signal Demodulation

The system pressure is obtained by considering the expression of intensity in relation to a membrane's mechanical response. By reorganizing and substituting (8) and (3), a pressure expression with respect to optical intensity and material properties may be determined. To begin, (8) is reorganized in order to obtain an expression for phase as an intensity function; see below.

$$cos\emptyset = \frac{I + IR_1R_2 - R_1 - R_2}{-2I\sqrt{R_1R_2} + 2\sqrt{R_1R_2}} \tag{22}$$

The researcher needed to obtain $\emptyset$ from the above equation. From trigonometry in math, it was known that $arc\cos\phi$ has a [-1, 1] domain as well as [0°, 180°] range, or [0, π]. This causes a limitation to Quadrant I and Quadrant II when finding solutions to expressions using the inverse cosine function [198][199]. Thus, for this range, only $\emptyset = arc(cos\emptyset)$. In other ranges, $arc\cos\phi$ could not return the values that were desired. When $\cos^{-1}\cos\phi$ is wanted in other ranges, one has to shift x in the range of $[\mathbf{0}, \pi]$. Thus, one gets [200]:

$$\emptyset = 2\mathrm{K}\pi \pm \cos^{-1}(cos\emptyset) \tag{23}$$

when K∈$\mathbb{Z}$ (K is the integer), which depends on the range of *x*. Remember that $cos(\mathbf{2}\pi - x) = cosx$, so no change was made to the original equation.

Therefore,

$$\emptyset = 2\mathrm{K}\pi \pm \cos^{-1}\left(\frac{I + IR_1R_2 - R_1 - R_2}{-2I\sqrt{R_1R_2} + 2\sqrt{R_1R_2}}\right). \tag{24}$$

Keep in mind that the definition of L relates to the etalon's cavity distance; it modulates membrane deflection. By taking (21), substituting in (23), and reorganizing for δ, a cavity-distance expression was obtained as an intensity function:

$$\delta \approx L_{initial} - \frac{\lambda}{2\pi n} \times 2\mathrm{K}\pi \pm \cos^{-1}\left(\frac{I + IR_1R_2 - R_1 - R_2}{-2I\sqrt{R_1R_2} + 2\sqrt{R_1R_2}}\right). \quad (25)$$

A membrane that is square was utilized for this study; its deflection was a pressure function that was defined using (26), which was explained in a previous chapter in (20).

$$P = \frac{(\delta - A)(Et^3)}{0.0345b^4}, \quad (26)$$

where P denotes the load that is distributed within a force/region, E denotes the elastic modulus, t denotes the membrane's thickness and b denotes the side-length of the membrane. In (26), A represents the sensor's thermal behavior by compensating for alterations in thermal expansion, material properties and residual stresses as a temperature function. Combining (25) and (26), the pressure is obtained from the intensity.

6.4 Results and Discussion

The method discussed in the previous section provides the means to calculate the initial cavity length. In this section, initial cavity length is investigated in section 6.4.1. Then, constructive and destructive interference is modeled using a mathematical analysis. Based on constructive and destructive interference, plus or minus signs had to be inserted in (25). Two examples are presented to clarify the plus minus sign and underpin the model.

6.4.1 Initial Cavity Length

The solution to the phase equation, (22), can create a specific value of K for each initial FP cavity length. The relationship between initial cavity length and K is linear, as shown in Fig. 38. Therefore, one can correctly determine the path difference by utilizing this method and can achieve a high sensitivity.

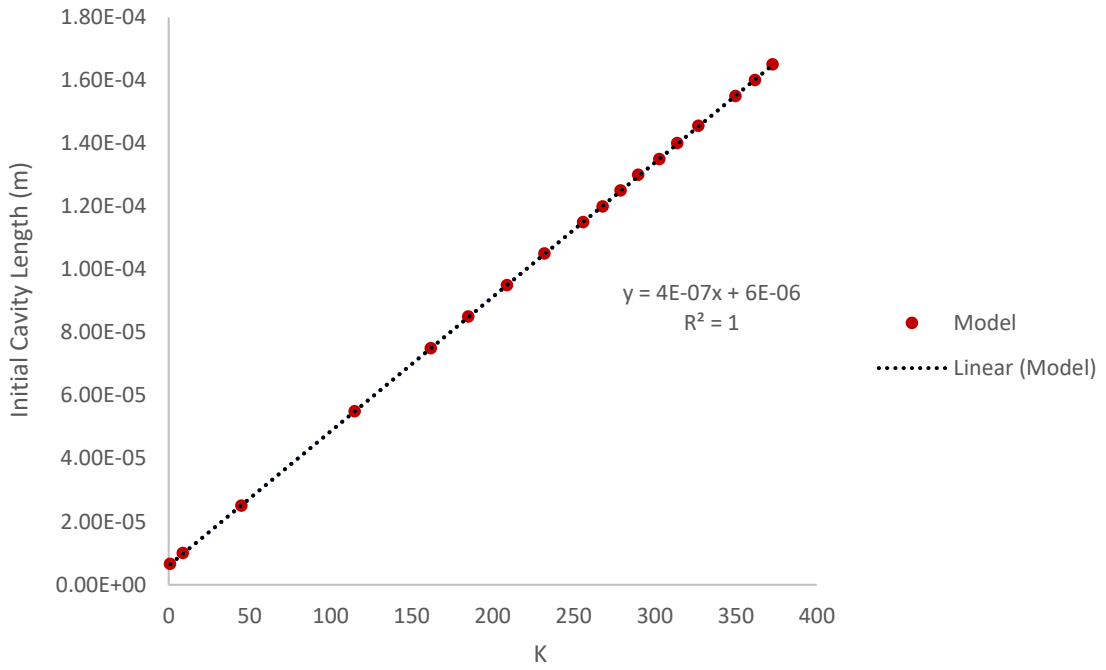

Fig. 38. The linear-fitting curve between the initial cavity length and values for K.

The values for K in the above equation relate to the initial length of the FP cavity; however, this does not predict the pressure of the whole intensity range. For the whole range of the phase, K_{new} = K-n, in which n increases by one for each induction of $\Delta\emptyset = \pi$, i.e., the transition from a transmission maximum to the following one.

6.4.2 Constructive and Destructive Interference

The initial start points in the reflected intensity spectra determined whether two light spectra interfered destructively or constructively. The plus/minus sign in (25) is related to constructive and destructive interference. The first linear range determines whether to use a plus or minus sign for each linear-range intensity value. As an example, the intensity values versus the pressure up to 1,000 psi for an FPI pressure device with an initial cavity length equal to 1.45E-04 (K = 328) are displayed in Fig. 39. The first linear range shows a decrease in the intensity values up to $\Delta\emptyset = \pi$;

therefore, for all the linear ranges with increases in the intensity values (intensity values for (2m + 1)π, i.e., for $\emptyset = \pi, 3\pi \ldots$) a plus sign had to be considered in (25), while for intensity values for linear ranges with decreases in the intensity values (intensity values for 2mπ, i.e., for $\emptyset = 0, 2\pi, 4\pi \ldots$), a minus sign had to be considered.

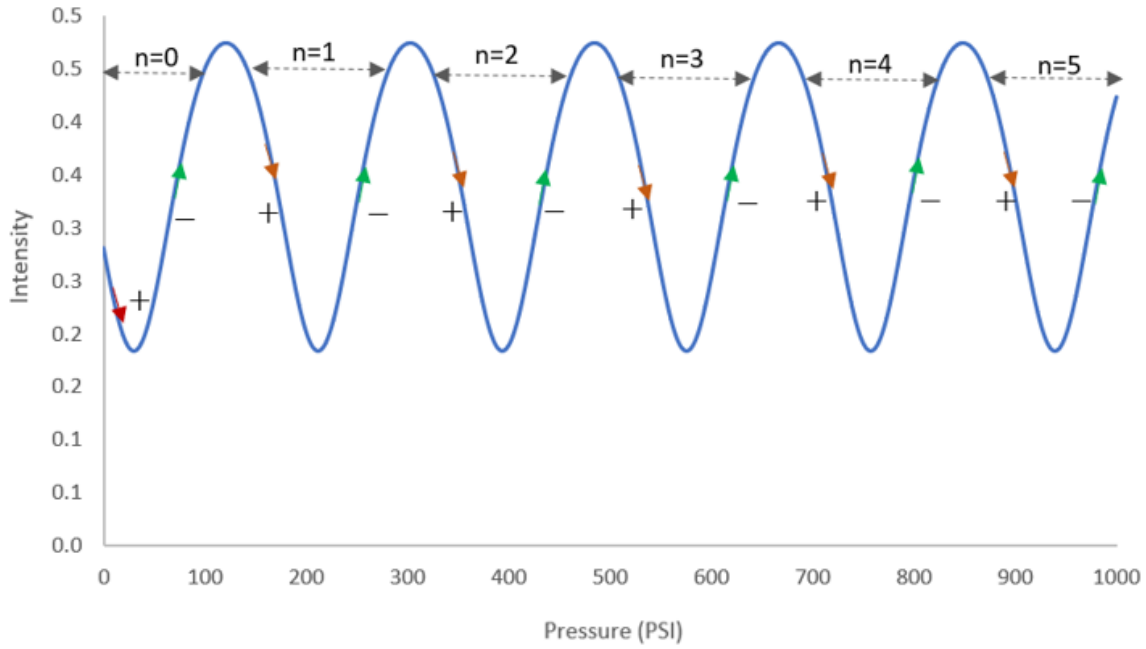

Fig. 39. The intensity spectra versus the pressure for an FPI with an initial cavity length equal to 1.45 E-04 (K = 328).

Fig. 40 shows the intensity versus the relative pressure curve for another FPI with an initial cavity length equal to 1.35 E-04 (K = 303). In this case, the first linear range shows an increase in intensity values up to $\Delta\emptyset = \pi$. Therefore, for ranges with an increase in intensity (2m + 1)π, i.e., for $\emptyset = \pi, 3\pi$, a plus sign had to be considered in (25), while for ranges with decreases in the intensity 2mπ, i.e., for $\emptyset = 0, 2\pi, 4\pi \ldots$, a minus sign had to be considered.

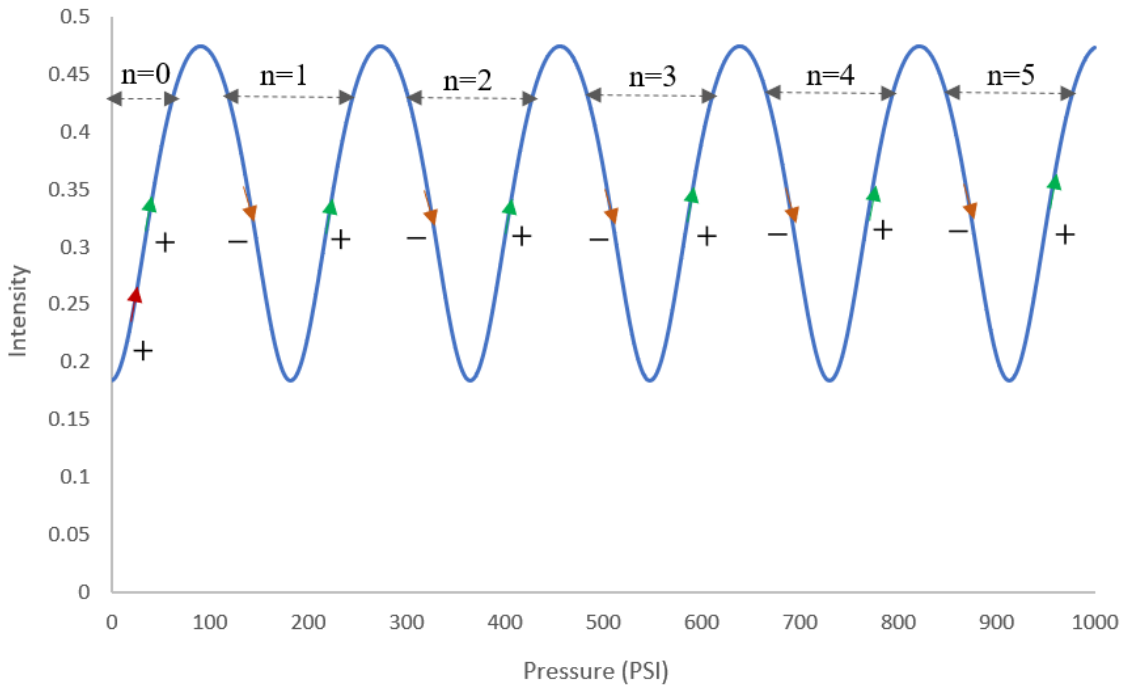

Fig. 40. The intensity spectra versus the pressure for an FPI with an initial cavity length equal to 1.35 E-04 (K = 303).

Exclusive of the plus/minus sign for each linear range, the whole intensity spectra follow the interferometer rules. Maximum intensity happens when the two legs of an interferometer are in phase and constructively interfere ($\emptyset = 0, 2\pi, 4\pi \ldots$). However, at the phase shift of an odd-number multiple of π, an integral number of a half wavelength ($\emptyset = \pi, 3\pi \ldots$), two light beams provide destructive interference and a minimum intensity. The sensitivity is as much as zero at the maximum and minimum points. Meanwhile, the region of a one-quarter wavelength shift (π /2, 3 π /2. . .) provides the highest intensity, the greatest rate of intensity variation with a phase shift.

6.5 Summary

This intensity-interrogation method is a simple and cost-effective signal interrogation method. Yet, since light interference is periodic, ambiguity exists in measuring the parameters as was shown in the data on the responses. In other words, each intensity value (on the *y* axis) corresponds to significant pressure (on the *x* axis). In this chapter, a signal demodulation method for the FFPI pressure sensor was developed so that each intensity value yields a specific pressure, even up to 1,000 psi. The model consists of a constant integer (K) that is related to the initial length of the FP cavity. There is a linear relationship between K and the initial FP cavity length. Moreover, in the model, a plus/minus sign must be chosen for each linear range. The first linear range determines whether one should insert a plus or minus sign. If one is in the first linear range, there is an increase in the intensity in all linear ranges; with an increase in the intensity, a plus sign must be considered. Therefore, by knowing the intensity values from an experiment, the corresponding pressure values can be obtained.

7 Summary and Conclusion

With rapid, affordable, low-cost and reliable devices for making parameter measurements, especially in harsh environments, on the rise [2], the intrinsic advantages of combining MEMS technology with an FFPI sensing device is increasingly of interest. MEMS technology typically enables sensors to reach a higher sensitivity and significantly faster measuring time compared with macroscopic approaches [3].

The intrinsic advantages of fiber optic sensors have made such sensors an attractive means for measurements, even in harsh environments [6]. These benefits include an electromagnetic (EM) [2] field immunity and a resistance to radio frequencies as well as a small size and weight, high accuracy, high resolution, remote controllability, and distributed sensing capabilities.

For these reasons, this thesis's overall aim was to create a custom fabricated FPI MEMS sensing device. We provided an FPI MEMS temperature sensor by using the TOE of silicon. Moreover, a multi-functional sensor for measuring temperature and pressure in harsh environments using FPI and MEMS was created.

Chapter 1 introduced the study, and Chapter 2 provided background information on the research. Chapter 3 reviewed fiber optic configurations with a focus on pressure. Literature reviews on temperature and multi-parameter sensing were presented in the next chapters.

As the optomechanical design of multi-parameter FPI temperature and pressure sensors is a highly integrated process involving many technical disciplines, including structural mechanics, thermomechanics, heat transfers, MEMS fabrication and signal processing, first, temperature sensing was investigated by developing an FPI temperature sensor. Thus, Chapter 4 was dedicated to an investigation of temperature measurement. The chapter began with an introduction and

literature review, and then the developed sensor was discussed. For this sensing device, a 25 μm thick SOI wafer—a batch-producible platform—was used.

This FPI temperature sensor was developed during this research based on the TOE of silicon. An 850 nm LED was selected as the light source because the refractive index of silicon changes substantially with temperature when observed with light near the band gap of silicon. Therefore, a relative refractive index change with temperature is much larger than other changes occurring within the silicon, including the expansion of silicon itself [8].

The sensor is housed in an epoxy-free protective packaging that increases the mechanical stability of the device. The TOC of silicon was extracted and compared with reference data. Moreover, four different couplers with different splitting ratios were used in experiments; an 80:20 SM coupler showed a higher modulation depth and sensitivity, while a 50:50 SM coupler displayed a more uniform signal with a normal distribution.

Chapter 5 then presented an integrated FPI temperature and pressure module. The proposed multi-parameter module makes use of membrane deflection for pressure sensing and the TOE for temperature measurements. The device features a unique packaging wherein an FFPI self-temperature-compensated mechanism is formed using an SOI wafer coupled with two optical fibers contained in a stainless-steel housing. A modular system was utilized for an easy alignment of a chip containing the dual sensor with the optical fibers. The features of the housing prevent pressure from affecting the temperature measurements, and limitations on operating temperature result from only the thermal mechanical properties of the sensor materials. The dual mechanism was designed so that the temperature-sensing mechanism is insensitive to pressure.

A series of experiments were conducted to test the performance of the multi-functional sensor and showed that it can withstand pressures of up to 1,000 psi and temperatures of up to 120°C; the

temperature is restricted by only the fiber optic materials. The experimental results are in good agreement with a numerical model. Moreover, an empirical model that combines solid mechanics and optical theory was used to model the FFPI self-temperature-compensated sensor and its packaging using finite-element analysis. The model integrates membrane-deflection equations, thermal expansion and temperature's effects on the material properties and accounts for the impacts of temperature on the membrane deflection of the pressure-sensing mechanism. This model can be used to design and fabricate an FPI pressure sensor capable of operating in environments with elevated temperatures and high pressures. The optical signal interrogation method, which was used for signal analyses, is cost-effective and simple compared to spectral interrogation. However, due to the periodic nature of the interference of light, ambiguity exists in measuring the parameters.

To address this ambiguity, a demodulation method was developed and presented in Chapter 6. It removes the linear-range limit of the intensity-interrogation method. In the model, a minus/plus sign is used based on the destructive and constructive interference of beams of light. This demodulation model improves signal processing by converting all measured intensities to all the values of a pressure range. Thus, pressure measurements up to even 1,000 psi are possible. By using this model, the researcher was able to obtain the initial length of the FP cavity.

For the developed sensor, sensitivities were calculated by using the slope of a linear fitting curve. The results showed a high sensitivity of 380.31 mV/°C to temperature, and 0.4 mV/psi to pressure. On the other hand, resolutions for temperature and pressure were calculated to be 0.002 °C and 1.6 psi, respectively.

A primary potential use of the developed sensor is plastic injection molding. The sensing of pressure in this application is crucial to the control of the manufacturing process; if the pressure is not sufficient, poor quality items can be created, if the pressure is too large, employees could be injured or experience an accident or equipment may experience damage [201]. Industrial piezoresistive sensors available today have significant limitations due to the temperature effect on the sensors' behaviour. As a result, manufacturers are limitedto in-process data. Such sensors infer machine barrel pressure by determining the deflection of a membrane from observable changes in the resistivity of its piezoresistive elements. Transfer fluids, such as silicone oil and mercury, allow for remote sensing and protect the membranes against direct plastic melt exposure. Historically, mercury has been utilized as the main transfer fluid for such devices, but the Canadian Environmental Protection Act, 1999, Products Containing Mercury Regulations SOR/2015-254 restricts its use. Sensing elements, e.g., films of doped polysilicon, destabilize and degrade, and although it is not until 600°C that parts made out of silicon undergo a mechanical destabilization, electrical challenges may occur at temperatures as low as 150°C [202]. The intrinsic advantages of the optical fibers and MEMS used in the proposed device make it potentially viable for use in reliable and cost-effective multi-parameter sensing in the plastic injection molding industry.

This dissertation discusses an optical system that has the capability to sense pressure and adjust with respect to temperature's impacts while it is being utilized in harsh environments; thus, this thesis increases sensors' process characterization abilities. However, since the sensing area's electronic components are removed, there are still limits with respect to operating temperatures, but they are caused only by the chosen materials' mechanical limits.

7.1 Future Work

The sensor for harsh and/or complex environments developed in this work provides a framework based on which improvements to the system can be implemented. Additional features and stability will better prepare this device for commercial viability.

7.1.1 MEMS Chip

The SOI wafer used in the device demonstrates good features for measuring pressure and temperature; however, aligning the optical fibers with the membrane for measuring pressure was challenging. The fact that the membrane is off-center because the chips are cut asymmetrically makes the alignment even more difficult. Moreover, fixing the chip on the housing with epoxy is tricky because the epoxy can slide to cover the membrane.

A proposed MEMS chip for a second prototype is displayed schematically in Fig. 41. This chip consists of a 300 μm glass substrate with a thin layer of silicon. Based on the experimental results, single-crystal silicon, having a thickness of 10 μm, provides a more-than-adequate refractive-index variation for temperature measurements.

The fabrication process will have the following steps:

1. On the 300 μm glass substrate, plasma-enhanced chemical vapor deposition will be performed to create a silicon layer with a 10 μm thickness.
2. Deep reactive ion etching (DRIE) will be used to etch a cavity in the silicon surface to create an FP cavity for pressure sensing.
3. DRIE will be used to create two holes at the bottom of the glass substrate for fibers.
4. A 25 μm SOI wafer will be anodically bonded on the top surface.

5. The handle wafer will be micromachined via the anisotropic etching of a (100) surface using a 20% KOH (potassium hydroxide) solution initially heated to a temperature of 65°C (an etching rate of approximately 30 μm/hr) and gradually reduced to a temperature of 45°C (an etching rate of approximately 10 μm/hr). The buried oxide, once exposed, will be removed using a 10% buffered-oxide etch to expose a 25 μm thick membrane window.

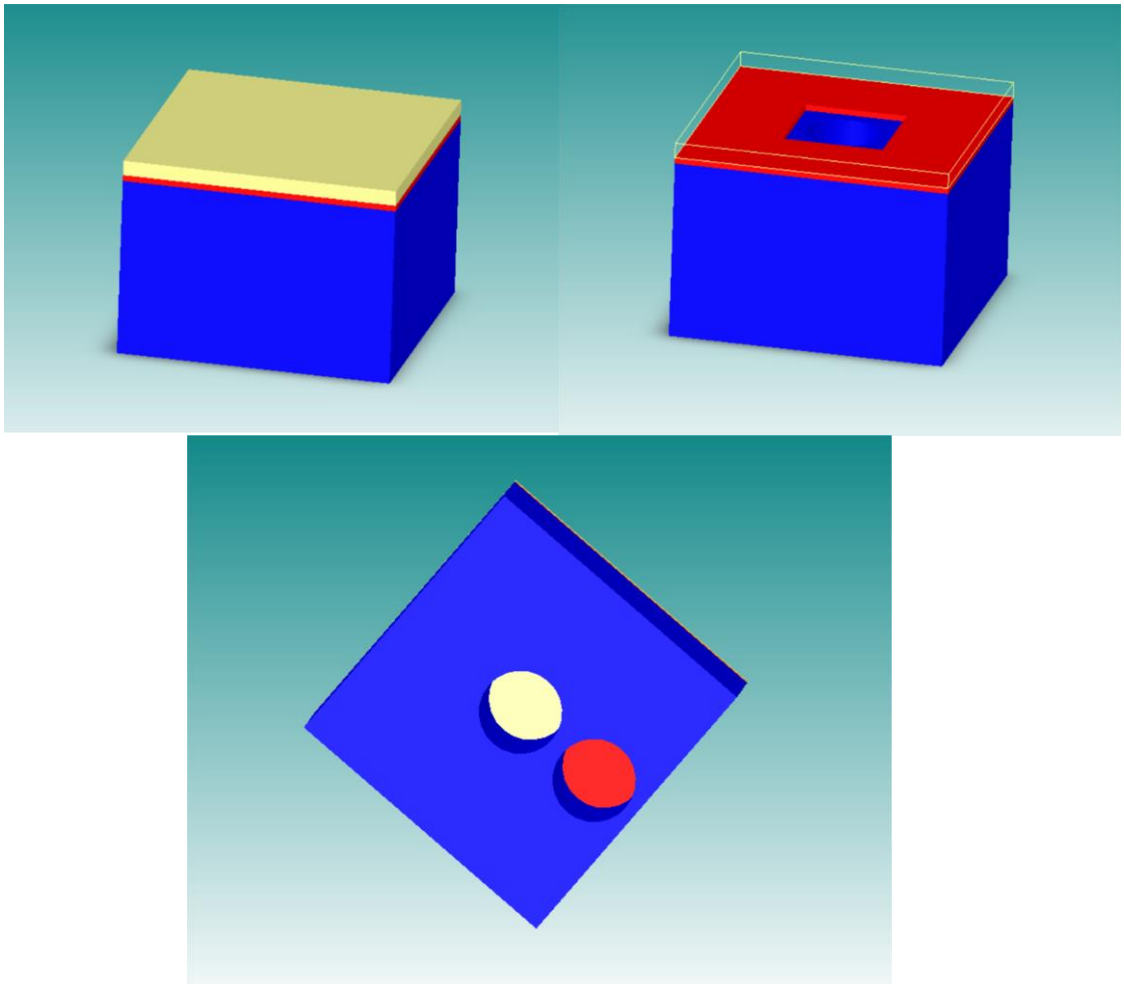

Fig. 41. The proposed MEMS chip from different perspectives, created by using CoventorWare 2.0. The blue is the glass substrate. The yellow stands for a silicon layer with a 10 μm thickness, and the red is 25 μm crystal silicon.

6. In the proposed MEMS chip, the glass substrate will support the SOI wafer properly and make the alignment with the optical fiber easy. Attaching this chip to the housing with epoxy will be easier, and the risk of covering the membrane will decrease.

7.1.2 Material for the Housing

To design a sensor to be used in elevated temperatures and at high pressures, the thermal properties of the materials that will be used will need to be considered. Stainless steel, which was used in the fabrication housing in this thesis, is a cost-effective material that has a good mechanical stability. Ceramics, such as zirconia, are stable materials with low thermal-expansion coefficients. Thus, ceramics are suitable candidates for elevated temperatures. In Fig. 42, the coefficients of thermal expansions are compared [203].

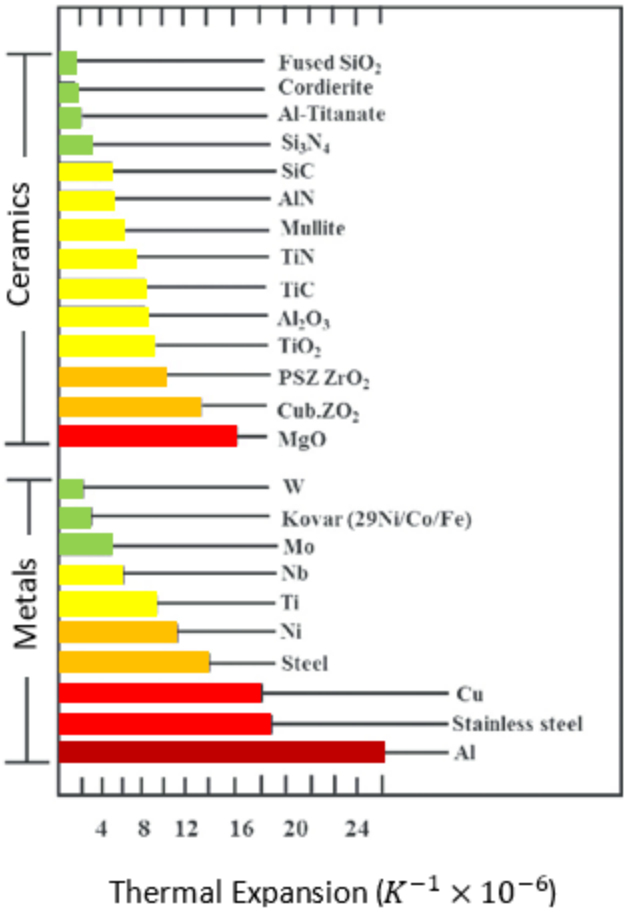

Fig. 42. A comparison of the thermal expansion coefficients of different materials (the figure was modified and redrawn from [203], page 163).

7.1.3 Signal Processing

Fiber optic sensors have the advantages of removing electrical parts from sensing points. However, the long lengths of optical fibers and couplers that must be connected to a computer might make using this sensing mechanism difficult. Using a wireless system may miniaturize the bulky optical measurement system for applications in future optical wireless-sensor networks.

Letter of Copyright Permission

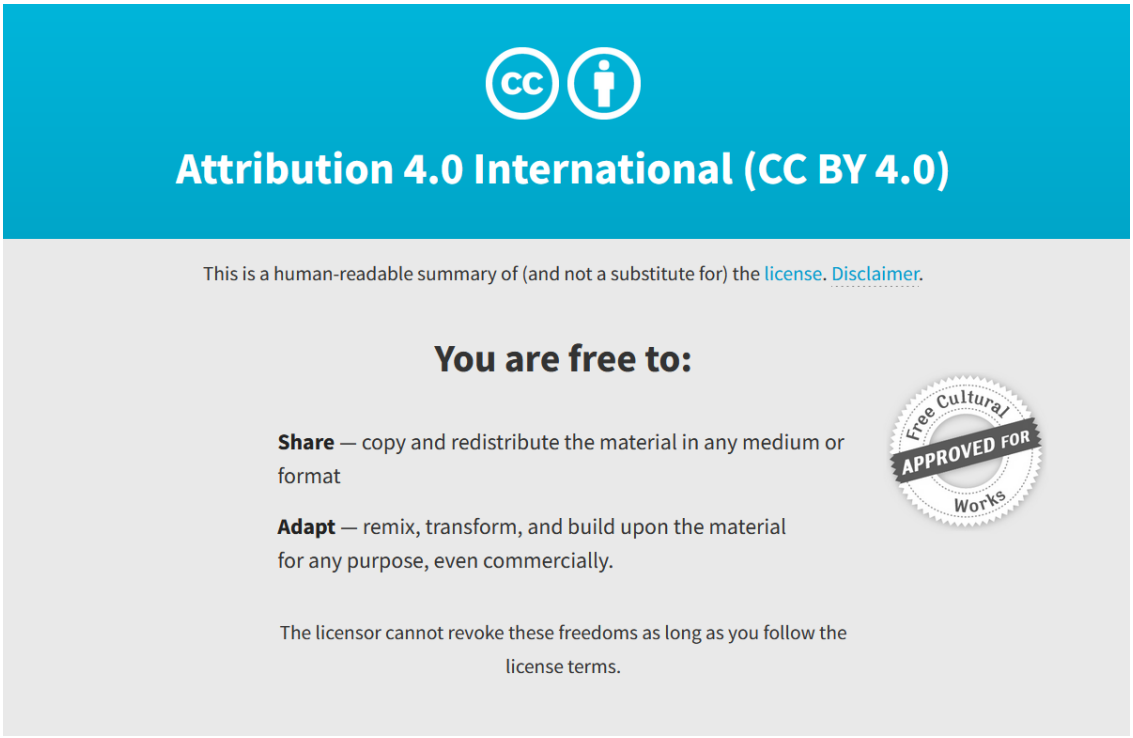

Attribution 4.0 International (CC BY 4.0)

This is a human-readable summary of (and not a substitute for) the license. Disclaimer.

You are free to:

Share — copy and redistribute the material in any medium or format

Adapt — remix, transform, and build upon the material for any purpose, even commercially.

The licensor cannot revoke these freedoms as long as you follow the license terms.

Free Cultural APPROVED FOR Works

IEEE Requesting permission to reuse content from an IEEE publication

High-Sensitivity Gas Pressure Sensor Based on Fabry–Pérot Interferometer With a Side-Opened Channel in Hollow-Core Photonic Bandgap Fiber

Author: Jian Tang
Publication: IEEE Photonics Journal
Publisher: IEEE
Date: Dec. 2015

Copyright © 2015, IEEE

Thesis / Dissertation Reuse

The IEEE does not require individuals working on a thesis to obtain a formal reuse license, however, you may print out this statement to be used as a permission grant:

Requirements to be followed when using any portion (e.g., figure, graph, table, or textual material) of an IEEE copyrighted paper in a thesis:

1) In the case of textual material (e.g., using short quotes or referring to the work within these papers) users must give full credit to the original source (author, paper, publication) followed by the IEEE copyright line © 2011 IEEE.
2) In the case of illustrations or tabular material, we require that the copyright line © [Year of original publication] IEEE appear prominently with each reprinted figure and/or table.
3) If a substantial portion of the original paper is to be used, and if you are not the senior author, also obtain the senior author's approval.

Requirements to be followed when using an entire IEEE copyrighted paper in a thesis:

1) The following IEEE copyright/ credit notice should be placed prominently in the references: © [year of original publication] IEEE. Reprinted, with permission, from [author names, paper title, IEEE publication title, and month/year of publication]
2) Only the accepted version of an IEEE copyrighted paper can be used when posting the paper or your thesis on-line.
3) In placing the thesis on the author's university website, please display the following message in a prominent place on the website: In reference to IEEE copyrighted material which is used with permission in this thesis, the IEEE does not endorse any of [university/educational entity's name goes here]'s products or services. Internal or personal use of this material is permitted. If interested in reprinting/republishing IEEE copyrighted material for advertising or promotional purposes or for creating new collective works for resale or redistribution, please go to http://www.ieee.org/publications_standards/publications/rights/rights_link.html to learn how to obtain a License from RightsLink.

References

[1] I. R. Matias and S. Ikezawa, *Smart Sensors Current Status and Future Possibilities*. springer, 2017.

[2] D. G. Senesky, K. B. Cheng, A. P. Pisano, and B. Jamshidi, "Harsh Environment Silicon Carbide Sensors for Health and Performance Monitoring of Aerospace Systems: A Review," *IEEE Sens. J.*, vol. 9, no. 11, pp. 1472–1478, 2009.

[3] C. T. Leondes, *MEMS/NEMS Handbook Techniques and Applications*. New York, 2006.

[4] V. Balakrishnan, H. P. Phan, T. Dinh, D. V. Dao, and N. T. Nguyen, "Thermal flow sensors for harsh environments," *Sensors (Switzerland)*, vol. 17, no. 9, 2017.

[5] T. M. Adams and R. A. Layton, *Introductory MEMS Fabrication and Application*. New York: springer, 2010.

[6] M. Azadeh, *Fiber Optics Engineering*. New York: springer, 2009.

[7] Y. S. Kim, N. G. Dagalakis, and Y. M. Choi, "Optical fiber Fabry-Pérot micro-displacement sensor for MEMS in-plane motion stage," *Microelectron. Eng.*, vol. 187–188, pp. 6–13, Feb. 2018.

[8] B. Sun *et al.*, "Simultaneous measurement of pressure and temperature by employing Fabry-Perot interferometer based on pendant polymer droplet," *Opt. Express*, vol. 23, no. 3, pp. 1906–1911, 2015.

[9] B. J. Thompson, *Fiber Optic Sensors*, 2nd ed. New York: CRC Press: Taylor & Francis, 2008.

[10] R. A. Wolthuis, G. L. Mitchell, E. Saaski, J. C. Hartl, and M. A. Afromowitz, “Development of Medical Pressure and Temperature Sensors Employing Optical Spectrum Modulation,” *IEEE Trans. Biomed. Eng.*, vol. 38, no. 10, pp. 974–981, 1991.

[11] E. A. Badeeva, T. I. Murashkina, D. I. Serebryakov, T. Y. Brostilova, and I. E. Slavkin, “Fiber-Optic Pressure Sensors with an Open Optical Channel for Rocket-Space and Aviation Engineering,” *2019 Int. Semin. Electron Devices Des. Prod. SED 2019 - Proc.*, Apr. 2019.

[12] L. Castañer, *Understanding MEMS principles and applications Chapter 8 Thermal devices*. Barcelona: John Wiley & Sons, Ltd, 2015.

[13] N. Sabri, S. A. Aljunid, M. S. Salim, R. B. Ahmad, and R. Kamaruddin, “Toward Optical Sensors: Review and Applications,” *J. Phys. Conf. Ser.*, vol. 423, no. 1, p. 012064, Apr. 2013.

[14] J. P. Agalloco and F. J. Carleton, “Temperature measurements,” in *Validation of Pharmaceutical Processes, Third Edition*, Third Edit., CRC Press, 2008, pp. 109–127.

[15] S. Pevec and D. Donlagić, “Multiparameter fiber-optic sensors: a review,” *Opt. Eng.*, vol. 58, no. 7, p. 072009, Mar. 2019.

[16] E. J. Brace, “Opto-Mechanical Analysis of a Harsh Environment MEMS Fabry-Perot Pressure Sensor,” University of Waterloo, 2019.

[17] A. Al-Assawi, *Fiber Optics Principle and Practices*. by Taylor & Francis Group, LLC, 2006.

[18] C. Meis, *Light and vacuum: The wave-particle nature of the light and the quantum vacuum.*

Electromagnetic theory and quantum electrodynamics beyond the standard model (second edition), 2nd ed. World Scientific Publishing Co. Pte. Ltd., 2017.

[19] C. Meis, "Basic Principles of the Electromagnetic Wave Theory," in *Light and Vacuum*, World Scientific, 2017, pp. 11–37.

[20] S.O.Kasap, *Optoelectronics and Photonics,2nd edition*. Pearson Education UK, 2013.

[21] S. Kasap, H. Ruda, and Y. Boucher, "An Illustrated Dictionary of Optoelectronics and Photonics : Important Terms and Effects," 2002.

[22] L. D. Dickson, "Characteristics of a Propagating Gaussian Beam," *Appl. Opt.*, vol. 9, no. 8, p. 1854, Aug. 1970.

[23] J. M. Liu, "Simple technique for measurements of pulsed Gaussian-beam spot sizes," *Opt. Lett.*, vol. 7, no. 5, pp. 196–198, May 1982.

[24] N. Ross Hill, "Gaussian beam migration," *Geophusics*, vol. 55, no. 11, pp. 1416–1428, Feb. 1990.

[25] D. Yu, F. Yang, B. Wen, Y. Wang, D. Huang, and C. Zhao, "Gaussian Beam Migration for Free-Surface Multiples in VSP," *Front. Earth Sci.*, vol. 10, Apr. 2022.

[26] W. B. S. Jr and E. Udd, *Field Guide to Fiber Optic Sensors*. Bellingham: Society of Photo-Optical Instrumentation Engineers (SPIE), 2015.

[27] Y.-J. Rao, Z.-L. Ran, and Y. Geong, *Fiber-Optic Fabry_Perot Sesors an introduction*. New York: CRC Press, Taylor & Francis Group, 2017.

[28] E. P. Goodwin and J. C. Wyant, *Field Guide to Interferometric Optical Testing*. Bellingham: The Society for Optical Engineering (SPIE), 2006.

[29] L. Thévenaz, *Advanced Fiber Optics Concepts And Technology*. Switzerland: EPFL Press: A Swiss academic publisher distributed by CRC Press, 2011.

[30] S. Tofighi, A. Bahrampour, N. Pishbin, and A. R. Bahrampour, "Interferometric fiber-optic sensors," *Opt. Fiber Sensors Adv. Tech. Appl.*, pp. 37–78, 2017.

[31] S. Zhang *et al.*, "Temperature characteristics of silicon core optical fiber Fabry–Perot interferometer," *Opt. Lett.*, vol. 40, no. 7, pp. 1362–1365, 2015.

[32] L. Tan, D. Hua, L. Wang, and Y. Wang, "Comparison of fringe imaging techniques using Mach-Zehnder and Fabry-Perot interferometer for molecular Doppler wind lidar," *Proc. SPIE - Int. Soc. Opt. Eng.*, vol. 8759, pp. 960–966, Jan. 2013.

[33] D. J M Vaughan MA, *The fabry-perot interferometer: History, theory, practice and applications*. New York London: CRC Press : Taylor & Francis Group, 1989.

[34] R. Chaux and J. P. Boquillon, "Diameter measurements of Fabry-Perot interference rings using CCD linear sensors," *Opt. Commun.*, vol. 30, no. 2, pp. 239–244, Aug. 1979.

[35] J. Schilling, K. Sengupta, S. Goennenwein, A. R. Bausch, and E. Sackmann, "Absolute interfacial distance measurements by dual-wavelength reflection interference contrast microscopy," *Phys. Rev. E*, vol. 69, no. 2, Feb. 2004.

[36] T. Yoshino, T. Ose, K. Kurosawa, and K. Itoh, "Fiber-Optic Fabry–Perot Interferometer and Its Sensor Applications," *IEEE Trans. Microw. Theory Tech.*, vol. 30, no. 10, pp. 1612–1621, 1982.

[37] H. F. Taylor, "Principles and applications of fiber-optic Fabry-Perot sensors," in *Conference on Lasers and Electro-Optics Europe - Technical Digest*, 1998, p. 312.

[38] C. R. C. P. Llc, *OPTO-MECHATRONIC SYSTEMS HANDBOOK*. 2003.

[39] Z. Mo, W. Xu, and N. Broderick, “A Fabry-Perot optical fiber force sensor based on intensity modulation for needle tip force sensing,” *ICARA 2015 - Proc. 2015 6th Int. Conf. Autom. Robot. Appl.*, pp. 376–380, Apr. 2015.

[40] A. Mendez, *Specialty Optical Fibers Handbook, 1st Edition*. 2007.

[41] W. Hartmann *et al.*, “Broadband Spectrometer with Single-Photon Sensitivity Exploiting Tailored Disorder,” *Nano Lett.*, vol. 20, no. 4, pp. 2625–2631, Apr. 2020.

[42] E. Vater *et al.*, “Tunable light source for narrowband laser excitation: Application to Raman spectroscopy,” *Laser Phys. Lett.*, vol. 6, no. 9, pp. 639–643, Sep. 2009.

[43] J. Podlecki, M. Nishioka, H. Toshiyoshi, Y. Arakawa, and H. Fujita, “Tunable Vertical Cavity Laser and Photodetector for Free Space Interconnection,” vol. 51, no. 8, 1999.

[44] R. Kashyap, “Principles of Optical Fiber Grating Sensors,” in *Fiber Bragg Gratings*, Elsevier, 2010, pp. 441–502.

[45] J. Goicoechea, M. Hernáez, C. R. Zamarreño, and F. J. Arregui, “Coatings for Optical Fiber Sensors,” in *Comprehensive Materials Processing*, vol. 13, Elsevier Ltd, 2014, pp. 103–119.

[46] M. Naci Inci, S. R. Kidd, J. S. Barton, and J. D. C. Jones, “Fabrication of single-mode fibre optic Fabry-Perot interferometers using fusion spliced titanium dioxide optical coatings,” *Meas. Sci. Technol.*, vol. 3, no. 7, p. 678, Jul. 1992.

[47] *Optical Fiber Fusion Splicing*. Springer-Verlag, 2005.

[48] Y. Liu, B. Li, X. Song, D. Yang, and Y. Wang, “FPI-based fibre-optic sensor fabricated by

excimer laser micromachining and fusion splicing HCF for multi-parameter measurements," *https://doi.org/10.1080/09500340.2020.1842927*, vol. 67, no. 15, pp. 1267–1276, Sep. 2020.

[49] D. W. Duan *et al.*, "In-line all-fibre Fabry-Pérot interferometer high temperature sensor formed by large lateral offset splicing," *Electron. Lett.*, vol. 47, no. 6, pp. 401–403, Mar. 2011.

[50] B. J. Peng, Y. Zhao, Y. Zhao, and J. Yang, "Tilt sensor with FBG technology and matched FBG demodulating method," *IEEE Sens. J.*, vol. 6, no. 1, pp. 63–66, Feb. 2006.

[51] S. Pachnicke, *Fiber-Optic Transmission Networks Efficient Design and Dynamic Operation*. Berlin, 2012.

[52] A. Wang, M. S. Miller, D. Sun, K. A. Murphy, and R. O. Claus, "Advances in the extrinsic Fabry-Perot interferometric optical fiber sensors," *Fiber Opt. Smart Struct. Ski. V*, vol. 1798, pp. 32–41, Mar. 1993.

[53] H. F. Taylor, "Fiber Optic Sensors Based upon the Fabry–Perot Interferometer," *Fiber Opt. Sensors*, pp. 35–64, Dec. 2017.

[54] Y. W. Huang, J. Tao, and X. G. Huang, "Research progress on F-P interference-based fiber-optic sensors," *Sensors (Switzerland)*, vol. 16, no. 9, 2016.

[55] P. Chen, Y. Dai, D. Zhang, X. Wen, and M. Yang, "Cascaded-cavity fabry-perot interferometric gas pressure sensor based on vernier effect," *Sensors*, vol. 18, no. 11, Nov. 2018.

[56] X. Yang, Y. Li, S. Zhang, S. Wang, and S. Wu, "Comparison of Fiber-Based Gas Pressure

Sensors Using Hollow-Core Photonic Crystal Fibers," *IEEE Photonics J.*, vol. 13, no. 2, 2021.

[57] Z. L. Ran, Y. J. Rao, H. Y. Deng, and X. Liao, "Miniature in-line photonic crystal fiber etalon fabricated by 157 nm laser micromachining," *Opt. Lett.*, vol. 32, no. 21, p. 3071, Nov. 2007.

[58] Z. Ran *et al.*, "Miniature fiber-optic tip high pressure sensors micromachined by 157 nm laser," *IEEE Sens. J.*, vol. 11, no. 5, pp. 1103–1106, 2011.

[59] M. jie Yin, B. Gu, Q. F. An, C. Yang, Y. L. Guan, and K. T. Yong, "Recent development of fiber-optic chemical sensors and biosensors: Mechanisms, materials, micro/nano-fabrications and applications," *Coordination Chemistry Reviews*, vol. 376. Elsevier B.V., pp. 348–392, 01-Dec-2018.

[60] E. Cibula and D. Donlagic, "Low-loss semi-reflective in-fiber mirrors," *Opt. Express*, vol. 18, no. 11, p. 12017, May 2010.

[61] T. Wieduwilt, J. Dellith, F. Talkenberg, H. Bartelt, and M. A. Schmidt, "Reflectivity enhanced refractive index sensor based on a fiber-integrated Fabry-Perot microresonator," *Opt. Express*, vol. 22, no. 21, p. 25333, Oct. 2014.

[62] S. Pevec and D. Donlagic, "Miniature fiber-optic sensor for simultaneous measurement of pressure and refractive index," *Opt. Lett.*, vol. 39, no. 21, p. 6221, Nov. 2014.

[63] W. Zhang, W. Zhuang, M. Dong, L. Zhu, and F. Meng, "Dual-Parameter Optical Fiber Sensor for Temperature and Pressure Discrimination Featuring Cascaded Tapered-FBG and Ball-EFPI," *IEEE Sens. J.*, vol. 19, no. 14, pp. 5645–5652, Jul. 2019.

[64] W. ping Chen and D. ning Wang, “Highly Sensitive Pressure Measurement based on Multimode Fiber Tip Fabry-Perot Cavity,” *Int. Conf. Photonics, Opt. Laser Technol.*, vol. 2, pp. 147–151, Feb. 2017.

[65] J. P. Dakin, W. Ecke, K. Schroeder, and M. Reuter, “Optical fiber sensors using hollow glass spheres and CCD spectrometer interrogator,” *Opt. Lasers Eng.*, vol. 47, no. 10, pp. 1034–1038, Oct. 2009.

[66] K. Chen, X. Zhou, B. Yang, W. Peng, and Q. Yu, “A hybrid fiber-optic sensing system for down-hole pressure and distributed temperature measurements,” *Opt. Laser Technol.*, vol. 73, pp. 82–87, Apr. 2015.

[67] M. Luo *et al.*, “All-fiber phase shifter based on hollow fiber interferometer integrated with Au nanorods,” *Sensors Actuators, A Phys.*, vol. 301, p. 111750, Jan. 2020.

[68] J. Xu, X. Wang, K. L. Cooper, G. R. Pickrell, and A. Wang, “Miniature temperature-insensitive Fabry - Pérot fiber-optic pressure sensor,” *IEEE Photonics Technol. Lett.*, vol. 18, no. 10, pp. 1134–1136, May 2006.

[69] H. Liang *et al.*, “Diaphragm-free fiber-optic fabry-perot interferometric gas pressure sensor for high temperature application,” *Sensors (Switzerland)*, vol. 18, no. 4, Apr. 2018.

[70] R. Fan *et al.*, “Practical research on photonic crystal fiber micro-strain sensor,” *Opt. Fiber Technol.*, vol. 52, p. 101959, Nov. 2019.

[71] Y. J. Rao, T. Zhu, X. C. Yang, and D. W. Duan, “In-line fiber-optic etalon formed by hollow-core photonic crystal fiber,” *Opt. Lett.*, vol. 32, no. 18, p. 2662, Sep. 2007.

[72] W. Ding and Y. Jiang, “All-solid photonic band gap fiber based distributed fiber optic

pressure sensor," *Opt. Express*, vol. 20, no. 13, p. 14054, Jun. 2012.

[73] C. Wu, H. Y. Fu, K. K. Qureshi, B.-O. Guan, and H. Y. Tam, "High-pressure and high-temperature characteristics of a Fabry–Perot interferometer based on photonic crystal fiber," *Opt. Lett.*, vol. 36, no. 3, p. 412, 2011.

[74] L. Zhang *et al.*, "Simultaneous Measurements of Temperature and Pressure With a Dual-Cavity Fabry-Perot Sensor," *IEEE Photonics Technol. Lett.*, vol. 31, no. 1, pp. 106–109, 2019.

[75] L. Zhang *et al.*, "A diaphragm-free fiber Fabry-Perot gas pressure sensor," *Rev. Sci. Instrum.*, vol. 90, no. 2, p. 025005, Feb. 2019.

[76] B. Xu, C. Wang, D. N. Wang, Y. Liu, and Y. Li, "Fiber-tip gas pressure sensor based on dual capillaries," *Opt. Express*, vol. 23, no. 18, p. 23484, Sep. 2015.

[77] B. Xu, Y. Liu, D. Wang, D. Jia, and C. Jiang, "Optical fiber fabry-pérot interferometer based on an air cavity for gas pressure sensing," *IEEE Photonics J.*, vol. 9, no. 2, Apr. 2017.

[78] Z. Zhang *et al.*, "Diaphragm-free gas-pressure sensor probe based on hollow-core photonic bandgap fiber," *Opt. Lett.*, vol. 43, no. 13, p. 3017, Jul. 2018.

[79] J. Tang *et al.*, "High-Sensitivity Gas Pressure Sensor Based on Fabry-Pérot Interferometer With a Side-Opened Channel in Hollow-Core Photonic Bandgap Fiber," *IEEE Photonics J.*, vol. 7, no. 6, 2015.

[80] B. Lee, "Review of the present status of optical fiber sensors," *Opt. Fiber Technol.*, vol. 9, no. 2, pp. 57–79, Apr. 2003.

[81] X. Wang, B. Li, O. L. Russo, H. T. Roman, K. K. Chin, and K. R. Farmer, "Diaphragm

design guidelines and an optical pressure sensor based on MEMS technique," *Microelectronics J.*, vol. 37, no. 1, pp. 50–56, Jan. 2006.

[82] H. Li, H. Deng, G. Zheng, M. Shan, Z. Zhong, and B. Liu, "Reviews on Corrugated Diaphragms in Miniature Fiber-Optic Pressure Sensors," *Appl. Sci.*, vol. 9, no. 11, p. 2241, May 2019.

[83] J. Ma, W. Jin, H. L. Ho, and J. Y. Dai, "High-sensitivity fiber-tip pressure sensor with graphene diaphragm," *Opt. Lett.*, vol. 37, no. 13, p. 2493, Jul. 2012.

[84] X. Wang, B. Li, O. L. Russo, H. T. Roman, K. K. Chin, and K. R. Farmer, "Diaphragm design guidelines and an optical pressure sensor based on MEMS technique," *Microelectronics J.*, vol. 37, no. 1, pp. 50–56, 2006.

[85] Y. Ge, J. Zhou, and X. Mao, "Miniature fiber pressure sensor based on fiber etching," *Optik (Stuttg).*, vol. 124, no. 1, pp. 4–7, Jan. 2013.

[86] S. Pevec and D. Donlagic, "Miniature all-fiber Fabry-Perot sensor for simultaneous measurement of pressure and temperature," *Appl. Opt.*, vol. 51, no. 19, pp. 4536–4541, Jul. 2012.

[87] E. Cibula, S. Pevec, B. Lenardic, E. Pinet, and D. Donlagic, "Miniature all-glass robust pressure sensor," *Opt. Express*, vol. 17, no. 7, p. 5098, Mar. 2009.

[88] Y. Zhu and A. Wang, "Miniature Fiber-Optic Pressure Sensor," *IEEE Photonics Technol. Lett.*, vol. 17, no. 2, pp. 447–449, 2005.

[89] B. A. F. Puygranier and P. Dawson, "Chemical etching of optical fibre tips - Experiment and model," *Ultramicroscopy*, vol. 85, no. 4, pp. 235–248, Dec. 2000.

[90] X. Wang, J. Xu, Y. Zhu, K. L. Cooper, and A. Wang, “All-fused-silica miniature optical fiber tip pressure sensor,” *Opt. Lett.*, vol. 31, no. 7, p. 885, Apr. 2006.

[91] K. Bremer, E. Lewis, B. Moss, G. Leen, S. Lochmann, and I. Mueller, “Fabrication of a high temperature-resistance optical fibre micro pressure sensor,” in *2009 6th International Multi-Conference on Systems, Signals and Devices, SSD 2009*, 2009.

[92] W. Wang and F. Li, “Large-range liquid level sensor based on an optical fibre extrinsic Fabry-Perot interferometer,” *Opt. Lasers Eng.*, vol. 52, no. 1, pp. 201–205, Jan. 2014.

[93] M. K. Mishra, V. Dubey, P. M. Mishra, and I. Khan, “MEMS Technology: A Review,” *J. Eng. Res. Reports*, vol. 4, no. 1, pp. 1–24, Feb. 2019.

[94] J. H. Bruning, “Optical lithography: 40 years and holding,” *Opt. Microlithogr. XX*, vol. 6520, p. 652004, Mar. 2007.

[95] M. Hoffmann and E. Voges, “Bulk silicon micromachining for MEMS in optical communication systems,” *J. Micromechanics Microengineering*, vol. 12, no. 4, p. 349, Jun. 2002.

[96] D. Hays *et al.*, “A hybrid MEMS fiber optic tunable fabryperot filter,” *J. Microelectromechanical Syst.*, vol. 19, no. 2, pp. 419–429, Apr. 2010.

[97] X. Qi *et al.*, “Fiber Optic Fabry-Perot Pressure Sensor With Embedded MEMS Micro-Cavity for Ultra-High Pressure Detection,” *J. Light. Technol.*, vol. 37, no. 11, 2019.

[98] W. Ma, Y. Jiang, J. Hu, L. Jiang, and T. Zhang, “Microelectromechanical system-based, high-finesse, optical fiber Fabry–Perot interferometric pressure sensors,” *Sensors Actuators, A Phys.*, vol. 302, p. 111795, Feb. 2020.

[99] M. Li, M. Wang, and H. Li, "Optical MEMS pressure sensor based on Fabry-Perot interferometry," *Opt. Express*, vol. 14, no. 4, p. 1497, Feb. 2006.

[100] Y. Ge, M. Wang, X. Chen, and H. Rong, "An optical MEMS pressure sensor based on a phase demodulation method," *Sensors Actuators, A Phys.*, vol. 143, no. 2, pp. 224–229, May 2008.

[101] P. Jia *et al.*, "Batch-producible MEMS fiber-optic Fabry–Perot pressure sensor for high-temperature application," *Appl. Opt.*, vol. 57, no. 23, p. 6687, Aug. 2018.

[102] Z. Wang *et al.*, "Sapphire Fabry–Perot interferometer for high-temperature pressure sensing," *Appl. Opt.*, vol. 59, no. 17, p. 5189, Jun. 2020.

[103] E. Brace□, S. Ghaderian□, A. Ghannoum□, and P. Nieva, "Impact of support material deformation in MEMS bulk micromachined diaphragm pressure sensors," *J. Micromechanics Microengineering J. Micromech. Microeng*, vol. 31, p. 8, 2021.

[104] Y. Ge, K. Cai, T. Wang, and J. Zhang, "MEMS pressure sensor based on optical Fabry-Perot interference," *Optik (Stuttg).*, vol. 165, pp. 35–40, 2018.

[105] G. C. Hill *et al.*, "SU-8 MEMS Fabry-Perot pressure sensor," *Sensors Actuators, A Phys.*, vol. 138, no. 1, pp. 52–62, Jul. 2007.

[106] J. Zhu, M. Wang, M. Shen, L. Chen, and X. Ni, "An Optical Fiber Fabry-Pérot Pressure Sensor Using an SU-8 Structure and Angle Polished Fiber," *IEEE Photonics Technol. Lett.*, vol. 27, no. 19, pp. 2087–2090, 2015.

[107] J. Zhu, M. Wang, M. Shen, L. Chen, and X. Ni, "An Optical Fiber Fabry-Pérot Pressure Sensor Using an SU-8 Structure and Angle Polished Fiber," *IEEE Photonics Technol. Lett.*,

vol. 27, no. 19, pp. 2087–2090, Oct. 2015.

[108] J. Wu, M. Yao, F. Xiong, A. P. Zhang, H.-Y. Tam, and P. K. A. Wai, “Optical Fiber-Tip Fabry-Pérot Interferometric Pressure Sensor Based on an In Situ μ-Printed Air Cavity,” *J. Light. Technol.*, vol. 36, no. 17, 2018.

[109] Z. Shao *et al.*, “All-sapphire-based fiber-optic pressure sensor for high-temperature applications based on wet etching,” *Opt. Express*, vol. 29, no. 3, p. 4139, Feb. 2021.

[110] J. Yi, “Sapphire Fabry-Perot Pressure Sensor at High Temperature,” *IEEE Sens. J.*, vol. 21, no. 2, 2021.

[111] W. Li *et al.*, “Fiber-optic Fabry–Perot pressure sensor based on sapphire direct bonding for high-temperature applications,” *Appl. Opt.*, vol. 58, no. 7, p. 1662, Mar. 2019.

[112] Q. Yu and X. Zhou, “Pressure sensor based on the fiber-optic extrinsic fabry-perot interferometer,” *Photonic Sensors*, vol. 1, no. 1, pp. 72–83, 2011.

[113] J. Yin *et al.*, “Batch-Producible Fiber-Optic Fabry – Pérot Sensor,” *IEEE Photonics Technol. Lett.*, vol. 26, no. 20, pp. 2070–2073, 2014.

[114] G. Liu and M. Han, “Fiber-optic gas pressure sensing with a laser-heated silicon-based Fabry–Perot interferometer,” *Opt. Lett.*, vol. 40, no. 11, p. 2461, Jun. 2015.

[115] L. Pavesi and D. Lockwood, *Topics in Applied Physics Volume 94: Silicon Photonics*, 1st ed., vol. 94. Springer, 2004.

[116] A. Cowen, G. Hames, D. Monk, S. Wilcenski, and B. Hardy, *SOIMUMPs Design Handbook*, 8th ed. MEMSCAP Inc.

[117] D. Donlagic and E. Cibula, “All-fiber high-sensitivity pressure sensor with SiO_2

diaphragm," *Opt. Lett.*, vol. 30, no. 16, p. 2071, Aug. 2005.

[118] M. Rajibul Islam, M. Mahmood Ali, M. H. Lai, K. S. Lim, and H. Ahmad, "Chronology of fabry-perot interferometer fiber-optic sensors and their applications: A review," *Sensors (Switzerland)*, vol. 14, no. 4. Molecular Diversity Preservation International, pp. 7451–7488, 24-Apr-2014.

[119] C. Lin and X. Fang, "Proceedin g s of ASID2016 Miniature MEMS Fabry-Perot Interferometry Pressure Sensor and the Fabrication System."

[120] P. Xu, F. Pang, N. Chen, Z. Chen, and T. Wang, "Fabry-Perot temperature sensor for quasi-distributed measurement utilizing OTDR," *1st Asia-Pacific Opt. Fiber Sensors Conf. APOS*, 2008.

[121] M. Bass and E. W. Van Stryland, *Fiber Optic Handbook - fiber, device, and system*, 1st ed. McGraw-Hill Professional.

[122] C. E. Lee, R. A. Atkins, and H. F. Taylor, "Performance of a fiber-optic temperature sensor from-200 to 10500C," 1988.

[123] L.-X. Kong *et al.*, "High-sensitivity and fast-response fiber-optic micro-thermometer based on a plano-concave Fabry-Pérot cavity filled with PDMS," *Sensors Actuators A*, vol. 281, pp. 236–242, 2018.

[124] G. Cocorullo, F. G. Della Corte, I. Rendina, and P. M. Sarro, "Thermo-optic effect exploitation in silicon microstructures," *Sensors and Actuators A: Physical*, 1998. .

[125] Z. Liu, X. Qiao, and R. Wang, "Miniaturized fiber-taper-based Fabry-Perot interferometer for high-temperature sensing," *Appl. Opt.*, vol. 56, no. 2, pp. 256–259, 2017.

[126] P. A. R. Tafulo, P. A. S. Jorge, J. L. Santos, and O. Frazão, “Fabry-Pérot cavities based on chemical etching for high temperature and strain measurement,” *Opt. Commun.*, vol. 285, pp. 1159–1162, 2012.

[127] T. Zhu, T. Ke, Y. Rao, and K. S. Chiang, “Fabry-Perot optical fiber tip sensor for high temperature measurement,” *Opt. Commun.*, vol. 283, no. 19, pp. 3683–3685, Oct. 2010.

[128] Z. Chen *et al.*, “High-Temperature Sensor Based on Fabry-Perot Interferometer in Microfiber Tip,” *Sensors*, vol. 18, no. 1, p. 202, Jan. 2018.

[129] W.-H. Tsai and C.-J. Lin, “A Novel Structure for the Intrinsic Fabry-Perot Fiber-Optic Temperature Sensor,” 2001.

[130] H. Y. Choi, K. S. Park, S. J. Park, U.-C. Paek, B. H. Lee, and E. S. Choi, “Miniature fiber-optic high temperature sensor based on a hybrid structured Fabry-Perot interferometer,” *Opt. Lett.*, vol. 33, no. 21, pp. 2455–2457, 2008.

[131] R. Fan, Y. Hou, and W. Sun, “Photonic Crystal Fiber Fabry-Perot Interferometers With High-Reflectance Internal Mirrors,” *Photonic Sensors*, vol. 5, no. 2, pp. 97–101, 2015.

[132] Y. Lopez-Dieguez *et al.*, “Multi-mode all Fiber Interferometer based on Fabry-Perot Multi-cavity and its Temperature Response,” *Optik (Stuttg).*, vol. 147, pp. 232–239, 2017.

[133] T. Zhu, T. Ke, Y. Rao, and K. S. Chiang, “Fabry-Perot optical fiber tip sensor for high temperature measurement,” *optics*, vol. 283, no. 19, pp. 3683–3685, 2010.

[134] Y. Zhao, D. Wang, and R. Lv, “A novel optical fiber temperature sensor based on Fabry-Perot cavity,” *Microw. Opt. Technol. Lett.*, vol. 55, no. 10, pp. 2487–2490, Oct. 2013.

[135] J. Kou, J. Feng, L. Ye, F. Xu, and Y. Lu, “Miniaturized fiber taper reflective interferometer

for high temperature measurement," *Opt. Express*, vol. 18, no. 13, p. 14245, Jun. 2010.

[136] X. Li, S. Lin, J. Liang, H. Oigawa, and T. Ueda, "High-Sensitivity Fiber-Optic Fabry–Perot Interferometer Temperature Sensor," *Jpn. J. Appl. Phys.*, vol. 51, no. 6S, p. 06FL10, Jun. 2012.

[137] M. S. Ferreira, P. Roriz, S. O. Silva, J. L. Santos, and O. Frazão, "Next generation of Fabry-Perot sensors for high-temperature," *Opt. Fiber Technol.*, vol. 19, pp. 833–837, 2013.

[138] K. Yang *et al.*, "Ultrasensitive temperature sensor based on a fiber fabry-pérot interferometer created in a mercury-filled silica tube," *IEEE Photonics J.*, vol. 7, no. 6, Dec. 2015.

[139] S. Dwivedi *et al.*, "Experimental Extraction of Effective Refractive Index and Thermo-Optic Coefficients of Silicon-on-Insulator Waveguides Using Interferometers," *J. Light. Technol.*, vol. 33, no. 21, 2015.

[140] G. Liu, M. Han, and W. Hou, "High-resolution and fast-response fiber-optic temperature sensor using silicon Fabry-Pérot cavity," *Opt. Express*, vol. 23, no. 6, pp. 7237–7247, 2015.

[141] Y. Ge, Q. Liu, J. Chang, and J. Zhang, "Optical fiber sensor for temperature measurement based on Silicon thermo-optics effect," *Optik (Stuttg).*, vol. 124, no. 24, pp. 6946–6949, Dec. 2013.

[142] G. Liu, M. Han, W. Hou, S. Matt, and W. Goode, "A miniature fiber-optic sensor for high-resolution and high-speed temperature sensing in ocean environment," *Ocean Sens. Monit. VII, SPIE*, vol. 9459, pp. 80–85, May 2015.

[143] G. H. Yoon, E. M. Dede, T. Nomura, and P. Schmalenberg, "Topology optimization of

time-transient heat conduction for thermo-optic silicon modulators," *Int. J. Heat Mass Transf.*, vol. 157, p. 119862, Aug. 2020.

[144] G. Cocorullo, F. G. Della Corte, M. Iodice, I. Rendina, and P. M. Sarro, "A Temperature All-Silicon Micro-Sensor Based on the Thermo-Optic Effect," *IEEE Trans. Electron Devices*, vol. 44, no. 5, 1997.

[145] G. Cocorullo, F. G. Della Corte, and I. Rendina, "Temperature dependence of the thermo-optic coefficient in crystalline silicon between room temperature and 550 K at the wavelength of 1523 nm," *Appl. Phys. Lett.*, vol. 74, no. 22, pp. 3338–3340, 1999.

[146] D.-X. Xu *et al.*, "Empirical model for the temperature dependence of silicon refractive index from O to C band based on waveguide measurements," *Opt. Express*, vol. 27, no. 19, p. 27229, 2019.

[147] S. Renard, "Industrial MEMS on SOI," *J. Micromechanics Microengineering*, vol. 10, no. 2, p. 245, Jun. 2000.

[148] W. Noell *et al.*, "Applications of SOI-based optical MEMS," *IEEE J. Sel. Top. Quantum Electron.*, vol. 8, no. 1, pp. 148–154, Jan. 2002.

[149] "FIS - Your Fiber Optics Experts - Fiber Instrument Sales," *Fiberinstrumentsales.com, 2021*. [Online]. Available: https://www.fiberinstrumentsales.com/. [Accessed: 13-Oct-2021].

[150] "FIS SMA905 Stainless Steel Connector 127um - Fiber Instrument Sales." [Online]. Available: https://www.fiberinstrumentsales.com/fis-sma905-stainless-steel-connector-127um.html. [Accessed: 13-Oct-2021].

[151] T. Lű, “Influence of cavity loss on an extrinsic Fabry-Perot cavity intensity-based pressure sensor,” *Rev. Sci. Instrum.*, vol. 86, no. 9, p. 095002, Sep. 2015.

[152] TT Electronics, “Fiber Optic Receiver OPF520 Series,” 2019.

[153] G. AbdulRahman, K. Iyer, N. Patricia, and K. Amir, “2016 IEEE SENSORS Proceedings,” in *Fiber Optic Monitoring of Lithium-Ion Batteries*, 2016, pp. 868–70. Orlando, FL, USA: IEEE, 2016.

[154] “Lindberg/Blue M™ Moldatherm™ Box Furnaces.” [Online]. Available: https://www.thermofisher.com/order/catalog/product/BF51794C#/BF51794C. [Accessed: 13-Oct-2021].

[155] “USB-TC01 - NI.” [Online]. Available: https://www.ni.com/en-ca/support/model.usb-tc01.html. [Accessed: 14-Oct-2021].

[156] “FIS Coupler 1x2 SM Dual Window1310/1550nm 50/50 Split 900um - Fiber Instrument Sales.” [Online]. Available: https://www.fiberinstrumentsales.com/fis-dual-window-1310-1550nm-1x2-coupler-50-50-split-900um.html. [Accessed: 14-Oct-2021].

[157] M. Li, Y. Liu, R. Gao, Y. Li, X. Zhao, and S. Qu, “Ultracompact fiber sensor tip based on liquid polymer-filled Fabry-Perot cavity with high temperature sensitivity,” *Sensors Actuators B*, vol. 233, pp. 496–501, 2016.

[158] A. Saltelli, “Sensitivity Analysis for Importance Assessment,” *Risk Anal.*, vol. 22, no. 3, pp. 579–590, Jun. 2002.

[159] T. O. Kvalseth, “Cautionary Note about R 2,” *Am. Stat.*, vol. 39, no. 4, pp. 279–285, 1985.

[160] J. P. Bentley, “Temperature sensor characteristics and measurement system design,” *J.*

Phys. E., vol. 17, no. 6, p. 430, Jun. 1984.

[161] V. K. Rai, "Temperature sensors and optical sensors," *Appl. Phys. B 2007 882*, vol. 88, no. 2, pp. 297–303, Jul. 2007.

[162] G. C. M. Meijer, G. Wang, and A. Heidary, "Smart temperature sensors and temperature sensor systems," *Smart Sensors MEMS Intell. Sens. Devices Microsystems Ind. Appl. Second Ed.*, pp. 57–85, Jan. 2018.

[163] J. Gums, "Types of Temperature Sensors | DigiKey." [Online]. Available: https://www.digikey.com/en/blog/types-of-temperature-sensors. [Accessed: 06-Aug-2022].

[164] D. Baird, *Experimentation : an introduction to measurement theory and experiment design*, 3rd ed. Englewood Cliffs: Prentice-Hall, 1995.

[165] P. Bevington and K. Robinson, *Data Reduction and Error Analysis for the Physical Sciences*, 2nd ed. New York: McGraw-Hill, 1989.

[166] D. K. Lee, J. In, and S. Lee, "Standard deviation and standard error of the mean," *Korean J. Anesthesiol.*, vol. 68, no. 3, pp. 220–223, Jun. 2015.

[167] G. Cocorullo, F. G. Della Corte, I. Rendina, and P. M. Sarro, "Thermo-optic effect exploitation in silicon microstructures," *Sensors Actuators A Phys.*, vol. 71, no. 1–2, pp. 19–26, Nov. 1998.

[168] B. J. Frey, D. B. Leviton, and T. J. Madison, "Temperature-dependent refractive index of silicon and germanium," *Optomech. Technol. Astron. SPIE*, vol. 6273, 2006.

[169] Taylor J.R., *Introduction to error analysis 2ed | Enhanced Reader*. University Science

Books: Sausalito, 1996.

[170] D. M. Allen, “Mean square error of prediction as a criterion for selecting variables,” *Technometrics*, vol. 13, no. 3, pp. 469–475, 1971.

[171] S. K. Ibrahim, F. Martin, and J. A. O’Dowd, “Fiber Sensing for Space Applications,” in *European Conference on Spacecraft Structures Materials and Environmental Testing (ECSSMET 2018)*, 2018.

[172] D. Lee, M. Yang, C. Huang, and J. Dai, “Optical fiber high-temperature sensor based on dielectric films extrinsic fabry-Pérot cavity,” *IEEE Photonics Technol. Lett.*, vol. 26, no. 21, pp. 2107–2110, Nov. 2014.

[173] L. Li *et al.*, “Ultrahigh sensitive temperature sensor based on Fabry-Pérot interference assisted by a graphene diaphragm,” *IEEE Sens. J.*, vol. 15, no. 1, pp. 505–509, Jan. 2015.

[174] S. Meti, K. B. Balavald, and B. G. Sheeparmatti, “MEMS Piezoresistive Pressure Sensor: A Survey,” *Int. J. Eng. Res. Appl.*, vol. 6, no. 4(part 1), pp. 23–31, 2016.

[175] A. Nallathambi, T. Shanmuganantham, and D. Sindhanaiselvi, “Design and Analysis of MEMS based Piezoresistive Pressure sensor for Sensitivity Enhancement,” *Mater. Today Proc.*, vol. 5, no. 1, pp. 1897–1903, Jan. 2018.

[176] Besling, W. F. Adrianus, K. Reimann, P. Steeneken, O. Wunnicke, and R. Woltjer., “MEMS capacitive pressure sensor, operating method and manufacturing method,” U.S. Patent No. 9,383,282. 5 Jul. 2016.

[177] K. B. Balavalad and B. G. Sheeparamatti, “Sensors & Transducers A Critical Review of MEMS Capacitive Pressure Sensors,” *Sensors & Transducers*, vol. 187, pp. 120–128, 2015.

[178] D. Xu, Y. Wang, B. Xiong, and T. Li, “MEMS-based thermoelectric infrared sensors: A review,” *Front. Mech. Eng.*, vol. 12, no. 4, pp. 557–566, Dec. 2017.

[179] X. Song *et al.*, “An Integrated Gold-Film Temperature Sensor for In Situ Temperature Measurement of a High-Precision MEMS Accelerometer,” *Sensors*, vol. 20, no. 13, p. 3652, Jun. 2020.

[180] T. Kose, K. Azgin, and T. Akin, “Design and fabrication of a high performance resonant MEMS temperature sensor,” *J. Micromechanics Microengineering*, vol. 26, no. 4, Mar. 2016.

[181] H. Alemohammad *et al.*, “Fiber Optic Sensors for Harsh Environments: Environmental, Hydrogeological, and Chemical Sensing Applications,” in *Optical fiber sensors. Optical Society of America*, 2018, p. TuB4.

[182] R. Pirich and K. D’Ambrosio, “Fiber optics for harsh environments,” in *2011 IEEE Long Island Systems, Applications and Technology Conference.*, 2011.

[183] C. Pang, H. Bae, A. Gupta, K. Bryden, and M. Yu, “MEMS Fabry-Perot sensor interrogated by optical system-on-a-chip for simultaneous pressure and temperature sensing,” *Opt. Express*, vol. 21, no. 19, p. 21829, Sep. 2013.

[184] S. Pevec and D. Donlagic, “Multiparameter fiber-optic sensor for simultaneous measurement of thermal conductivity, pressure, refractive index, and temperature.,” *IEEE Photonics J.*, vol. 9, no. 1, pp. 1–14, 2017.

[185] N. Kurgan and R. Varol, “Mechanical properties of P/M 316L stainless steel materials,” *Powder Technol.*, vol. 201, no. 3, pp. 242–247, Aug. 2010.

[186] T. (Tom) Bell, K. Akamatsu, and N. N. G. Kyōkai., *Stainless steel 2000: thermochemical surface engineering of stainless steel.* London: CRC Press, 2001.

[187] E. Thecnology, “EPO-TEK ® 353ND Technical Data Sheet For Reference,” 2017.

[188] Thorlabs, “SFLC127-10 Ø1.25 mm, 6.4 mm Long SS Ferrule for MM Fiber, Ø127 µm Bore Size, 10 Pack.” [Online]. Available: https://www.thorlabs.com/thorproduct.cfm?partnumber=SFLC127-10. [Accessed: 17-Apr-2022].

[189] “MorHEAT Inc. - Home.” [Online]. Available: https://mpimorheat.com/. [Accessed: 03-Mar-2020].

[190] J. G. Korvink, E. B. Rudnyi, A. Greiner, and Z. Liu, *MEMS: A Practical Guide of Design, Analysis, and Applications*. Norwich, NY, U.S.A .: William Andrew, Inc, 2010.

[191] Comsol, “The Structural Mechanics Module User’s Guide,” 2018. [Online]. Available: available: https://www.comsol.com/structural-mechanics-module. [Accessed: 10-Dec-2019].

[192] S. Timoshenko and S. Woinowsky-Krieger, *Theory of plates and shells*, 2nd ed. New York: McGraw-Hill, Inc, 1959.

[193] W. C. Young and R. G. Budynas, *Roark’s Formulas for Stress and Strain*. McGraw-Hill Education, 2012.

[194] S. Ghildiyal, R. Balasubramaniam, and J. John, “Diamond turned micro machined metal diaphragm based Fabry Perot pressure sensor,” *Opt. Laser Technol.*, vol. 128, p. 106243, Aug. 2020.

[195] L. Zhang *et al.*, “A diaphragm-free fiber Fabry-Perot gas pressure sensor,” *Rev. Sci. Instrum.*, vol. 90, no. 2, p. 025005, Feb. 2019.

[196] S. Ghildiyal, P. Ranjan, S. Mishra, R. Balasubramaniam, and J. John, “Fabry-Perot Interferometer-Based Absolute Pressure Sensor With Stainless Steel Diaphragm,” *IEEE Sens. J.*, vol. 19, no. 15, 2019.

[197] C. Zhou, S. V. Letcher, and A. Shukla, “Fiber-optic microphone based on a combination of Fabry–Perot interferometry and intensity modulation,” *J. Acoust. Soc. Am.*, vol. 98, no. 2, p. 1042, Jun. 1998.

[198] T. J. Bannon, “The Ambiguity of the Inverse Secant,” *Math. Teach.*, vol. 111, no. 6, pp. 470–475, Apr. 2018.

[199] H. H. D. Alan Jeffrey, *Handbook of Mathematical Formulas and Integrals FOURTH EDITION*. Elsevier.

[200] “RapidTables (Arccos(x) function).” [Online]. Available: https://www.rapidtables.com/math/trigonometry/arccos.html. [Accessed: 19-Feb-2022].

[201] J. E. Suarez, B. E. Johnson, and B. El-Kareh, “Thermal Stability of Polysilicon Resistors,” *IEEE Trans. Components, Hybrids, Manuf. Technol.*, vol. 15, no. 3, pp. 386–392, 1992.

[202] H. Karbasi and H. Reiser, “Smart Mold: Real-Time in-Cavity Data Acquisition,” in *in First Annual Technical Showcase & Third Annual Workshop, Canada, 2006*, 2006.

[203] M. B. Uday, M. N. Ahmad-Fauzi, A. M. Noor, and S. Rajoo, “Current Issues and Problems in the Joining of Ceramic to Metal,” in *Joining Technologies*, IntechOpen, 2016.

Appendix

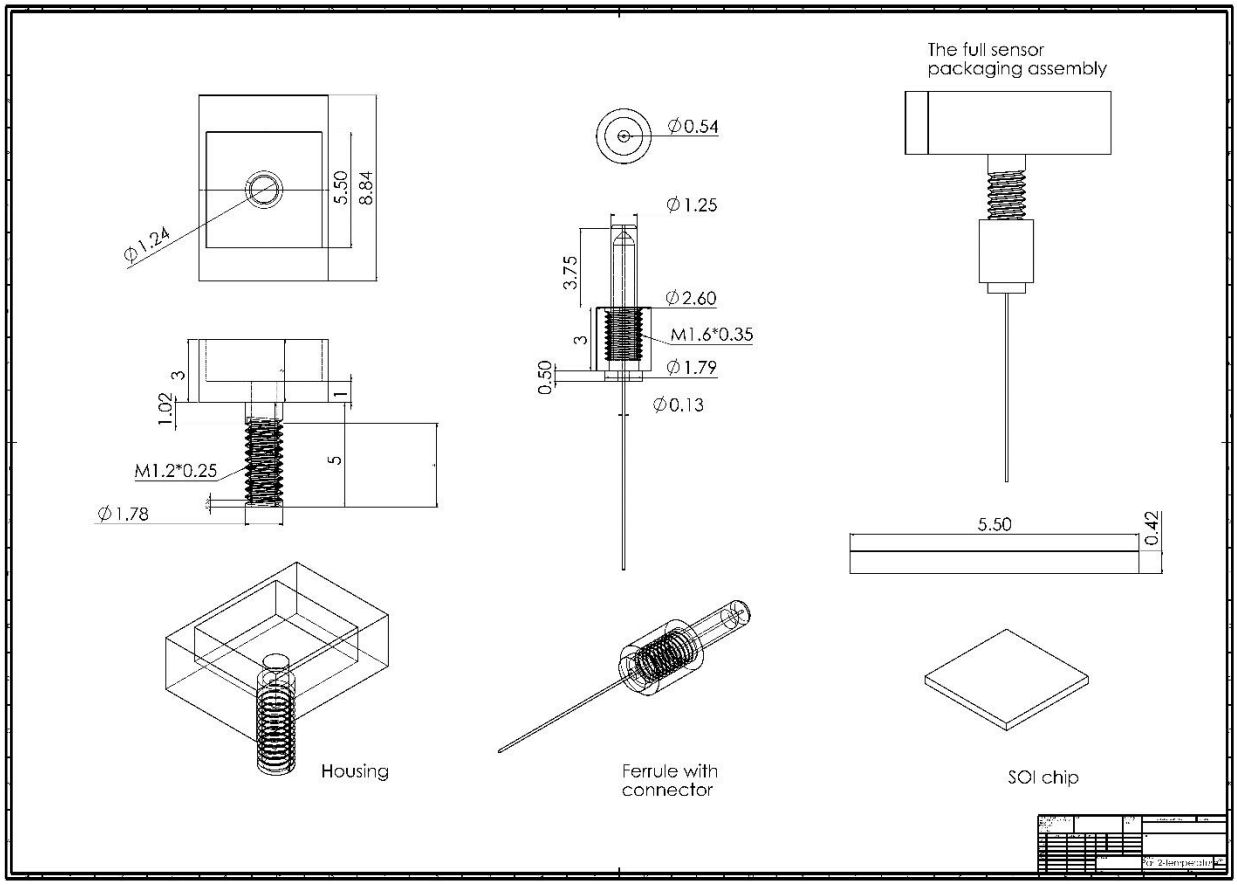

Fig. 43. A detailed plot of the developed packaging for temperature sensor with dimensions in mm (discussed in chapter 4).

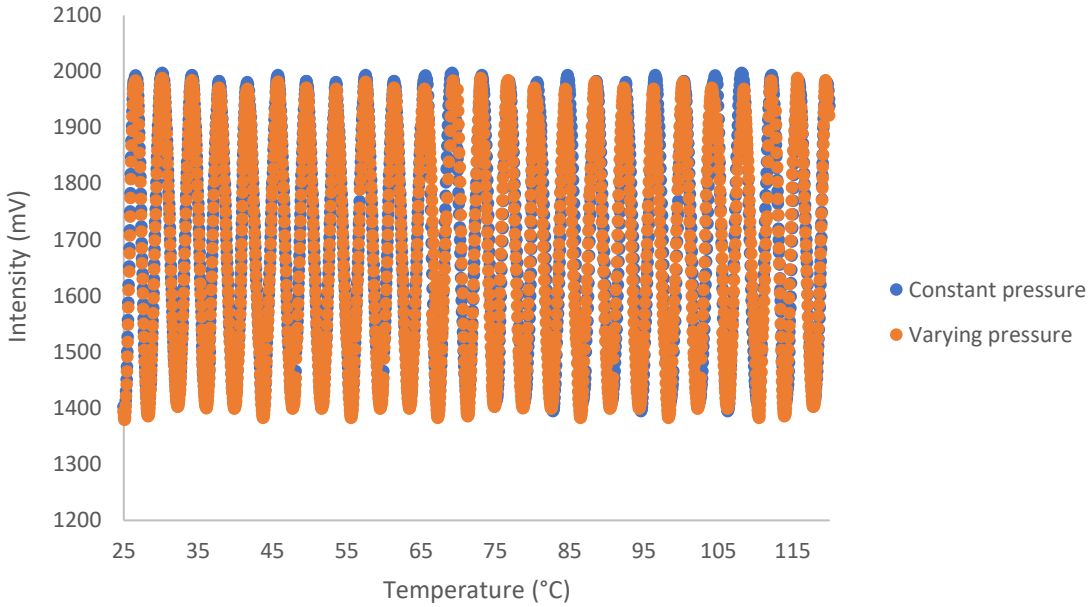

Fig. 44. The experimental intensity responses to temperature variations from 25℃–120℃ for Optical Fiber 1 (the fiber at the corner).